Aus der Klinik für **Angeborene Herzfehler Kinderkardiologie**

der Medizinischen Fakultät Charité – Universitätsmedizin Berlin

DISSERTATION

**Functional heart valve stent designs for future transcatheter autologous pulmonary valve replacement**

**Funktionelle Herzklappen-Stent Designs für zukünftige autologe, transkatheter Klappenprothesen in pulmonaler Position**

zur Erlangung des akademischen Grades
Doctor medicinae (Dr. med.)

vorgelegt der Medizinischen Fakultät
Charité – Universitätsmedizin Berlin

von

Xiaolin Sun

aus Qingdao, Shandong, Volksrepublik China

# Table of Contents

**A list of figures and tables**

## Abbreviations

| | |
|---|---|
| Autologous pulmonary valve | APV |
| Aortic stenosis | AS |
| Computed tomography | CT |
| Congenital Catheterization Collaborative Project on Outcomes–Quality Improvement | C3PO-QI |
| Congenital Heart Disease | CHD |
| Deutsches GrOwnValve Stent | DGS |
| Deutsches Herzzentrum Berlin | DHZB |
| Disability-adjusted life years | DALYs |
| Ejection fraction | EF |
| Finite element analysis | FEA |
| Forschungseinrichtungen für Experimentelle Medizin | FEM |
| Hoop force | HF |
| Infective endocarditis | IE |
| Inferior vena cava | IVC |
| Left bundle branch block | LBBB |
| Left ventricular outflow tract | LVOT |
| Newton | N |
| Paravalvular leak | PVL |
| Percutaneous pulmonary valve implantation | PPVI |
| Permanent pacemaker implantation | PPI |
| Pulmonary artery | PA |
| Radial force | RF |
| Rheumatic heart disease | RHD |
| Right bundle branch block | RBBB |
| Right ventricular end-diastolic volume | RVEDVI |
| Right ventricular outflow tract | RVOT |
| Right ventricular systolic pressure | RVSP |
| Serious adverse events | SAE |
| Standard ACIS Text file format | SAT |
| Standard for the Exchange of Product Model Data file format | STP |
| Stereolithography | STL |
| Structural valve deterioration | SVD |
| Superior vena cava | SVC |
| Surgical aortic valve replacement | SAVR |
| Surgical pulmonary valve replacement | SPVR |
| Tetralogy of Fallot | TOF |
| Transcatheter aortic valve implantation | TAVI |
| Transcatheter aortic valve replacement | TAVR |
| Transcatheter autologous pulmonary valve replacement | TaPVR |
| Transcatheter pulmonary valve replacement | TPVR |
| Tricuspid valve | TV |
| Valve-in-valve | VIV |
| Valvular heart disease | VHD |

**Abstract (English)**

**Background** Transcatheter pulmonary valve replacement (TPVR) has asserted its position as a cornerstone in cardiology and become a nonsurgical alternative for patients with a dysfunctional right ventricular outflow tract (RVOT), demonstrating excellent early and late clinical outcomes. Short- and long-term complications of TPVR include stent fracture and migration, coronary compression, and valve regurgitation.

**Objective** The purpose of this study is to describe methodology for developing Nitinol stents by conducting a computational design and finite element analysis in conjunction with 3D reconstruction of animal cardiac CT for TPVR.

**Methods** 3D cardiac CT reconstruction was achieved using 3D Slicer, from which the RVOT + pulmonary artery (PA) was exported for blood flow simulation and hoop force acquisition with the stents. Functional stents were designed using Autodesk Fusion 360 and divided into three morphological geometries: group 1–straight tubular stents, group 2–corollaceous stents, and group 3–corollaceous stents with an elliptic geometry. Stent simulations for stent life and radial force, and the hoop force of the stent during expansion with the RVOT+PA model were obtained in Ansys. The blood flow simulation of RVOT+PA was performed using Ansys with the velocity-based coupled solver.

**Results** 3D cardiac CT reconstructions were obtained in STL format, from which the right ventricle (RV) +PA model was performed for the blood flow simulation and the hoop force was obtained with the stents. Twelve functional stents were successfully designed and exported in SAT and STP formats for simulation. All stent life (Times)/radial force (N) were achieved: Group 1 comprised the stents DGS-3 (3219.2/1.88E+05), DGS-5 (16406/1.94E+05), DGS-7 (1.00E+06/1.89E+05), DGS-8B (0/3.74E+05), DGS-10B (8370.1/2.41E+05), DGS-12D (1.00E+06/2.41E+08); Group 2 comprised the stents DGS-8A (0/3.60E+05), DGS-9A (0/3.60E+05), DGS-10A (46093/2.28E+05), DGS-12C (2.50E+005/1.69E+05); Group 3 comprised the stents DGS-12A (1.00E+06/2.38E+08), DGS-12B (54509/2.20E+05). Hoop force (N) was obtained from the 12 stents: Group 1– DGS-5 (57802), DGS-7 (54647), DGS-8B (53248), DGS-10B (56650), DGS-12D (46297). Group 2–DGS-8A (50490), DGS-9A (60393), DGS-10A (23639), DGS-12C (29802). Group 3–DGS-12A (16368), DGS-12B (16368). The RV+PA blood flow simulation demonstrated that the anterior part of the PA wall had the largest shear force.

**Conclusions** DGS-12C, DGS-12D, DGS-10A, DGS-10B, DGS-7, and DGS-5 can be subsequently tested in vitro. Autologous pulmonary valves could be sutured onto the functional stents to maintain their original geometry prior to implantation. Pre-implantation

3D CT reconstruction and stent simulation can be performed for better evaluation and visualization. The RV+PA blood flow simulation may serve as a significant input for the design of stents and pulmonary valve to determine the shear force throughout the cardiac cycle.

**Abstrakt (Deutsch)**

**Hintergrund** Der katheterbasierte Pulmonalklappenersatz ist ein Eckpfeiler der Kardiologie und bietet zudem eine nicht-chirurgische Alternative für die Behandlung funktionsgestörter rechtsventrikulärer Ausflusstrakte oder bioprothetischer Klappen mit hervorragenden frühen und späten klinischen Ergebnissen. Kurz- und langfristige Komplikationen von TPVR umfassen Stentfraktur/-migration, Komprimierung der Koronararterien und Klappeninsuffizienz.

**Ziel** Ziel dieser Studie ist es, die Methodik und das Konzept für Nitinol-Stents mithilfe rechnerischer Entwürfe und Finite-Elemente-Analysen anhand von 3D-Rekonstruktionen kardialer CT-Untersuchungen in Tieren für die Anwendung von TPVR zu beschreiben.

**Methoden** Die 3D-Rekonstruktion der CT-Untersuchungen erfolgte mit der Software 3D Slicer, aus der die RVOT und Pulmonalarterie (PA) in Verbindung mit den Stents für die Blutflusssimulation und die Umfangsspannung exportiert wurde. Die funktionellen Stents wurden mit Fusion 360 entworfen und danach in die Formate SAT und STP exportiert. Simulationen für die Lebensdauer und Radialkraft sowie für die Umfangsspannung der Stents bei der Freisetzung mit dem RVOT+PA-Modell wurden in Ansys berechnet. Die Blutflusssimulation von RVOT+PA wurde in Ansys mit dem geschwindigkeitsbasierten gekoppelten Solver durchgeführt.

**Ergebnisse** Zwölf funktionelle Stents wurden mithilfe von Fusion 360 generiert. SAT- und STP-Dateien wurden zur Simulation in Ansys exportiert. 3D Kardio-CT-Rekonstruktionen wurden mithilfe im STL-Format kreiert, aus dem das RVOT+PA-Modell des Prä-CT ausgewählt wurde, um die Blutflusssimulation durchzuführen und die Ringkraft der Stents zu erhalten. Die Lebensdauer (Anzahl) und Radialkraft (N) der Stents wurden wie folgt berechnet: DGS-3 (3219.2/1.88E+05), DGS-5 (16406/1.94E+05), DGS-7 (1.00E+06/1.89E+05), DGS-8A (0/3.60E+05), DGS-8B (0/3.74E+05), DGS-9A (0/3.60E+05), DGS-10A (46093/2.28E+05), DGS-10B (8370.1/2.41E+05), DGS-12A (1.00E+06/2.38E+08), DGS-12B (54509/2.20E+05), DGS-12D (1.00E+06/2.41E+08), DGS-12C (2.50E+005/1.69E+05). Die jeweilige Umspannungskraft (N) wurde wie folgt berechnet: DGS-5 (57802), DGS-7 (54647), DGS-8A (50490), DGS-8B (53248), DGS-9A (60393), DGS-10A (23639), DGS-10B (56650), DGS-12A (16368), DGS-12B (16368), DGS-12C (29802), DGS-12D (46297). Die RV+PA-Blutflusssimulation zeigte, dass der vordere Teil der PA-Wand die größte Scherkraft aufwies.

**Schlussfolgerungen** DGS-12C, DGS-12D, DGS-10A, DGS-10B, DGS-7 und DGS-5 können nachfolgend in vitro getestet werden. Autologe Pulmonalklappen können zur

Erhaltung der ursprünglichen Geometrie vor der Implantation auf funktionelle Stents aufgenäht werden. Vor der Implantation können Kardio-CT 3D-Rekonstruktion und Stentsimulationen zur besseren Bewertung und Visualisierung durchgeführt werden. Die Blutflusssimulation von RVOT+PA kann einen bedeutsamen Beitrag zur Gestaltung von Stents und Pulmonalklappen leisten, um die Scherkraft während des gesamten Herzzyklus zu erhalten.

# 1. Introduction

## 1.1. Epidemiology of valvular diseases

Valvular heart disease (VHD) is a leading cause of physical disability, poor quality of life, and shortened life expectancy throughout the world (1-4) (**Figure 1**). The epidemiology of VHD differs significantly across nations, with functional and degenerative disease being predominant in high-income countries, while rheumatic heart disease (RHD) is prevalent in low- and middle-income countries (5).
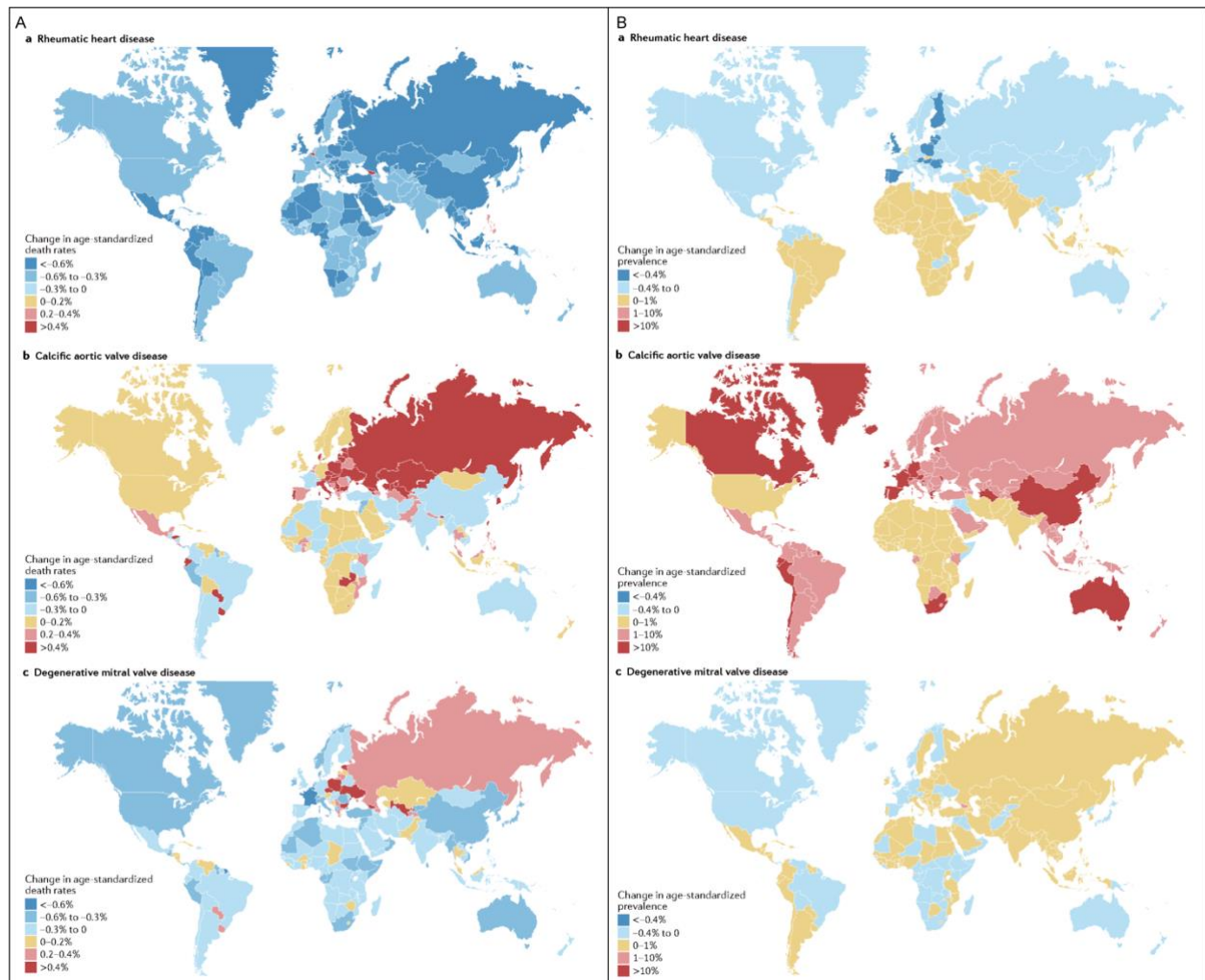


**Figure 1. Epidemiology of valvular disease** (1)
**A.** Changes in age-standardized death rates due to three forms of valvular heart disease. The maps show changes in age-standardized death rates between 1990 and 2019 due to rheumatic heart disease (**Part a**), calcific aortic valve disease (**Part b**), and degenerative mitral valve disease (**Part c**). Deaths due to rheumatic heart disease and degenerative mitral valve disease reduced overall, whereas those due to calcific aortic valve disease remained stable.
**B.** Changes in age-standardized prevalence of three forms of valvular heart disease from 1990 to 2019. The maps show changes in the age-standardized prevalence of rheumatic heart disease (**Part a**), calcific aortic valve disease (**Part b**), and degenerative mitral valve disease (**Part c**). The prevalence of rheumatic heart disease increased in endemic areas and continued to fall in non-endemic areas. By contrast, the prevalence of calcific aortic valve disease increased across the world, whereas the prevalence of degenerative mitral valve disease remained largely stable.

This distribution is evident as RHD continues to be the most prevalent symptom of VHD

globally, affecting 40.5 million individuals in 2019 with an annual incidence of 2.8 million. Moreover, it caused 306,000 fatalities worldwide in 2019, with a median age of 28.7 years in low- and middle-income countries (5). Despite a decrease in global mortality due to RHD since 1900, the mortality rate has remained relatively stable since 2000. RHD continues to be the primary cause of mortality in the context of VHD, and its incidence is on the rise at an alarming rate. Poverty, inequality, and stress are all linked to the diagnosis of RHD. Even though global rates of severe poverty have declined in the last 40-50 years, such advances have not been associated with a decrease in the incidence of RHD on a global scale (1). Furthermore, significant disparities still exist between high-income and middle- or low-income nations.

There is a strong association of advanced age with calcific aortic valve disease, which has a rapidly increasing incidence in high-income nations. Global estimates indicate a prevalence of calcific aortic valve disease of 9.4 million people in 2019 (5). According to data obtained from a large Australian registry, moderate and severe aortic stenosis are closely linked to significant morbidity and mortality, with a 5-year mortality of 56% and 67%, respectively (6). Calcific aortic valve disease resulted in an estimated 126,827 deaths in 2019, representing a 138% increase since 1990 with no change in age-standardized prevalence, and a loss of 1.8 million disability-adjusted life years (DALYs) annually (5).

Around 24.2 million individuals worldwide are afflicted with mitral regurgitation (with a greater incidence in older age groups), which contributed to the loss of 0.88 million DALYs and the lives of 34,171 people in 2019 (5). Secondary (or functional) mitral regurgitation results from morphological changes in the left atrium or left ventricle (with normal valve leaflets) (7), and affects up to 24% of patients with systolic heart failure (8). Furthermore, of these, 65% have moderate or severe mitral regurgitation (9, 10). In non-rheumatic VHD, aortic regurgitation is the third most common type (following aortic stenosis and degenerative mitral regurgitation) (11, 12) and can be either caused by primary valve pathology (bicuspid aortic valve, RHD, infective endocarditis, connective tissue disease, or autoimmune disorders) or be secondary to aortic root dilatation. Aortic valve regurgitation is present in 30% of individuals with a bicuspid aortic valve (13) with moderate to severe symptoms. Aortic regurgitation is typically moderate in individuals with RHD and is very rarely seen as a single lesion (14). Moreover, advanced age is correlated with an increase in size of the aortic root, which has a significant hereditary

component (15) and is linked with hypertension that differs in systolic (but not diastolic) blood pressure (16).

Congenital heart disease is relatively rare, affecting about 1 in 200 and 1 in 125 live infants in China and the United States, respectively (17-19). Valvular anomalies are a common component of congenital heart disease, either alone or in combination with other congenital symptoms. A bicuspid aortic valve is present in approximately 0.4-0.6% of the population (more in men than women) (20, 21), with 6.4% of first-degree relatives of affected individuals having the condition as well (22). In addition, high rates of pulmonary stenosis (about 0.5 per 1,000 live births) and tetralogy of Fallot (0.3 per 1,000 live births) exist, both of which are life-threatening conditions and more common in Asia than in other regions of the world (23, 24). The absolute death rate due to congenital heart disease decreased by 60% between 1990 and 2019, accompanied by a 28% increase in its global prevalence (5). This may be due to improved survival, population growth and better early detection via antenatal ultrasound and pediatric echocardiography (25). Similarly, the incidence of congenital pulmonary stenosis or tetralogy of Fallot at birth has risen significantly worldwide in the last five decades (23). The prevalence of congenital heart disease varies by region; for example, in China, the increasing prevalence of congenital heart disease is mostly due to patent ductus arteriosus and atrioventricular septal defects (rather than congenital valvular heart disease). Meanwhile, the prevalence of congenital pulmonary stenosis and tetralogy of Fallot has remained stable or decreased (19).

**1.2. Transcatheter heart valve implantation**

**1.2.1   Transcatheter aortic valve implantation (TAVI)**

TAVI has transformed the treatment of aortic stenosis (AS) since it was first performed in 2002 (26). It is now the gold standard of care for patients with AS who are not suitable for open-heart surgery and is approved by the U.S. Food and Drug Administration for patients of all surgical risk profiles (**Figure 2**) (27-29). In a study, 797 high-risk surgical patients were randomized (1:1) to TAVI with a self-expanding bioprosthesis (CoreValve System, Medtronic, Dublin, Ireland) or to surgical aortic valve replacement (SAVR). The study showed that TAVI with self-expanding bioprostheses is associated with survival, safety and functional outcomes at 5 years, similar to those with SAVR (30). Meanwhile, 2032 intermediate-risk patients with severe symptomatic aortic stenosis were enrolled in the PARTNER 2 trials, which found no significant differences in the incidence of death from any cause or disabling stroke between the TAVI group (SAPIEN XT heart valve system, Edwards Lifesciences) and the surgical group (47.9% and 43.4%, respectively)

at 5 years (31). Favorable outcomes following TAVI with third-generation balloon-expandable (SAPIEN 3, Edwards Lifesciences) and self-expanding devices (CoreValve, Evolut R, or Evolut PRO, Medtronic, Dublin, Ireland) versus SAVR in low-risk subjects showed that the rate of the composite endpoint of death, stroke, or rehospitalization at 1 year was significantly lower with TAVI than with surgery (28). Also, TAVI was not found to be inferior to surgery with respect to the composite endpoint of death or disabling stroke at 24 months (29). In a nationwide head-to-head study of matched high-risk patients with degenerated bioprosthetic aortic valves, valve-in-valve (VIV) TAVI was shown to be more favorable to re-SAVR in terms of 30-day mortality, morbidity, and bleeding complications (32). In a 3-year PARTNER follow-up, TAVI for bioprosthetic aortic valve failure was associated with favorable survival, improved hemodynamic status, as well as excellent functional and quality-of-life outcomes (33).



| | Acurate (Boston Scientific) | Allegra (NVT) | Centera (Edwards) | Evolut PRO (Medtronic) | Evolut R (Medtronic) | JenaValve (JenaValve) | Portico (ST. Jude) | Sapien 3 (Edwards) | VenousA (Venus Medtech) |
|---|---|---|---|---|---|---|---|---|---|
| **Design Properties** | | | | | | | | | |
| Leaflets | Porcine Pericardium | Bovine Pericardium | Bovine Pericardium | Porcine Pericardium | Porcine Pericardium | Porcine Pericardium | Bovine Pericardium | Bovine Pericardium | Porcine Pericardium |
| Stent Frame | Nitinol | Nitinol | Nitinol | Nitinol | Nitinol | Nitinol | Nitinol | Cobalt-Chromium | Nitinol |
| Delivery | Self-expandable | Self-expandable | Self-expandable | Self-expandable | Self-expandable | Self-expandable | Self-expandable | Balloon-expandable | Self-expandable |
| **Delivery** | | | | | | | | | |
| Routes | TF, TA,TS | TF | TF,TS | TF,TAo,TS | TF,TAo,TS | TF, TA | TF, TA | TF, TA, TAo | TF, TA,TS |
| Sheath Size | 18Fr/19Fr | 18Fr | 14Fr | 16Fr | 14Fr | 18Fr | 18Fr/19Fr | 14Fr/16Fr | 18Fr/20Fr |
| **CE Mark** (Years) | 2011 | 2017 | Awaited | 2017 | 2013 | 2011 (AS) 2013 (AR) | 2012 | 2014 | NA |
| **Specific Advantages** | Low PPM requirement. | Resheathable up to 70% of deployment. | Resheathable up to 85% of deployment. PTFE skirt to reduce PVL. Motorized DS. | Resheathable up to 80% of deployment. Double-layer porcine skirt. | Resheathable up to 80% of deployment. Upcoming RCT data in low risk population. | Active fixation for use in AR. | Resheathable up to 85% of deployment. | External skirt to reduce PVL. Upcoming RCT data in low-risk population. | Experience in bicuspid valve population in China. Reduced cost. |

**Figure 2. Comparative overview of selected TAVI devices**
AR: aortic regurgitation; AS: aortic stenosis; DS: delivery system; Fr: French scale; NA: not available; PPM: permanent pacemaker; PTFE: polytetrafluoroethylene; PVL: paravalvular leak; RCT: randomized controlled trial; Tao: transaortic; TA: transapical; TF: transfemoral; TS: trans-subclavian.

## 1.2.2   Transcatheter pulmonary valve replacement (TPVR)

Since 2000, when the first TPVR was performed by Bonhoeffer in Paris (34), minimally invasive pulmonary valve therapies have been established as an alternative strategy for patients with CHD, seeking a balance between deteriorating RVOT dysfunction and minimizing the overall number of surgeries throughout a patient's life (**Figure 3**).

Currently, two balloon-expandable devices are available for TPVR: the Melody™ valve (Medtronic plc, Ireland; CE mark in 2006) and SAPIEN XT (Edwards Lifesciences LLC,

USA; FDA approval in 2017). The devices have different specifications related to the intended TPVI diameters (Melody™ valve: 18, 20, and 22 mm; SAPIEN XT: 20, 23, 26, and 29 mm). In a large-scale cohort of CHD patients with RVOT dysfunction from 42 heart centers, the post-approval MELODY Registry confirmed the efficacy of TPVI with the Melody™ valve, with an incidence rate of 4.2% per person per year (95% CI 3.7–4.9) for the composite endpoint of TPVI-related death, reoperation, and reintervention, as well as an incidence rate of 2.3% per person per year (95% CI 1.9–2.8) for infective endocarditis, resulting in significant morbidity and mortality (35). Furthermore, the Melody™ valve was also found to be feasible and safe when applied in expandable small-diameter RVOT conduits with favorable early and long-term procedural and hemodynamic outcomes (36). Moreover, TPVR with the Melody valve showed similar long-term outcomes in terms of survival and freedom of reinterventions compared with surgical pulmonary valve replacement (SPVR) (37). Another recently reported multicenter study containing the largest series of patients who underwent TPVR with a SAPIEN XT or S3 valve showed generally excellent procedural outcomes, which are particularly encouraging in relation to large valves implanted in patients with a large native/patched RVOT (38). However, the Melody™ valve and the SAPIEN XT or S3 valve had a higher incidence of serious adverse events (SAE) during TPVR in the C3PO-QI (Congenital Catheterization Collaborative Project on Outcomes–Quality Improvement) registry with uncommon mortality, greater radiation dose compared to other congenital interventions (associated with patient and procedural factors), and common reintervention during the early follow-up (39). The Venus P-valve, which has a self-expanding platform design, is feasible and safe in patients with severe pulmonary regurgitation (PR) who have previously undergone correction of tetralogy of Fallot with a transannular patch (40), which has been found to serve as an efficacious and minimally invasive alternative to SPVR in selected patients with a large RVOT, yielding better right ventricular and pulmonary valve function at the midterm follow-up (41, 42).

| | Melody™ (Medtronic) | Sapien XT (Edwards) | Sapien 3 (Edwards) | Harmony (Medtronic) | Pulsta valve (TaeWoong Medical Co. Ltd) | Venus P (Venus Medtech) | Alrerra valve (Edwards) |
|---|---|---|---|---|---|---|---|
| | | | | | | | |
| CE Mark | 2006 | 2010 | 2014 | - | - | 2022 | - |
| FDA Approval | 2017 | 2016 | 2020 | - | - | - | - |
| Stent | Cheatham platinum–iridium Balloon-Expandable | Cobalt chromium alloy Balloon-Expandable | Cobalt chromium alloy Balloon-Expandable | Self-expanding nitinol | Self-expanding nitinol | Self-expanding nitinol | Self-expanding nitinol |
| Valve | Bovine Jugular Vein | Bovine Pericardium | Bovine Pericardium | Porcine pericardium | Porcine pericardium | Porcine pericardium | Porcine pericardium |
| Valve Size | 18-22mm | 23-29mm | 20-29mm | 22mm, 25mm | 18-28mm | 20-36mm | 27mm |

**Figure 3. Comparative overview of selected TPVR devices**

### 1.3. Indications for TAVI and TPVR

### 1.3.1 Indications for TAVI

TAVI has been shown to be effective in older patients with symptomatic severe aortic stenosis, though its indication has recently been expanded in order to lower the risk and enable its use in younger patients (42, 43). The ESC/EACTS 2021 and AHA/ACC 2020 guidelines for the management of valvular heart disease (44, 45), which outline straightforward indications for TAVI or SAVR and provide considerable discretionary advice to clinicians, have helped strengthen TAVI's central position in the contemporary management of AS.

The decision between performing TAVI and SAVR should be based on the individual patient's risk-benefit ratio as well as their suitability for either treatment. An aortic anatomy that permits transfemoral delivery as well as the presence of severe comorbidities are additional criteria that favor the use of TAVI. Other variables that favor the use of TAVI include age $\geqslant$ 75 years, prior cardiac surgery, frailty, limited mobility, and diseases that are likely to impair rehabilitation (44, 45).

Evidence-based therapy recommendations for individuals suffering from severe valvular disease are based on a strong foundation of research. Although interventions in asymptomatic patients remain a matter of debate, any decision should be made after conducting a thorough consideration of the possible benefits versus the risks of the intervention and its long-term effects. To avoid permanent left ventricular myocardial alterations that may later lead to clinical symptoms and unfavorable cardiac events, it is important to carry out such interventions as early as possible. Emerging risk factors in individuals with asymptomatic AS include extremely severe valve blockage, high serum natriuretic peptide levels, and imaging indications favoring myocardial fibrosis or increased extracellular myocardial volume. Patients with a minimal surgical risk (STS < 4%) and no characteristics that favor TAVI should undergo SAVR, which implies that it is not currently indicated for the treatment of asymptomatic severe AS, though this may change in the future (45). If a patient has AR, the potential benefit of early intervention in preventing left ventricular dilatation and dysfunction must be weighed against the long-term risk of having a prosthetic valve. This is particularly important as severe AR frequently occurs in younger patients with a congenital bicuspid valve.

### 1.3.2 Indications for TPVR

TPVR was originally intended as an additional treatment in patients with a dysfunctional

RVOT, rather than as a substitute for surgery in those with a dysfunctional RVOT. Its goal was to increase the lifespan of surgically implanted conduits and decrease the number of surgical procedures required by CHD patients with RVOT dysfunction throughout the course of their lives.

Determining the optimal time for an intervention on the RVOT continues to be a challenge. Currently, the criteria for TPVI are the same as those for SPVR. When asymptomatic individuals with moderate to severe PR meet one of the following criteria, pulmonary valve replacement is recommended:

♥ Significant RV dilatation (RVEDVI > 150 mL/m², or RVESVI > 80 mL/m²)

♥ RV dysfunction (RV EF < 45%)

♥ Sustained atrial or ventricular arrhythmia

♥ RVOT obstruction with RVSP > 2/3 systemic or peak RVSP > 80 mmHg

♥ Progressive tricuspid regurgitation (at least moderate) (46, 47)

In symptomatic patients, intervention is indicated when there is moderate or severe PR, or significant stenosis with peak RVSP > 60 mmHg (46, 47).

Based on the ESC guidelines for the management of adult congenital heart disease (47), TPVR or PPVI has been used as an alternative to surgical intervention in certain situations. Due to its demonstrated safety and effectiveness profile, this developing technology has emerged as a viable option for surgery in a majority of patients suffering from RVOT dysfunction. There was no particular focus placed on surgery or TPVR as a first-line treatment. Accordingly, these two options were chosen in view of each individual patient's criteria.

As further research has been conducted, particularly with the publication of findings from a larger group of retrospective controlled studies in Europe, TPVR has been shown to have no statistically significant difference in long-term survival or valve durability when compared with surgical procedures, indicating that the two procedures are equivalent. Additionally, as TPVR is less invasive than surgery, patients have reported less discomfort. In 2018, AHA/ACC issued a guideline in view of evidence-based research (46), proposing TPVR rather than surgery as first-line treatment for patients with suitable anatomical conditions. This decision marked a major change in the clinical landscape. Due to ethical considerations, it is important to emphasize that these two cohorts (TPVR vs. surgery) cannot be allocated in a randomized controlled study due to the inherent difficulties. Therefore, according to ESC advice, TPVR is recommended as a category I

indication despite limited high-level evidence (47). A thorough analysis was conducted along with implementing the corresponding recommendations, which resulted in considering interventional therapy rather than surgery in this group of patients. Furthermore, invoking a discussion between the patient and surgeon about whether to combine intervention and surgery to improve the patient's condition has gained traction, which is a significant advantage.

## 1.4. Current issues associated with TAVI and TPVR

### 1.4.1 Current issues associated with TAVI

Although TAVI has become the gold standard of care for patients with low-high surgical risks, various medical device-related issues remain. These include:

♥ Valve durability and function (48-51)

Structural valve deterioration (SVD) is characterized as persistent intrinsic alterations in the valve (calcification, pannus, and leaflet failure) that result in degeneration and/or malfunction, which in turn may lead to valvular stenosis or intra-prosthetic regurgitation. The risk of SVD is significantly affected by the design of the valve as well as the age of the patient at the time of implantation.

♥ Stroke

Stroke is a severe consequence of TAVI and is associated with a 5- to 10-fold higher risk of short-term death in a hospital setting (27). Moreover, patients undergoing TAVI are at an elevated risk of having an embolic stroke both during the operation (related mainly to valve placement and deployment) and during the post-procedural period, which may extend from several weeks to several months (48).

♥ Permanent pacemaker implantation (PPI)

It is typical for patients to have cardiac conduction system interference following TAVI, with new left bundle branch block (LBBB) or total atrioventricular block requiring the implantation of a pacemaker in 5–35% of cases (52). Risk factors have been found to be associated with procedures, devices, and various patient factors including advanced age, male sex, pre-existing conduction disorders (particularly right bundle branch block, RBBB), a small outflow tract, or calcification of the aortic or mitral valve annulus (53).

♥ Infective endocarditis (IE)

Infective endocarditis affects approximately 0.5–3% of patients within the first year following TAVI and has an in-hospital mortality of 30–60% (54, 55). Infections are caused

by Enterococci, which enter the circulation via the gastrointestinal or the genitourinary tract and are the most frequent cause of TAVI-related endocarditis (55).

♥ Coronary obstruction (56) and stent fracture (57)

The risk of coronary obstruction with TAVI is not a novel notion. Aortic stenosis and coronary artery disease commonly coexist, with rates reaching 82% in high-risk individuals(58). A recent Medicare data study(59) revealed that up to 4.7 percent of TAVR patients presented with an acute coronary syndrome over a median follow-up of 297 days. Although this may appear to be a low number, the death rate is disproportionately high, with over one-third of patients dying within 30 days. As more patients opt for TAVR over surgery, it is obvious that coronary access will become a more relevant concern in the long-term treatment of both coronary artery disease and aortic stenosis.

♥ Vascular access

Transfemoral valve delivery is now possible in at least 90% of cases, facilitated by smaller delivery systems and expandable sheaths or by adopting a sheath-free technique. In addition, the frequency of severe vascular complications has decreased to less than 2% (60). Even though not all access methods have been studied thoroughly, retrospective data have indicated that a subclavian access is the safest option for non-femoral access, with comparable results to transfemoral approaches (61).

**1.4.2   Current issues associated with TPVR**

♥ Stent fracture

Despite regular pre-stenting, stent fracture may still typically occur with the Melody valve (5–16%) and is also the most frequent cause for reintervention (62). The following risk factors are linked with stent fracture: young age, high pre- and post-procedural RVOT gradients, small angiographic conduit diameter, stent recoil or compression after deployment, and valve placement directly beneath the sternum (63). Until now, stent fractures have not been reported with the SAPIEN valve.

♥ Conduit rupture/RVOT dissection

RVOT dissection or conduit rupture may occur from wire perforation or balloon inflation because of the possibility of severe morbidity and death. Rupture occurs more often in the presence of highly calcified conduits or homografts, with a frequency of up to 9% as reported in a study, while a pooled meta-analysis has indicated a risk of 4.1% (64).

♥ Valve migration/embolization

Surgical intervention may be required in cases of valve embolization or migration, where

the valve may be retrieved to the inferior vena cava (IVC) and then stented to flatten the valve leaflets; however, this procedure harbors a risk of damage to the RV, TV, and IVC.

♥  Infective endocarditis

The risk of infective endocarditis following TPVR has been estimated to be 5.7%; in most cases, it responds to antibiotics without the need for reintervention (65). In the pathophysiology of post-TPVR endocarditis, a high residual RVOT gradient, consequential turbulence, and in-situ thrombosis have all been identified as contributing factors.

♥  Obstruction of pulmonary blood flow caused by valve displacement into the PA (66)

♥  Coronary ischemia resulting from coronary compression. (67)

## 1.5. The scope of this work

The core components of the TPVR/TAVI and TPVR system can be divided into four parts: stent design, 3D geometry of the heart valve, delivery system, and pre-treatment for crosslinking of the pericardium. As carriers of a heart valve, present-day stents are unable to avoid the above complications. Accordingly, in this dissertation, different functional series of stents are developed using Autodesk Fusion 360 and are then combined with previously prepared animal pre-CT 3D reconstructions to obtain the stents' radial force, life, and hoop force in Ansys 2021 R2. In this work, the stent designs are named DGS which stand for "Deutsches Herzzentrum Berlin- GrOwnValve Stent". This study is the first to conceptualize anatomical functional stent designs for autologous heart valve mounting in the context of TPVR. The aim of this work is to describe and illustrate key functional design features of the new stents for future use in transcatheter autologous pulmonary valve replacement with 3D model simulation, making the suture procedure reproducible and effective for the real-time application in the operating room.

## 2. Methods

### 2.1. Animal cardiac CT acquisition and 3D reconstruction in 3D Slicer

### 2.1.1 Intravenous anesthesia for cardiac CT

All cardiac CT data were acquired from GrOwnValve preclinical trials (IVC113-G 0062/18) in a translational sheep model with the approval of the legal and ethical committee of the State Office for Health and Social Affairs, Berlin (LAGeSo). All animals received humane care in compliance with the guidelines of the European and German Societies of Laboratory Animal Science (FELASA, GV-SOLAS). In addition, cardiac CTs from 21 animals were reconstructed using the open-source software 3D Slicer. Anesthetic set-ups (68) were performed at Forschungseinrichtungen für Experimentelle Medizin (FEM)-Campus Virchow-Klinikum Charité – Universitätsmedizin Berlin.

❖ Sheep (young adult sheep, 47.4 ± 5.8 kg, female, *Ovis aries*) were tranquilized with premedication of midazolam (2 mg/mL, 0.4 mg/kg), butorphanol (10 mg/mL, 0.4 mg/kg) and glycopyrronium bromide (200 mcg/mL, 0.011 mg/kg) by intramuscular injection.

❖ After 15 min of injection, the physical condition was checked once the sheep became docile.

❖ An 18 G catheter with an injection port was placed aseptically in the cephalic vein with perfusion lines joined to a T-connector for anesthesia and contrast agent.

❖ The sheep were anesthetized through intravenous injection of propofol (20 mg/mL, 1-2.5 mg/kg) and fentanyl (0.01 mg/kg).

❖ The sheep were checked for symptoms of tranquilization like jaw relaxation, loss of the swallowing and the ciliary reflex.

❖ The sheep were intubated with a 6.5-8 mm tracheal tube and a gastric tube was placed into the stomach for gastric fluid aspiration followed by an intravenous injection of propofol (20 mg/mL, 1-2.5 mg/kg) and fentanyl (0.01 mg/kg).

❖ Total anesthesia was achieved by intravenously injecting propofol (10 mg/mL, 2.5-8.0 mg/kg/h) and ketamine (10 mg/mL, 2-5 mg/kg/h) in preparation for cardiac CT.

### 2.1.2 Cardiac CT protocol

All animal CTs were performed at DHZB following the steps below (68).

❖ The sheep were transferred from Forschungseinrichtungen für Experimentelle Medizin to the CT room of the DHZB after the preparations. All sheep were scanned in the prone position after securely fixing them on the CT bed with three bandages on the forelimbs, abdomen, and hind limbs.

❖ Cardiac CT was performed on a 64-slice dual-source multidetector CT system with

ECG gating. The standard acquisition technical parameters were set as follows: gantry rotation time 0.33 s, 100-320 mAs per rotation, 120 kV tube voltage, matrix 256 with a 16-bit depth, deviation effective X-ray dose 15.5±11.6 mSv, slice thickness 0.75 mm.

❖ Contrast enhancement was achieved by administering 2-2.5 mL/kg of iodinated contrast agent at a rate of 5 mL/s via the T-connector on the forelimb.

❖ The 4D CT scanning protocol was performed sequentially. The entire cardiac cycle was divided into eleven frames from 0% to 100% with 10% R-wave to R-wave (R-R) intervals covering the cardiac cycle. An end-diastolic phase was carried out at approximately 70% of the R-R interval for analysis for the 3D series. Sagittal, coronal, and axial data were obtained in each frame of the 4D CT, as well as in 70% of the 3D series.

❖ A bolus tracking method was used for contrast bolus timing in the region of interest on the main pulmonary artery to achieve ideal synchronization. No beta-blockers were administered to any of the sheep.

❖ The sheep were transferred back to the FEM and the perfusion of propofol, and ketamine was stopped after scanning. The sheep regained consciousness 10-20 min after extubation.

❖ Anesthesiologists and veterinarians oversaw the entire anesthesia treatment until the sheep were fully awake and able to move freely.

### 2.1.3 Cardiac CT data loading into 3D Slicer

All cardiac CT data were loaded into 3D Slicer as DICOM files with the pre-check function using the advanced manual in the software. The "Crop Volume" function in the "Module" was then used to obtain the desired CT series (50-70% valve reconstruction in general) in order to create a new annotation ROI combined by selecting "Interpolated cropping" and "Isotropic spacing". The spacing scale was then set at 1.00x to adjust the ROI in the CT images to the appropriate range.

### 2.1.4 Cardiac CT segmentation settings

Various segmentations were created for different sections of the heart in the "Segment Editor" module: Aorta→ Hollowed aorta→ Aortic root→ Aortic root tube→ Aortic valve, Left ventricle→ Left ventricular myocardium, Left atrium→ Left atrial myocardium, Right ventricle→ Right ventricular myocardium, Right atrium→ Right atrial myocardium, SVC+IVC, Pulmonary artery→ Hollowed pulmonary artery→ Pulmonary root→ Pulmonary arterial tube→ Pulmonary valve, Left heart, Right heart, Heart and the stent (post-CT). The "Four-Up" scene Axial+Sagittal+Coronal+3D was used to paint different

parts of the heart with the settings "Sphere brush", editable area "Everywhere", editable intensity range and "Allow overlap" to modify the other segments' function. A single segment was then selected to paint slice-by-slice, but only for the shape of the aortic valve and the pulmonary valve. After painting the two valves, a larger sphere brush diameter was used to paint the rest of the great vessels. It is preferable to use the three views of the images for tracking the pulmonary artery, pulmonary vein, and aorta.

After painting the two great vessels, the painting sequence should be continued as follows: SVC+IVC→ Left atrium→ Right atrium. The margins of these structures will be used to paint the two ventricles.

### 2.1.5 Smoothing methods in 3D Slicer

Smoothing methods include "Closing" (2-3mm), "Median" (1-2mm), and "Gaussian" (1-2mm). The "Editable Button" should be closed first; otherwise, smoothing can only be performed with a limited intensity range. It is recommended to smooth the aorta first, followed by tracking the right and left coronary arteries slice-by-slice for coronary artery painting, as well as for the small branches of the pulmonary artery and pulmonary vein.

### 2.1.6 Myocardial segmentation settings

After creating the 3D models of the left and right chambers, the "Hollow" function in the Segment Editor module was applied to build shells for the four chambers to mimic the myocardium (depending on the thickness of each chamber): left and right atriums (1-1.5 mm), left ventricle (6-10 mm), and right ventricle (4-8 mm).

### 2.1.7 Computational cutting of the aortic and pulmonary valves

"Logical operators" was used in the segmentation module to create the aortic root, hollowed aortic root, aortic valve, pulmonary artery root, hollowed aortic root, and pulmonary artery. The "Hollow" function was then used to create a shell for the two major vessels with a thickness of 1-1.5 mm. Next, the hollowed aortic and pulmonary root were erased using a sphere brush (1-2 mm) according to the valvular margins in the CT images. After erasing, a 1-2 mm sphere brush was used to create the free edges and commissures of the two heart valves. Regarding the aortic valve 3D model, the right and left coronary arteries were kept in the hollowed root models.

### 2.1.8 Saving and exporting 3D segmentation files

All segmentations were saved in the CT DICOM folder in the formats MRML and NRRD and exported into the STL format for 3D printing in our lab.

In this monography, the animal J Pre-CT was chosen to illustrate the procedure of the 3D reconstruction in 3D Slicer.

### 2.2. Functional stent designs in Fusion 360 (Educational Version)

### 2.2.1  2D sketch drawings of functional stents

2D sketches were created on the basis of the various design ideas. Both the width and depth of the frame were 0.3 mm. In this study, all stents were designed with a diameter of 30 mm and divided into different functional segments to mount a 30-mm diameter new tri-leaflet pulmonary valve with a Nitinol shape-memory self-expandable frame.

### 2.2.2  Groups of functional stents in general and their 3D shaping

The functional stents were designed using Autodesk Fusion 360, and were divided into three morphological geometries, The material of the DGS stents used in Fusion 360 was satin steel whose bending factor (K-factor is 0.44) because there were no Nitinol properties in the educational version of Fusion 360. After creating and exporting the 3D models of the DGS stents, the Nitinol properties were applied for the stent simulations which are illustrated below.

♥  **Group 1**– Straight tubular stents to host an autologous pulmonary valve (APV) with a circular opening orifice: DGS-3, DGS-5, DGS-7, DGS-8B, DGS-10B, DGS-12D.
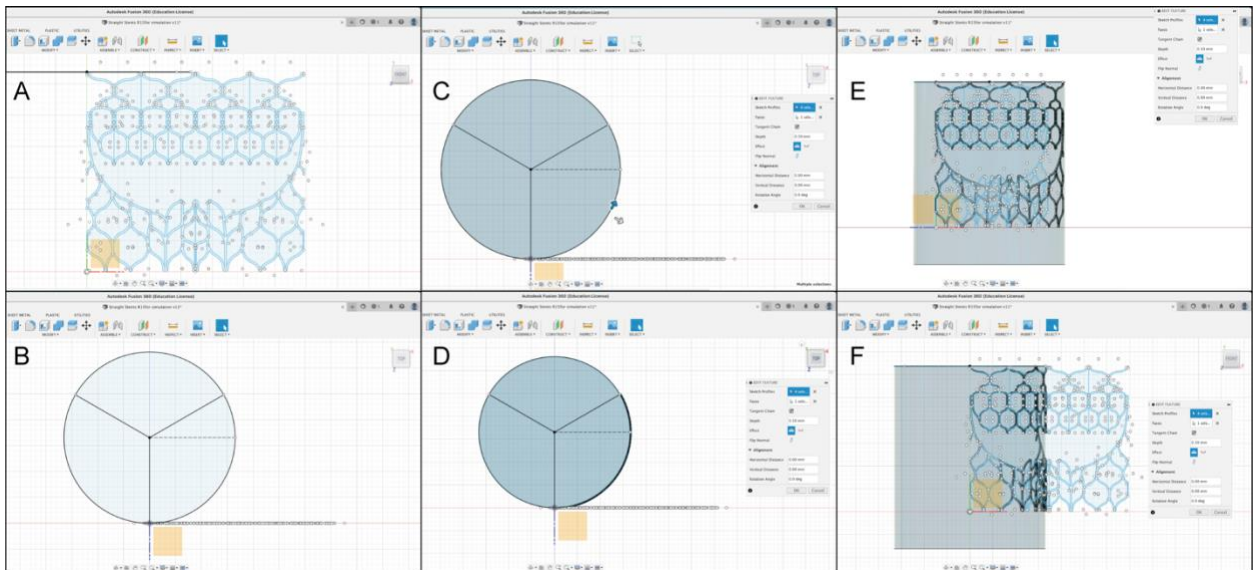


**Figure 4. Representative illustration of stent design (DGS-12D) in Group 1. A:** Front view of the 2D stent sketch; **B**: Circular tract for 2D sketch embossing; **C**: Cylindrical template created by extruding the circular tract before 2D stent sketch embossing; **D-F**: Cylindrical template created by extruding the circular tract after 2D stent sketch embossing (Top, main, and front views).

For the straight circular stent, a circle with the desired diameter was drawn as the tract for length for the 2D sketch emboss. The embossing depth **(Figure 4C)** ranged from 0.3 m to 4 mm depending on the location of the stent. The cylinder was embossed with a third of the circumference of the stent's 2D sketch. After embossing, the cylinder was extruded as "shearing" from the stent embossing. 1/3 model of the stent was then

visualized on the platform. The circle was divided into three equal fan shapes at a 120º angle. The fan shape margins were subsequently used to build faces for the mirror of the 1/3 model. Afterward, a straight circular stent was established, and the mirror function was then applied in the software. **Figure 4 and Figure 5.**
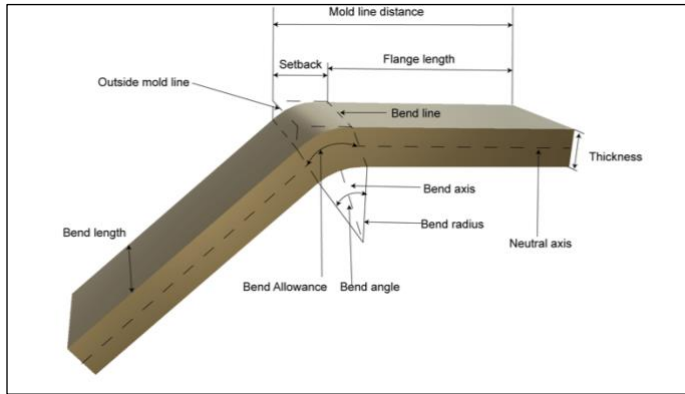


**Figure 5.** **Calculation of bend allowance.**

**At** = bend allowance (mm),

**A** = bend angle (radian),

**R** = 0.3 mm bend radius,

**T** = 0.3 mm sheet thickness,

**K** = 0.44 bend factor calculate.

❖ **DGS-3** was divided into three functional segments. **Figure 6**.
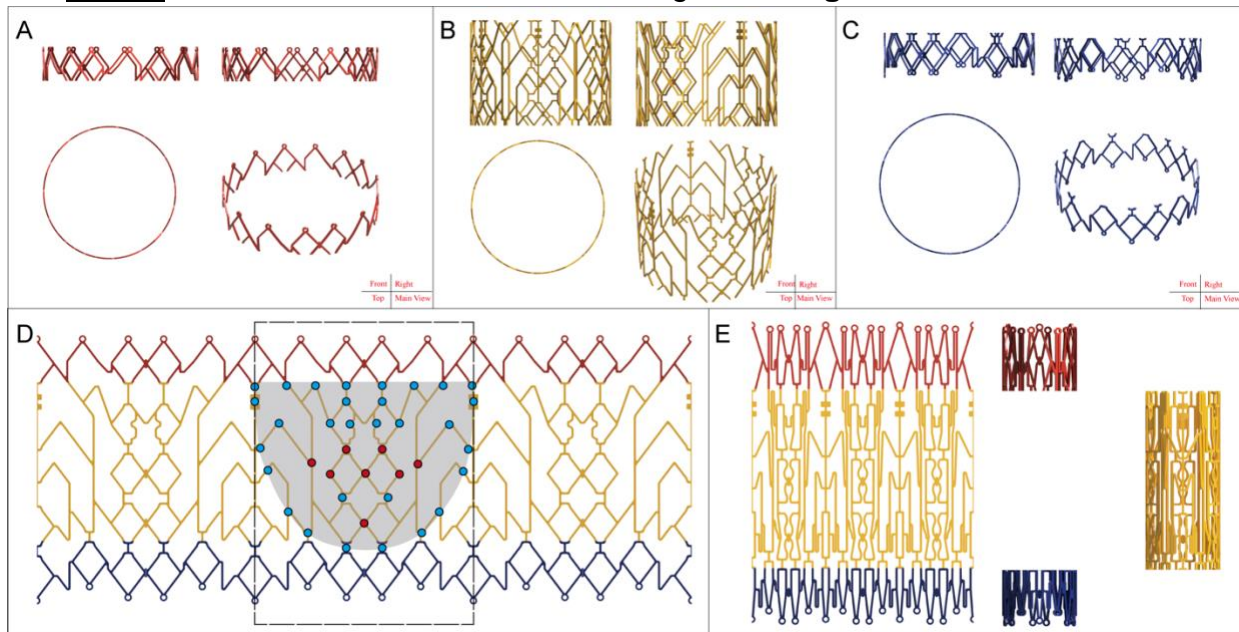


**Figure 6. The architectures of DGS-3.**
**A:** Top segment for pulmonary artery anchoring; **B:** Circular middle segment for the two suture lines at the commissural horizontal and support struts in every leaflet edge to host new leaflets; **C:** Segment for RVOT anchoring; **D:** Expanded 2D sketch illustration with a virtual heart valve; **blue dots** are the suture points at the APV edges to the stent, **red dots** are the suture points on the APV conduit to the stent or the potential suture points to the stent; **E:** Crimped 2D and 3D illustration.

**Segment I:** This segment was designed for PA anchoring with V-shaped struts with six connective zones to link to segment II for each new leaflet to maintain a stable radial force and hoop force following deployment.

**Segment II:** New leaflet loading zones with two specific suture lines at the commissural horizontal and fixation points for hosting the edges of the new leaflets. Every leaflet edge has balanced support struts for the three leaflets hosting, and each leaflet can be sutured

at eleven specified suture sites aligned in the grids. There are also 8 potential suture locations to further fixate every leaflet if the mounting requires tightening.

**Segment III:** For RVOT anchoring with six symmetrical struts connecting to segment II.

❖ **DGS-5** also had three functional segments, **Figure 7**.
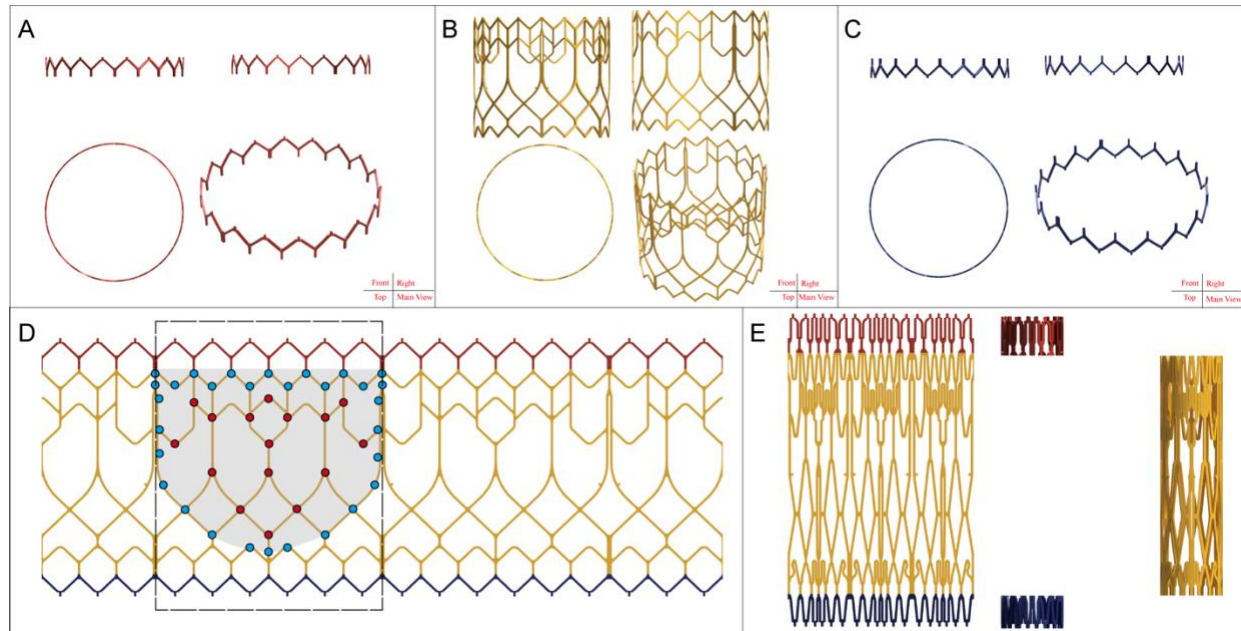


**Figure 7. The architectures of DGS-5.**
**A:** Top segment for pulmonary artery anchoring; **B:** Circular middle segment for the two suture lines at the commissural horizontal and support struts in every leaflet edge to host new leaflets; **C:** Segment for RVOT anchoring; **D:** Expanded 2D sketch illustration with a virtual heart valve; **blue dots** are the suture points at the APV edges to the stent, **red dots** are the suture points on the APV conduit to the stent or the potential suture points to the stent; **E:** Crimped 2D and 3D illustration.

**Segment I:** This segment was designed to assist the stented heart valve to anchor onto the PA with 18 Y-shaped struts as well as three strong struts linked to the three commissures.

**Segment II:** Middle segment with specific symbols at the commissural horizontal and mellifluous support struts for hosting new leaflets as well as four mellifluous support struts in every leaflet edge for hosting new leaflets. Each leaflet can be sutured at eleven specific suture points aligned in the grids. Furthermore, the stent had 16 potential suture points for extra fixation for tighter mounting.

**Segment III:** This segment was used for anchoring onto the RVOT with large open-cell architectures linked to segment II.

❖ **DGS-7** had four functional segments to support its performance, **Figure 8**.

**Segment I:** This segment was designed for PA anchoring with 18 symmetrical large open cells along the circumference with two conterminous zones that linked with cells in segment II.

**Segment II:** This segment had "Y" and "人" joints of cells at the commissural horizontal as sewing symbols. The diamond cell in the third layer of the stent for native heart valve compression provides the new heart valve with enough space to deliver its action during the cardiac cycle as well as secure its cylindrical geometry.

**Segment III:** This segment was designed for new PV mounting with 13 specific suture points for each leaflet. It was equipped with five simplified support struts to connect along segment IV to ensure the integrity of the stent as a whole.

**Segment IV:** This segment was designed to assist the stent in anchoring onto the RVOT with symmetrical cells and had three small cells as hooks at the bottom part that were 120° to one another.
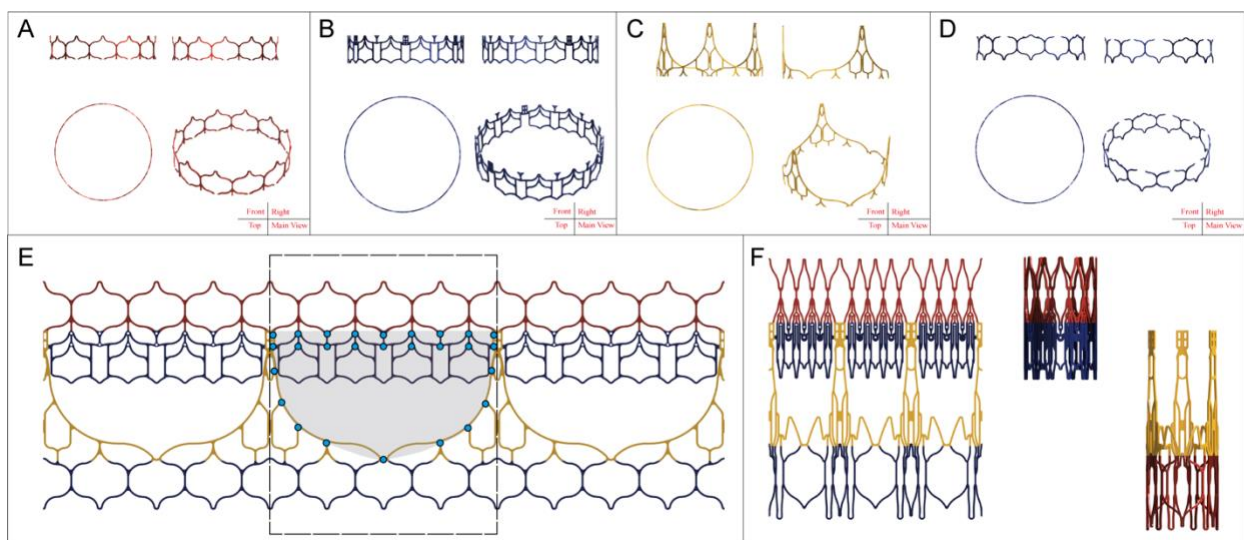


**Figure 8. The architectures of DGS-7.**
**A:** Top segment for pulmonary artery anchoring; **B:** Circular middle segment for the two suture lines at the commissural horizontal and native heart valve compression; **C:** Segment III for new heart valve sewing with simplified support structures; **D:** Segment for RVOT anchoring; **E:** Expanded 2D sketch illustration with a virtual heart valve; **blue dots** are the suture points at the APV edges to the stent, the **red arrow** shows the retrieval cell that can be connected with the delivery system for APV repositioning; **F:** Crimped 2D and 3D illustration.

❖ **DGS-8B** had four functional segments without any outstretched arms or crowns at the top, middle and RVOT, **Figure 9**.

**Segment I:** This segment consisted of 12 large X-shaped open-cell struts, each of which had three struts to connect to segment II to ensure the integrity of the stent, which can be aligned towards the pulmonary trunk.

**Segment II:** This segment consisted of two functional parts: Two circular suture lines at the commissural horizontals with 0.3-mm diameter holes for 5-0 polypropylene for running or interrupted sutures, and three vertical arms to secure the artificial heart valve and to compress the native leaflets.

**Segment III:** This segment was designed for hosting the new heart valve and consisted of three functional parts: 1. Nine specific suture points for each leaflet at approximately equal distance, 2. symmetrical support struts for sewing the leaflets, and 3. hook position for repositioning a stented heart valve.

**Segment IV:** This segment consisted of 12 large X-shaped open-cell struts with 15 struts to connect to segment III to ensure the integrity of the stent, which can be aligned to the RVOT.
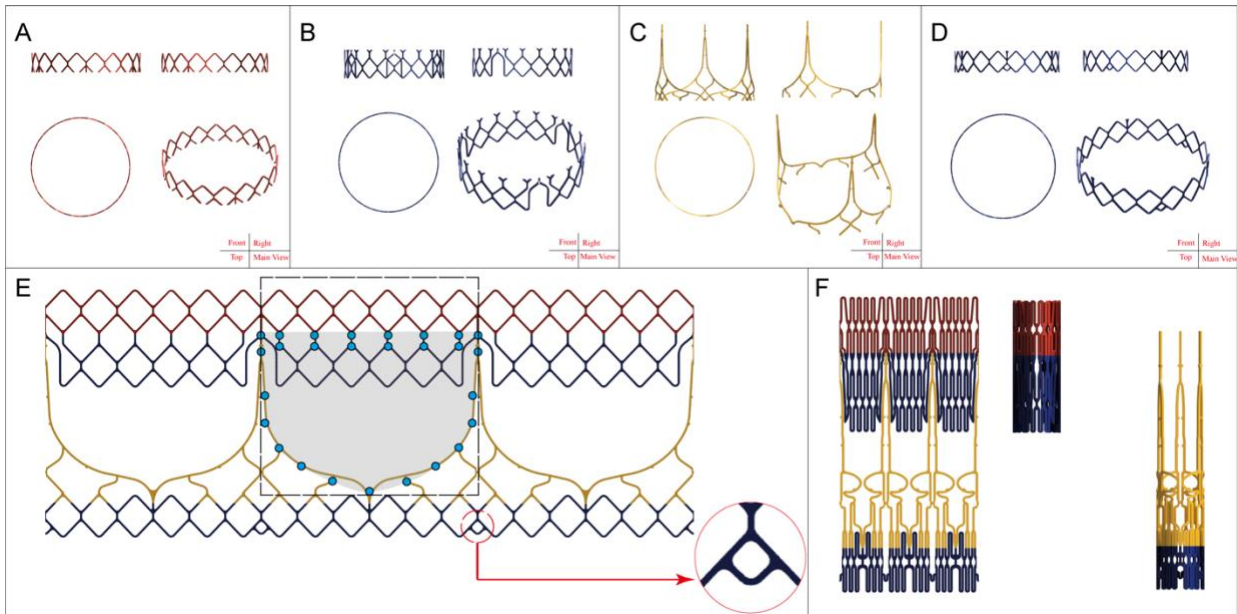


**Figure 9. The architectures of DGS-8B.**
**A:** Top segment for pulmonary artery anchoring; **B:** Circular middle segment for the two suture lines at the commissural horizontal and native heart valve compression; **C:** Segment III for sewing the new heart valve with simplified support structures; **D:** Segment for RVOT anchoring; **E:** Expanded 2D sketch illustration with a virtual heart valve; **blue dots** are the suture points at the APV edges to the stent; **F:** Crimped 2D and 3D illustration.

❖ **DGS-10B** was designed with four functional segments without a crown to host a tri-leaflet heart valve, **Figure 10**.

**Segment I:** This segment had 12 large open X-shaped cells with a coaxial alignment in accordance with segment II-IV.

**Segment II:** This segment consisted of two functional parts: Two horizontal sewing lines for fixing a tri-leaflet heart valve onto the stent with a circular geometry and three vertical arms to compress the native leaflet.

**Segment III:** This segment was comprised of two functional parts: Approximate determinate suture points for hosting the leaflets and a strong asymmetrical support frame with retrieving struts for stent repositioning.

**Segment IV:** This segment was designed for RVOT anchoring with a vertical geometry.
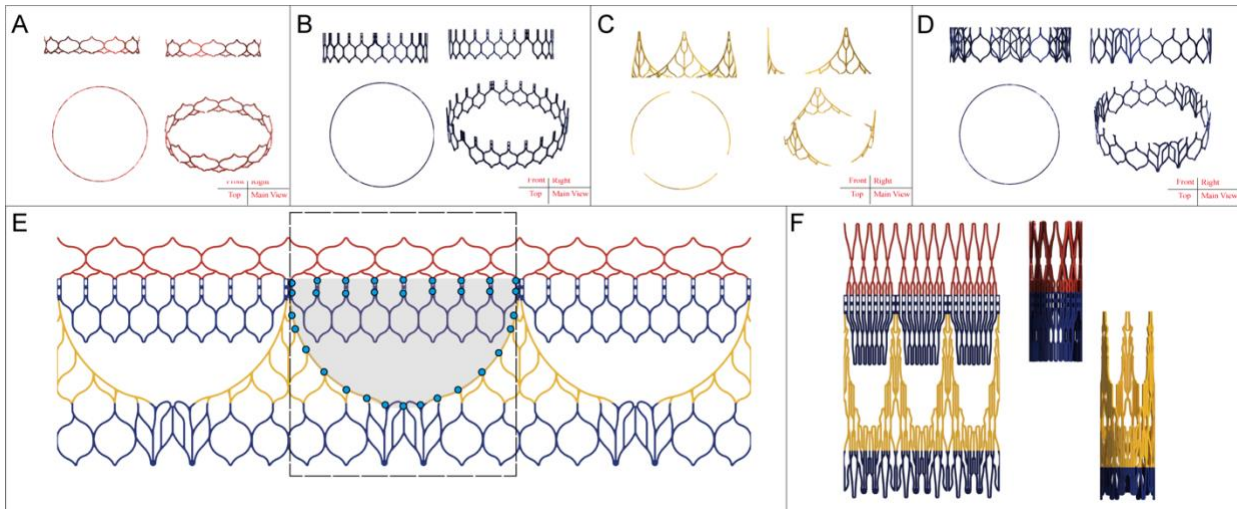
**Figure 10. The architectures of DGS-10B.**
**A:** Top segment for pulmonary artery anchoring; **B:** Circular middle segment for the two suture lines at the commissural horizontal and native heart valve compression; **C:** Segment III for sewing the new heart valve with simplified support structures; **D:** Segment for RVOT anchoring; **E:** Expanded 2D sketch illustration with a virtual heart valve; **blue dots** are the suture points at the APV edges to the stent; **F:** Crimped 2D and 3D illustration.

❖ **DGS-12D** had four functional segments to ensure its performance during implantation, **Figure 11**.
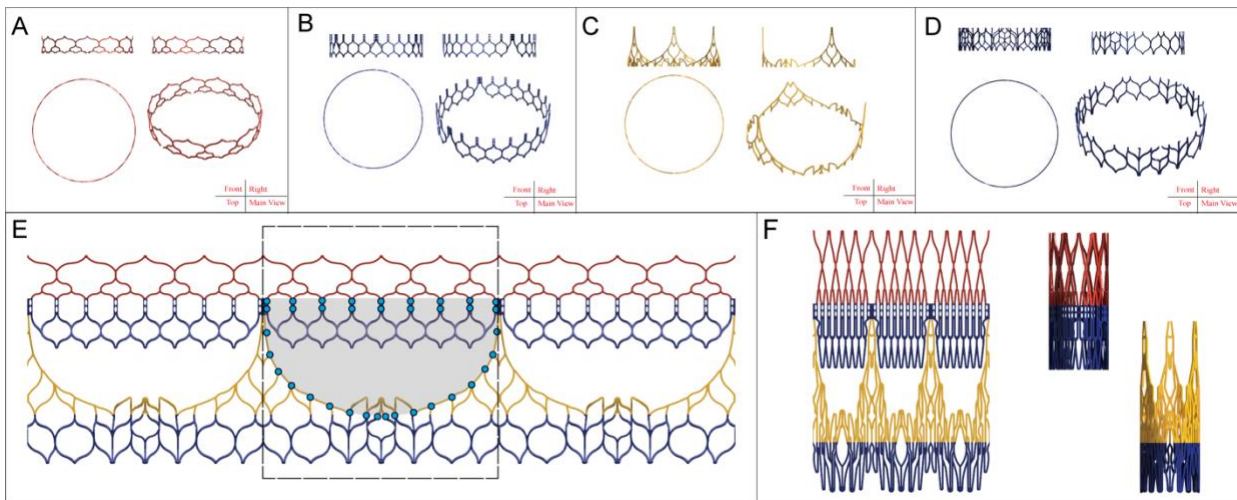


**Figure 11. The architectures of DGS-12D.**
**A:** Top segment for pulmonary artery anchoring; **B:** Circular middle segment for the two suture lines at the commissural horizontal and native heart valve compression; **C:** Segment III for sewing the new heart valve with simplified support structures; **D:** Segment for RVOT anchoring; **E:** Expanded 2D sketch illustration with a virtual heart valve; **blue dots** are the suture points at the APV edges to the stent; **F:** Crimped 2D and 3D illustration.

**Segment I:** This segment had 12 large open X-shaped cells with a coaxial alignment for anchoring at the MPA, with three struts connected with the two commissural horizontal suture lines to maintain the strength of the stent.

**Segment II:** This segment was composed of two functional parts: Two suture lines at the commissural horizontal for heart valve fixation and three vertical arms to guard the leaflets

and compress the native leaflets.

**Segment III:** This segment had three functional segments: An asymmetrical support frame with approximate determinate suture points and three guard arches for the basal segment of the leaflets. Furthermore, structures at the second suture point connections between the two leaflet junctions below the three commissures can be used as a hook-connect point with the delivery system to reposition the stented heart valve.

**Segment IV:** This segment was designed for anchoring onto the RVOT with 30 asymmetrical cells which connected to segment III.

♥ **Group 2**– Corollaceous stents to host an autologous pulmonary valve with a circular opening orifice: DGS-8A, DGS-9A, DGS-10A, DGS-12C.

For these three circular stents with outstretched arms, the "sheet metal" method was used to bend the 2D solid bodies after extruding the 2D sketch in 0.3 mm as the thickness of the stents, **Figure 5**. The bend allowance for a bending process was calculated with the following **Equation 1**. After obtaining the desired bending model with different parameters, all solid bodies were combined together to acquire 1/2 model of the stent. Afterward, a whole stent model was created using the mirror function in the software, **Figure 12**.
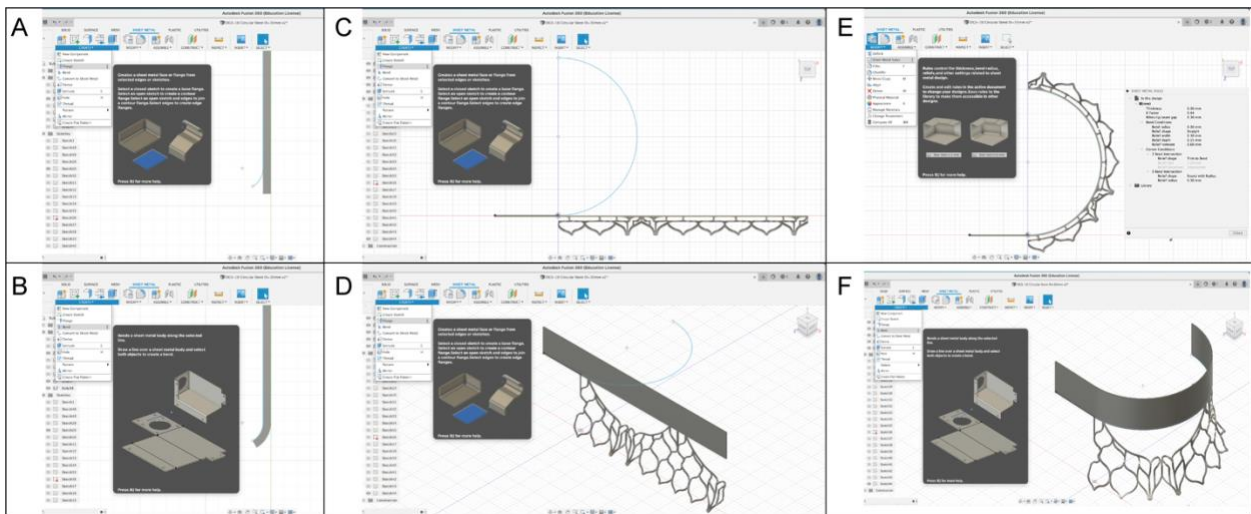


**Figure 12. Representative illustration of stent design (DGS-12C) in Group 2. A-B**: Outstretched arm before sheet metal with sheet metal sketch; **C-D**: RVOT crown before sheet metal with sheet metal sketch; **D-F:** RVOT crown after sheet metal with sheet metal sketch. RVOT- right ventricular outflow tract.

$$At = A(R + K * T) \qquad (1)$$

❖ **DGS-8A and DGS-9A**

DGS-8A had the same design concept as DGS-9A, which consisted of four functional components: 1. Top lotus crown for pulmonary artery anchoring, 2. middle crown for native leaflet compression and two suture lines at the commissural horizontal, 3.

symmetrical support architectures for suturing new leaflets, and 4. basal crown for RVOT anchoring, **Figure 14** and **Figure 13**.
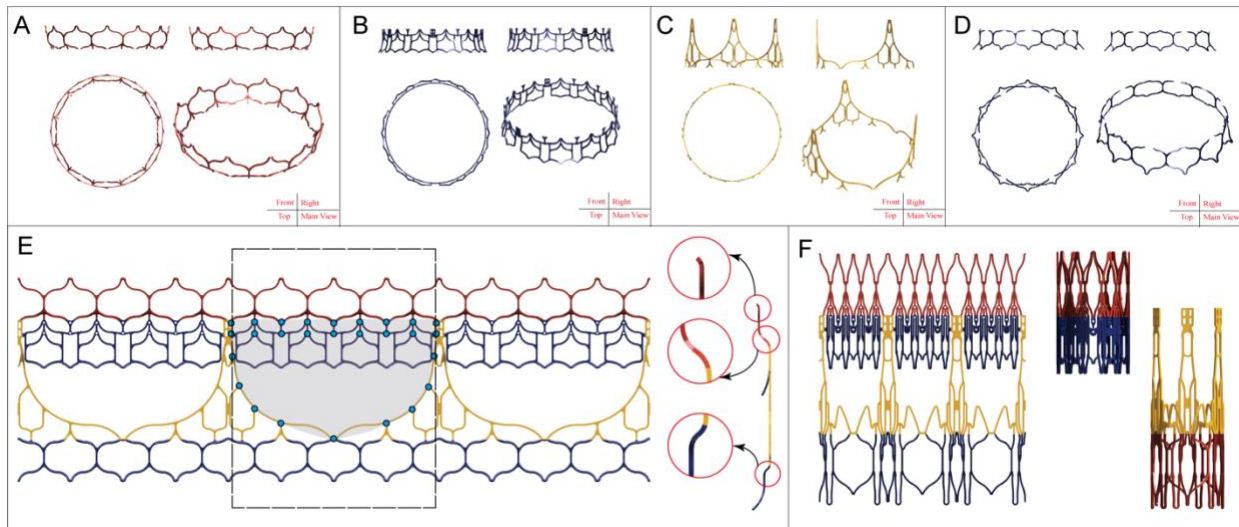


**Figure 14. The architectures of DGS-8A.**
**A:** Top crown with tiny outstretched arms for pulmonary artery anchoring; **B:** Circular middle portion for the two suture lines at the commissural horizontal and native heart valve compression; **C:** Portion III for sewing the new heart valve with strong support structures; **D:** Crown for RVOT anchoring; **E:** Expanded 2D sketch illustration with a virtual heart valve; **blue dots** are the suture points at the APV edges to the stent, the three **black arrows** show the outstretched arms and crown which are the major difference from DGS-9A, and two guard layers at the RVOT crown; **F:** Crimped 2D and 3D illustration.
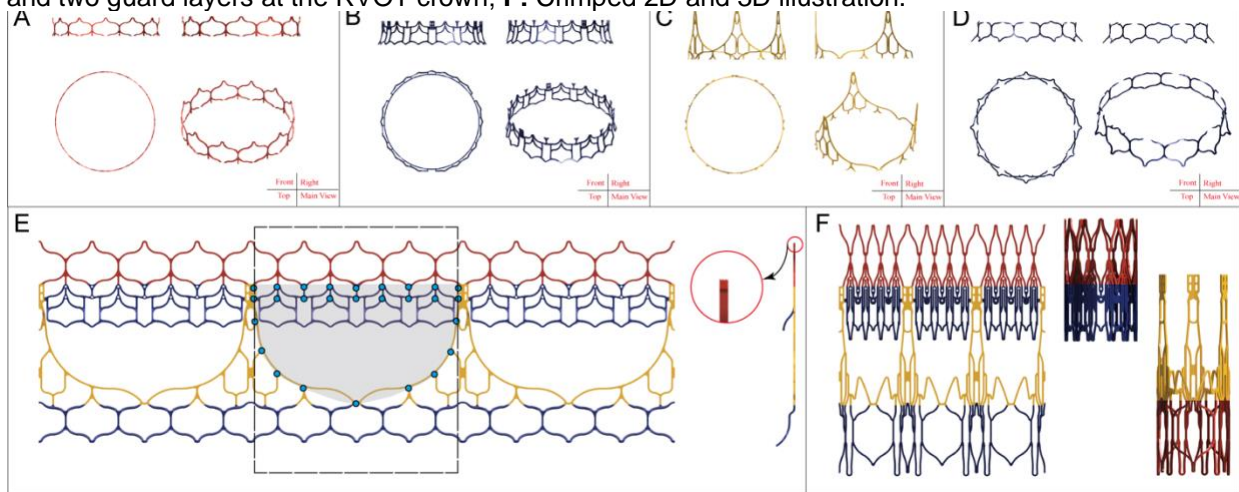


**Figure 13. The architectures of DGS-9A.**
**A:** Top crown without tiny outstretched arms for pulmonary artery anchoring; **B:** Circular middle portion for the two suture lines at the commissural horizontal and native heart valve compression; **C:** Portion III for sewing the new heart valve with strong support structures; **D:** Crown for RVOT anchoring; **E:** Expanded 2D sketch illustration with a virtual heart valve; **blue dots** are the suture points at the APV edges to the stent, the **black arrows** shows the vertical crown which is the major difference from DGS-8A; **F:** Crimped 2D and 3D illustration.

DSG-8A and DGS-9A differed from one another in the design philosophy of the top lotus crown. The top crown of DGS-8A was designed to be 34 mm in diameter, with a 2-mm offset from the core segment hosting the 30-mm diameter new heart valve for greater dilation of the pulmonary artery. Furthermore, at the top of this crown, tiny-outstretched arms were present at the distal end of the cells with a 0.2-mm offset from the top crown.

This design was meant to ensure better anchoring at the pulmonary artery and prevent stented heart valve migration throughout the cardiac cycle.

**Segment I:** The distal perpendicular crown aligned to the pulmonary trunk consisted of 12 large open-cell struts. Each X-shaped cell had three struts to connect with segment II to ensure the integrity of the stent.

**Segment II:** This segment comprised two functional parts: Two circular suture lines at the commissural horizontals with 0.3-mm diameter holes for 5-0 polypropylene for running or interrupted sutures, and three outstretched arms which were offset 1.5 mm from the diameter of the top crown and segment III for the security of the artificial heart valve and compression of native leaflets.

**Segment III:** This segment was designed to host the new heart valve and included three functional parts: 1. Nine specific suture points for each leaflet at approximately equal distance, 2. symmetrical support struts for sewing the leaflets, and 3. hook position for stented heart valve repositioning. Each leaflet had nine equal distances for sewing onto the stent using running or interrupted sutures.

**Segment IV:** This segment was designed for RVOT anchoring with two guard layers. The first layer can be anchored at the basal horizontal of the native valve, while the second layer can heal the stented heart valve anchor at the RVOT.

❖ **DGS-10A** was designed with four functional segments with three crowns to host a tri-leaflet APV for TaPVR, **Figure 15**.
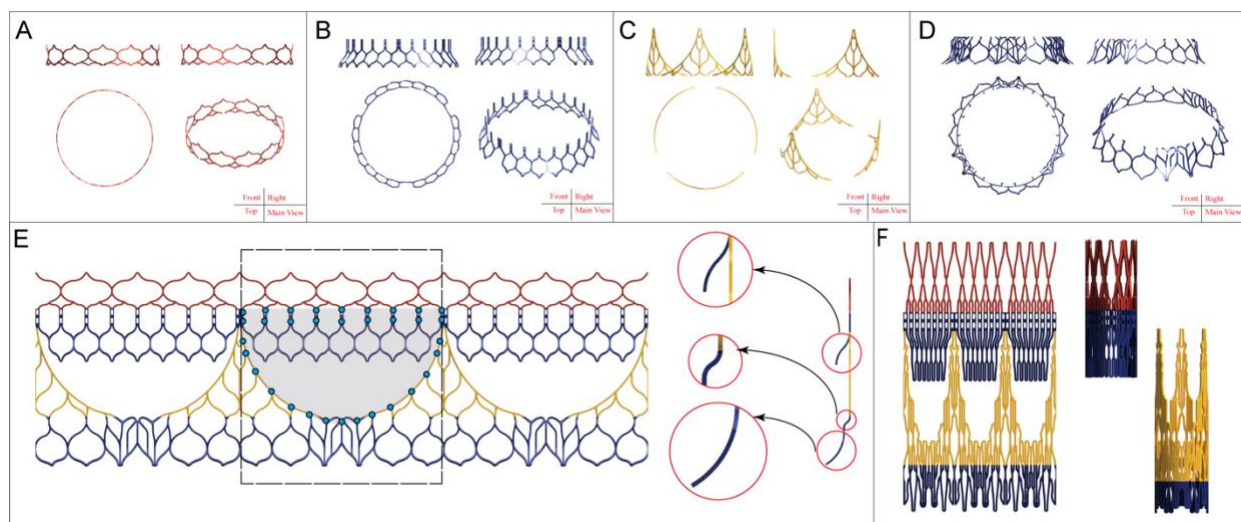


**Figure 15. The architectures of DGS-10A.**
**A:** Top crown with vertical crown for pulmonary artery anchoring; **B:** Circular middle segment for the two suture lines at the commissural horizontal and native heart valve compression; **C:** Segment III for sewing the new heart valve with strong support structures; **D:** Crown for RVOT anchoring; **E:** Expanded 2D sketch illustration with a virtual heart valve; **blue dots** are the suture points at the APV edges to the stent, the **black arrows** show the outstretched arms, two guard layers for RVOT anchoring; **F:** Crimped 2D and 3D illustration.

**Segment I:** The distal crown to the PA had 12 large open X-shaped cells with a coaxial alignment in accordance with segment II-IV, thus offering ideal blood flow conduction for TOF patients. These large cells were concatenated with the copular struts from segment II, which can help keep the stent still during the whole cardiac cycle.

**Segment II:** This segment consisted of two functional parts: Two horizontal sewing lines for tri-leaflet PV fixation onto the stent with a circular geometry and protracted arms with a 2-mm offset from the central diameter (30 mm) for compressing the native leaflet to provide ideal space for endoprosthesis valve opening.

**Segment III:** This segment was comprised of two functional parts: Approximate determinate suture points for hosting the leaflets and a strong asymmetrical support frame with retrieving struts for stent repositioning. Each leaflet frame had 17 sewing points at approximately equal distances ranging from 2.7 mm to 3.1 mm. Compared to the DGS-12 series, the DGS-10 series lacked three guard arches at the basal segment.

**Segment IV:** This segment was designed for RVOT anchoring with two layers of offset (0.5 mm and 3.5 mm) from the central stent diameter.

❖ **DGS-12C** was designed with four functional segments with four crowns to host a tri-leaflet APV for TaPVR, **Figure 16**.
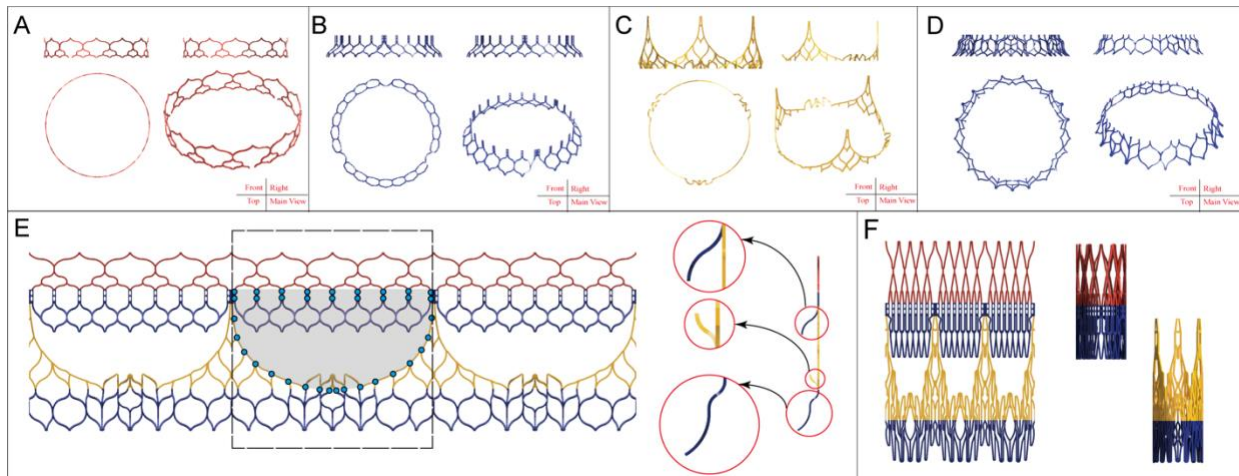


**Figure 16. The architectures of DGS-12C.**
**A:** Top crown for pulmonary artery anchoring with a circular geometry; **B:** Circular middle crown for the two suture lines at the commissural horizontal and native heart valve compression; **C:** Segment III for sewing the new heart valve with three guard arches at the basal part with a circular shape; **D:** Crown for RVOT anchoring; **E:** Expanded 2D sketch illustration with a virtual heart valve; **blue dots** are the suture points at the APV edges to the stent, the **black arrows** show the outstretched arms at segments II and III, two guard layers for RVOT anchoring; **F:** Crimped 2D illustration.

**Segment I:** The distal crown to the PA had 12 large open X-shaped cells with nine connecting struts to segment II to keep the stent still during the whole cardiac cycle.

**Segment II:** The middle crown of DGS-12C had a circular design with the same diameter

as the top crown and the top of the RVOT crown. It consisted of two functional parts: Two suture lines at the commissural horizontal for heart valve fixation and three outstretched arms to guard the leaflets and compress the native leaflets. The two suture lines provided adequate space for surgeons to suture the heart valve at the commissural horizontal with running or interrupted sutures using 5-0 polypropylene.

**Segment III:** This segment was for the new APV, which comprised two functional segments: Asymmetrical support frames with approximate determinate suture points and three guard arches for the basal segment of the leaflets. Each leaflet frame had 17 sewing points at approximately equal distances, providing the surgeon with determinate suture points during the surgery for running or interrupted sutures. The three guard arches had four functions: 1. to protect the basal segment of the heart valve from blood flow, 2. to compress the native heart valve in order to provide the new heart valve with enough space, 3. to prevent the stented heart valve from migrating towards the pulmonary artery as well as to the RVOT, 4. to provide a connection between the two leaflet junctions below the three commissures at the second suture point, which can be used as a hook-connect point with the delivery system to reposition the stented heart valve in case of stent malposition.

**Segment IV:** This segment was designed for RVOT anchoring and comprised two slick secure layers to help the stented APV adhere to the RVOT without interrupting cardiac conduction bundles and other cardiac structures at the RVOT.

♥ **Group 3**– Corollaceous stents with an elliptic geometry to host an APV with an elliptic opening orifice: DGS-12A, DGS-12B.

The top crown for the oval stent, which possesses a circular geometry to the pulmonary artery side and an oval geometry at the commissural horizontal line, was created using the "lofting" function with smooth tracts between the top parts and the basal parts. The RVOT crown and the native leaflet compressing parts were created according to the following steps, **Figure 17**:

The 2D sketch was embossed to the cylinder (0.3- 4 mm, depending on the different structures) with the desired diameter for the heart valve, after which the cylinder was sheared from the 3D stent; A template was created for the stent geometry as the inner face for the stent; 0.3 mm was offset from the template surface to create a shell for the outer surface of the stent; The outer surface of the stent was replaced into the shell so as to create the final surface of the stent; The inner surface was replaced into the template for the inner surface of the stent; A stent was then visualized on the screen.

❖ **DGS-12A and DGS-12B** were designed with a top-down deployment, allowing precise positioning in various RVOT and pulmonary artery anatomies with favorable blood flow conduction, and were designed for an "anatomical" oval tri-leaflet pulmonary valve. Owing to the asymmetrical nature of the ovality, there were two designs of the three commissural attachments to the stents; therefore, the difference between DGS-12A and DGS-12B was the position of one of the commissures sutured into the stent at the long axis or the short axis of the ovality. The circumference of the ovality was obtained using **equations 2 and 3**.

$$C \approx \pi(a + b)\left(1 + \frac{3h}{10 + \sqrt{4 - 3h}}\right) \qquad (2)$$

$$h = \frac{(a - b)^2}{(a + b)^2} \qquad (3)$$

**a: long radius, b: short radius, c: circumference**
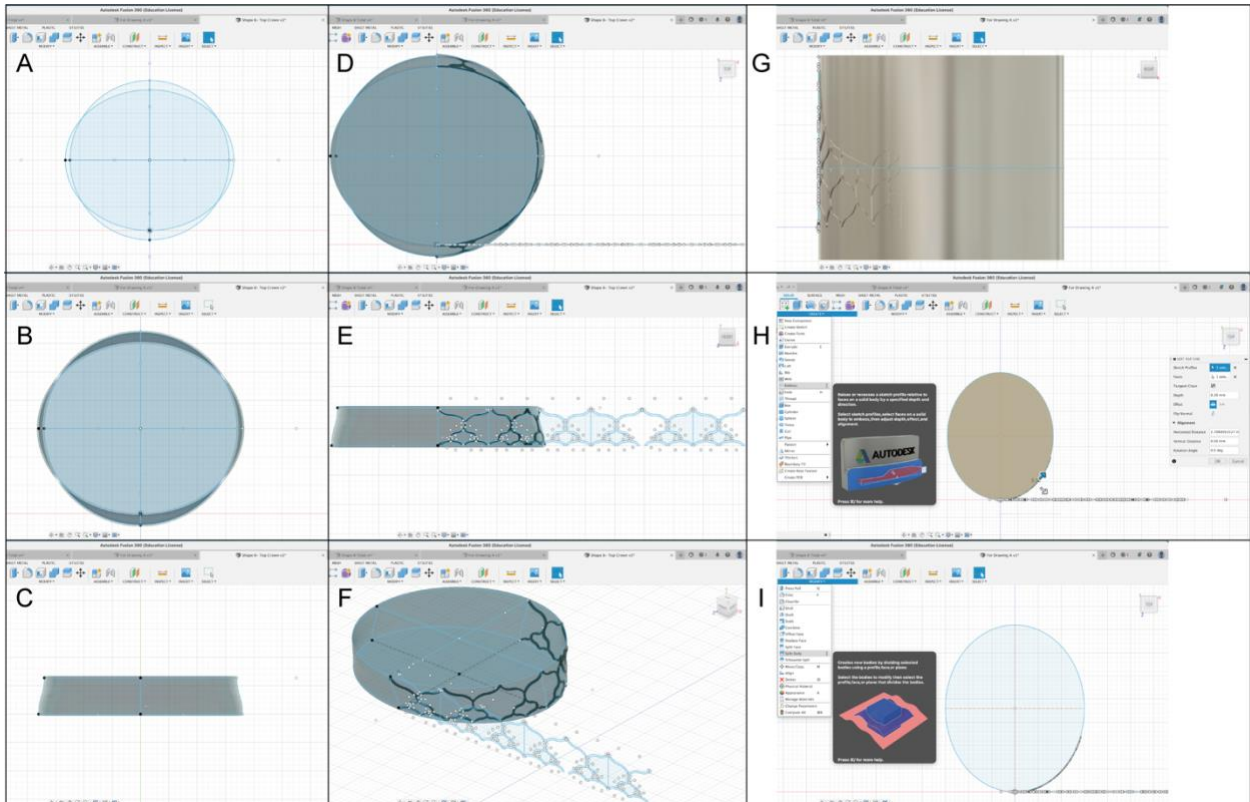


**Figure 17. Representative illustration of stent design (DGS-12B) in Group 3. A:** 2D sketch for pulmonary artery crown embossing; **B-C**: Solid body as a template for pulmonary artery crown embossing by lofting the 2D sketch; **D-F**: Pulmonary artery crown of stent embossing to the solid body (Top, front, and main views); **G-I**: RVOT crown of stent embossing to the elliptic solid body (Right and top views, **H** with the elliptic solid body, **I** without the elliptic solid body). RVOT- right ventricular outflow tract.

**Segment I:** The distal segment (Φ34 mm) at the top crown was designed with a circular architecture according to the PA anatomy. Meanwhile, the proximal segment of the top corollaceous crown was oval (30 mm: 36 mm) with a ratio of 1:1.2. The circular segment

was gradually transitioned to ovality. Accordingly, the top crown with 12 stabilized cells provided better coaxial alignment, which is beneficial for anchoring at the MPA. Three struts of the 12 X-shaped open cells were firmly connected with the two commissural horizontal suture lines to maintain the strength of the stent.

**Segment II:** This segment was composed of two functional parts: Two suture lines with 2.4 mm height at the commissural horizontal for heart valve fixation and three outstretched arms to guard the leaflets and compress the native leaflets. The two suture lines provided adequate space for surgeons to suture the heart valve at the commissural horizontal with running or interrupted sutures using 5-0 polypropylene.

**Segment III:** This segment was for the new APV and comprised two functional segments: Asymmetrical support frames with approximate determinate suture points and three guard arches for the basal segment of the leaflets. Each leaflet frame had 17 sewing points at approximately equal distances, from 2.7 mm to 3.1 mm, providing the surgeon with determinate suture points during the surgery for running or interrupted sutures. The three guard arches had four functions: 1. to protect the basal segment of the heart valve from blood flow, 2. to compress the native heart valve to supply the new heart valve with enough space, 3. to prevent the stented heart valve from migrating towards the pulmonary artery as well as to the RVOT, 4. at the second suture point connections between the two leaflet junctions below the three commissures, which can be used as a hook-connect point with the delivery system to reposition the stented heart valve in case of stent malposition.

**Segment IV:** This segment was for RVOT anchoring and comprised two slick secure layers to help the stented APV adhere at the RVOT without interrupting cardiac conduction bundles and other cardiac structures at the RVOT.

Segments **II-IV** were designed with an oval geometry to embrace the RVOT anatomy gently and fully with a long- and short-axis ratio of 1:1.2.
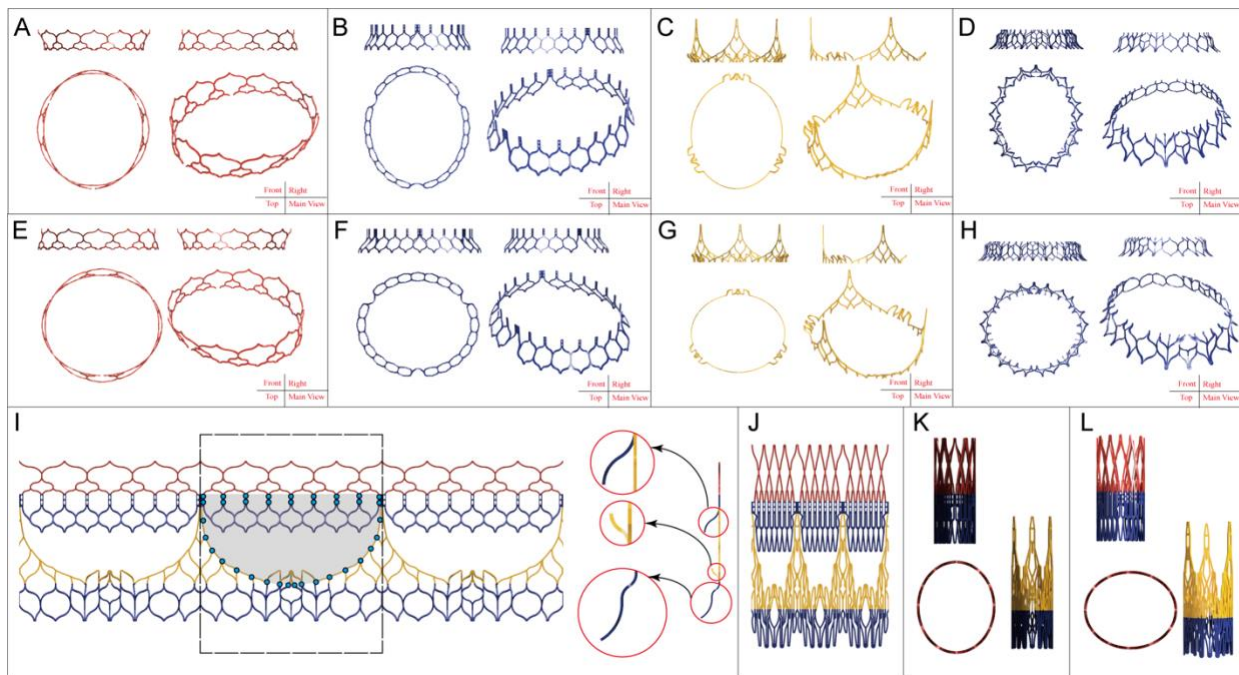
**Figure 18. The architectures of DGS-12A and DGS-12B. A-D: Architectures of DGS-12A, E-H: Architectures of DGS-12B, A and E:** Top crown for pulmonary artery with a circular geometry; **B and F:** Circular middle crown for the two suture lines at the commissural horizontal and native heart valve compression; **C and G:** Segment III for sewing the new heart valve with three guard arches at the basal part with a circular shape; **D and H:** Crown for RVOT anchoring; **I:** Expanded 2D sketch illustration with a virtual heart valve; **blue dots** are the suture points at the APV edges to the stent, the **black arrows** show the outstretched arms at segments II and III, two guard layers for RVOT anchoring; **J:** Crimped 2D illustration; **K:** Crimped 3D illustration of DGS-12A; **L:** Crimped 3D illustration of DGS-12B. Owing to the asymmetrical nature of the ovality, there were two designs of the three commissural attachments to the stents; therefore, the difference between DGS-12A and DGS-12B was the position of one of the commissures sutured into the stent at the long axis or the short axis of the ovality, which is shown in **A** to **C** and **E** to **F**.

### 2.2.3 Exporting the files of functional stents

After acquiring the 3D model of the stent, all solid bodies can be exported into different file formats: STL for 3D printing, SAT and IGS for ANSYS simulation.

After creating the 3D models, the software's rendering function rendered the stents with different colors and materials. The thus rendered stents were then exported as JPG files. The drawings of the stents were obtained from the "Drawing" function in Fusion 360 alongside the measurements at different functional parts of the various stents. All drawings were subsequently exported as PDF files.

### 2.3. Right ventricle + pulmonary artery blood flow simulation

Simulating the steady state of blood flow was performed using Ansys 2021 R2 Fluent with the pressure and velocity (0.6-0.9 m/s) based coupled solver, which had one velocity inlet (tricuspid valve level) and three velocity outlets (pulmonary artery branches) as boundary conditions. Blood was modeled as a non-Newtonian fluid using the Carreau-Yasuda model (69, 70) **(equation 4)**, and the following steps were used for the simulation:

$$\mu_{eff} = \mu_\infty + (\mu_0 - \mu_\infty)[1 + (\lambda * \gamma)^2]^{\frac{(n-1)}{2}} \qquad (4)$$

Here, **$\mu_{eff}$** is the effective viscosity and **$\mu_0$, $\mu_\infty$, $\lambda$** and **n** are material coefficients. The representative valves for human blood are: $\mu_0$=0.056 kg/ms, $\mu_\infty$=0.0035 kg/ms, $\lambda$=3.313 s, n=0.3568.

### 2.3.1 Read mesh

❖ **Model importing and meshing:**

The RVOT+PA model was imported into Ansys Fluent, after which the mesh was read in a new 3D session of Ansys. The imported mesh is checked using [Perform Mesh Check] and the mesh quality is evaluated using [Evaluate Mesh quality]. A mesh orthogonal quality greater than the recommended minimum threshold of 0.1 confirms that the mesh is of good quality, **Figure 19**.
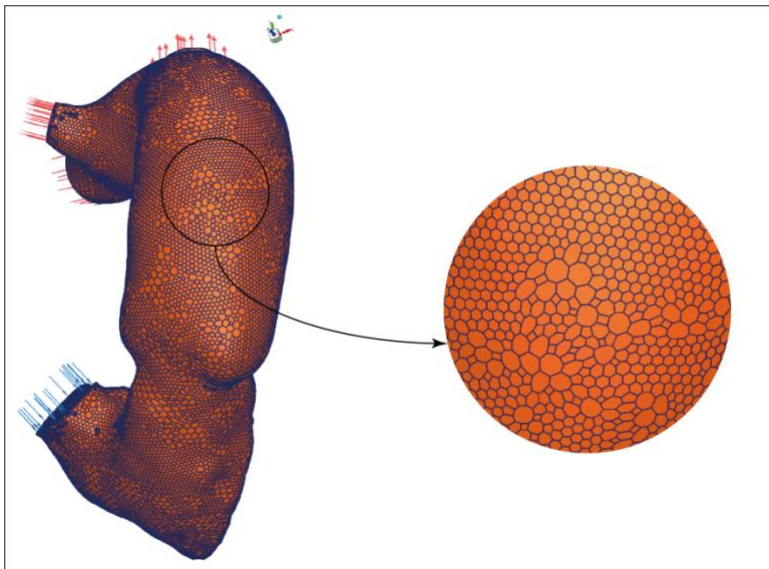


**Figure 19. Mesh for blood flow simulation in Ansys.**
Blue arrows show the inlet flow direction of the right-heart 3D model at the tricuspid valve level, red arrows show the outlet flow directions of the three branches of main pulmonary artery, black arrow shows the meshing elements in detail.

❖ **Physics setup**

[Pressure-Based] was kept as the [Solver] type and [Steady] under [Time], while default [Operating conditions] were also kept as default. [Laminar] was selected under [Model] since the Reynolds number for this problem was low, after which the material properties and boundary conditions were set up. The type was changed to [velocity-inlet (0.6-0.9 m/s)] and [pressure-outlet] was repeated three times.

❖ **Material property setup**

[Create/Edit] was selected under [Materials] (71), [Material Name] was changed to "Blood" and [Density (kg/m$^3$)] to 1060, [Carreau] was selected in the drop-down list for [Viscosity (kg/m-s)], and the [Carreau Model] was set as follows: [Time Constant, lambda (s)]=3.31, [Power-Law index, n]=0.3568, [Zero Shear Viscosity (kg/m-s)]=0.056, [Infinite

Shear Viscosity (kg/m-s)]=0.0035; [Cell Zones] was selected to edit the [Cell Zone Conditions] to ensure that the [Material Name] was set to [blood].

❖ **Boundary conditions setup**

Under [Zones], [Boundaries] was selected to set up boundary conditions. It was verified that [Wall] was selected as [Type]→ [Wall], and that the [Wall Motion] was set to [Stationary Wall]. In the list of [Boundary Conditions], {inlet} was selected and its [Type] changed to [velocity-inlet]. Under the [Momentum] tab, 0.9 was entered as [Velocity magnitude (m/s)]. In the list of [Boundary Conditions], [Outlet01] was selected and its [Type] changed to [velocity-outlet]. Under the [Momentum] tab, 13332 was entered as [Gauge Pressure (m/s)]. As the three outlets had the same boundary conditions, the "copy boundary condition" feature was applied to speed up the process.

❖ **Numerical solution**

The default settings were maintained under the [Solution] tab, and [Pseudo Transient] was checked while keeping the default values for [Pseudo Transient Explicit Relaxation Factors] under [Solution Controls]. The [Absolute Criteria] was kept as the default valve in [Residual Monitors]. Meanwhile, a monitor for mass flux imbalance was set up in the [Report] column by clicking [Definitions]→ [New]→ [Flux Report] → [Mass Flow Rate], selecting the inlet and all outlets, and checking the [Report Plot] option to plot the flux value during calculation. The [Solution] was then initialized and computed. Once "Hybrid initialization is done" appeared, the initial case and data were saved. "200" was entered for [Number of Iterations] in the [Run Calculation] tab, and the calculation was started by clicking [Calculate].

❖ **Results of blood flow simulation**

[Mass Flow Rate] was selected in [Options], followed by the inlet and all outlets in the [Boundaries] column to check the conservation of mass in more detail by clicking [Compute]. [Contours] was selected to add a [New] flow field for detailed post-processing and visualizing: [Pressure] and [Static Pressure] was selected under [Contours of], after which {wall} was selected and [Save/Display] was clicked. [Wall Fluxes] and [Wall Shear Stress] was selected under [Contours of], after which {wall} was selected and [Save/Display] was clicked. To visualize the flow field, [Pathlines] was selected to add a [New] flow field, the inlet was selected under [Release from Surfaces]. "1000" was entered for [Steps] and "2" for [Path Skip], following which [Velocity] and [Velocity Magnitude] were selected under [Color by]. Static blood flow was visualized by clicking

the [Save/Display] and [Pulse] tabs.

## 2.4. Right ventricle + pulmonary artery shear force simulation

The main parameters of the RVOT+PA 3D model were as follows:

Density: 7850 kg m^-3, Specific Heat: 2.3 E+006 mJ/kg•℃, Coefficient of Thermal: 2.3E-004/℃, Tensile Yield Strength: 25 MPa, Tensile Ultimate Strength: 33 MPa, and Zero-Thermal-Strain Reference Temperature: 22 ℃, Young's Modulus: 0.5 MPa, Poisson's Ratio: 0.45, Bulk Modulus: 1.6667 MPa, Shear Modulus: 0.17241 MPa.

### 2.4.1　Geometry setup

❖ [Definition] settings: [Flexible] was selected under [Stiffness Behavior], [Default Coordinate System] under [Coordinate System], and [No] under [Suppressed]. [Material]: [Blood] was selected under [Assignment], and [Nonlinear Effects] and [Thermal Strain Effects] were applied.

❖ [Basic Geometry Options] settings: [Yes] was selected under [Solid Bodies], [Surface Bodies], [Line Bodies], [Attributes], [Named Selections] and [Material Properties]. [Independent] was selected under [Parameters].

❖ [Advanced Geometry Options] settings: [Yes] was selected under [Use Associativity], [Import Coordinate Systems], [Import Using Instances], [Smart CAD Update], [Decompose Disjoint Geometry], and [Enclosure and Symmetry Processing]. [Independent] was selected under [Parameters]. [No] was selected under [Reader Mode Saves Updated File], [Compare Parts On Update], [Clean Bodies On Import], and [Stitch Surfaces On Import].

### 2.4.2　Coordinate system setup

[Global Coordinate System] was selected under [Coordinate System], [Cartesian] under [Type].

### 2.4.3　Contacts of RVOT+PA 3D model setup

❖ [Scope] settings: [Geometry Selection] was selected under [Scoping Method].

❖ [Auto Detection] settings: [Slider] was selected under [Tolerance Type], "0" under [Tolerance Slider], "0.41074 mm" under [Tolerance Value], [No] under [Use Range], [Yes] under [Face/Face], "75º" under [Face-Face Angle Tolerance], [Off] under [Face Overlap Tolerance], [Include] under [Cylindrical Faces], [No] under [Face/Edge] and [Edge/Edge], and [Bodies] under [Group By] and [Search Across].

### 2.4.4    Contact regions setup

❖    [Scope] settings: [Geometry Selection] was selected under [Scoping Method], [15831 Faces] under [Target], [Volume\Volume] under [Contact Bodies], [Geom\Solid22] under [Target Bodies].

❖    [Definition] settings: [Bonded] was selected under [Type], [Automatic] under [Scope Mode], [Program Controlled] under [Behavior] and [Trim Contact], and "0.41074 mm" under [Tolerance Value].

❖    [Advanced] settings: [Program Controlled] was selected under [Formulation], [Small Sliding], [Detection Method], [Penetration Tolerance], [Elastic Slip Tolerance], [Normal Stiffness], [Update Stiffness], and [Pinball Region].

❖    [Geometric Modification] settings: [None] was selected under [Contact Geometry Correction] and [Target Geometry Correction].

### 2.4.5    Meshing setup

❖    [Display] settings: [Use Geometry Setting] was selected under [Display Style].

❖    [Defaults] settings: [Mechanical] was selected under [Physics Preference], [Program Controlled] under [Element Order], and [Default] under [Element Size].

❖    [Sizing] settings: [Yes] was selected under [Use Adaptive Sizing] and [Mesh Defeaturing], [Default] under [Resolution] and [Defeature Size], [Fast] under [Transition], [Coarse] under [Span Angle Center], and [Assembly] under [Initial Size Seed].

❖    [Quality] settings: The meshing quality was controlled by [Aggressive Mechanical] error limits, [Default (0.050000)] target quality, and [Medium] smoothing method. The element size of meshing for the stent was 0.05 mm, which was used to confirm the appropriate meshing or proper geometry for the subsequent deformation.

❖    [Advanced] settings: [No] was selected under [Generate Pinch on Refresh] and [Straight Sided Elements], [Yes] under [Topology Checking], [Program Controlled] under [Number of CPUs for Parallel Part Meshing] and [Triangle Surface Mesher], and [Dimensionally Reduced] under [Rigid Body Behavior].

### 2.4.6    Analysis settings:

❖    [Analysis Definition] settings: [Structural] was selected under [Physics Type], [Static Structural] under [Analysis Type], and [Mechanical APDL] under [Solver target].

❖    [Step Controls] settings: "1" was selected as the [Number of Steps], [Program Controlled] under the [Auto Time Stepping].

❖    [Solver Controls] settings: [Program Controlled] was selected under [Solver Type] and [Solver Pivot Checking], [Off] under [Weak Springs], [Large Deflection], [Inertia Relief],

and [Quasi-Static Solution].

❖ [Rotordynamics Controls] settings: [Off] was selected under [Coriolis Effect].

❖ [Restart Controls] settings: [Program Controlled] was selected under [Generate Restart Points] and [Combine Restart Files], and [No] under [Retain Files After Full Solve].

❖ [Nonlinear Controls] settings: [Program Controlled] was selected under [Newton-Raphson Option], [Force Convergence], [Moment Convergence], [Displacement Convergence], [Rotation Convergence], [Line Search], and [Stabilization].

❖ [Nonlinear Controls] settings: [No] was selected under [Inverse Option], [Off] under [Contact Split (DMP)].

❖ [Output Controls] settings: [Yes] was selected under [Stress], [Strain], [Contact Data], [Volume and Energy] and [Euler Control]. [No] was selected under [Surface Stress], [Back Stress], [Nonlinear Data], [Nodal Faces], [General Miscellaneous] and [Contact Miscellaneous]. [Program Controlled] was selected under [Result File Compression].

❖ [Analysis Data Management] settings: [Program Controlled] was selected under [Contact Summary], [No] under [Save MAPDL db] and [Nonlinear Solution], [Active System] under [Solver Units], and [nmm] under [Solver Unit System].

### 2.4.7 Loads settings

❖ [Scope] settings: [Geometry Selection] was selected under [Scoping Method], and [No] under [Suppressed].

❖ [Definition] settings: [Fixed Support] was selected under [Type] and [4 Faces] under [Geometry].

### 2.4.8 Imported Load settings

❖ [Definition] settings: [Imported Data] was selected under [Mechanical-Based Mapping], [4 Faces] under [Geometry], [No] under [Suppressed], and [B5: Solution] under [Source].

❖ [Definition] settings: [Yes] was selected under [Delete Mapped Data Files].

### 2.4.9 Imported Load settings

❖ [Scope] settings: [Named Selection] was selected under [Scoping Method] and [inner wall] under [Named Selection].

❖ [Definition] settings: [Imported Pressure] was selected under [Type], [Initial] under [Loaded Area], [Program Controlled] under [Tabular Loading], [No] under [Suppressed], and [Worksheet] under [Source Time].

❖ [Transfer Definition] settings: [wall] was selected under [CFD Surface].

❖ [Settings] options: [Program Controlled] was selected under [Mapping Control],

[Profile Preserving] under [Mapping], [Triangulation] under [Weighting], and [Surface] under [Transfer Type].

❖ [Graphics Controls] settings: [Off] was selected under [Display Source Points].

❖ [Graphics Controls] settings: [Program Controlled] was selected under [Legend Range], [Minimum Source], [Maximum Source].

### 2.4.10 Adding [Solution] to obtain results

❖ [Solution Information] settings: [Force Convergence] was selected under [Solution Output], [0] under [Newton-Raphson Residuals] and [Identify Element Violations], and [2.5 s] under [Update Interval].

❖ [FE Connection Visibility] settings: [All FE Connectors] was selected under [Display], [Single] under [Line Thickness] and [Lines], and [2.5 s] under [Display Type].

### 2.5. DGS stent simulation for stent life and radial force

The SAT files of the DGS stents were exported from Autodesk Fusion 360 and then imported into the Ansys 2021 R2 Workbench to build the "Ansys library for each stent simulation". The Static Structural module was chosen to build the stent simulation folder, which included the Engineering Data, Geometry, Model, Setup, Solution, and Results. All data that were set up for each procedure were as follows:

### 2.5.1 Engineering Data
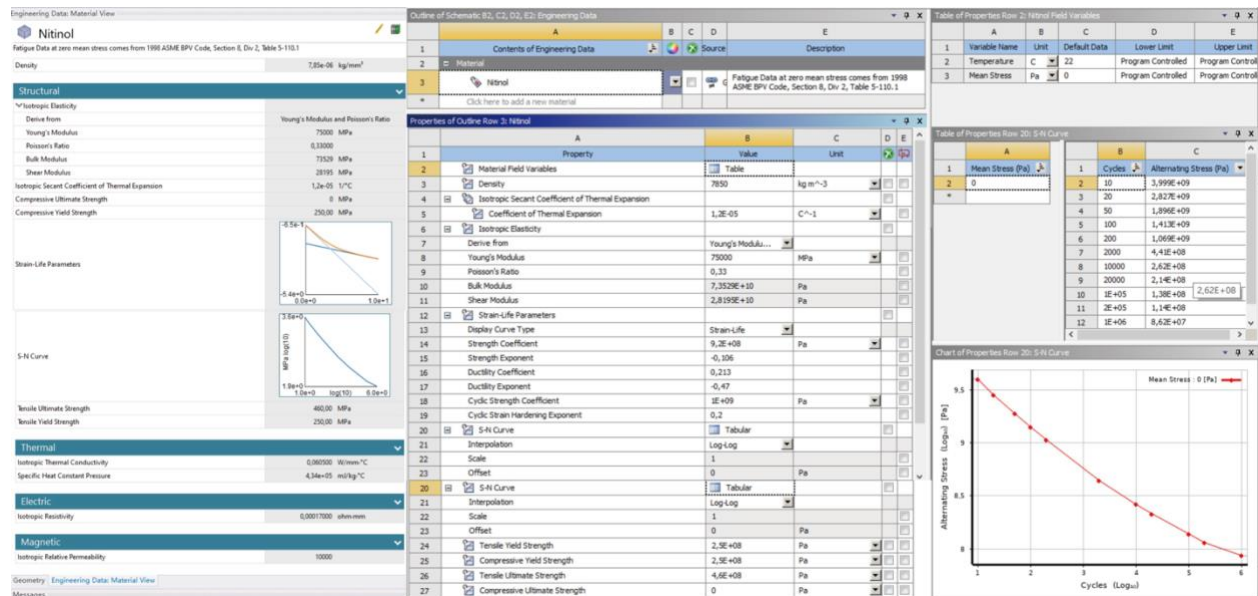


**Figure 20. Nitinol properties for self-expandable stent.** The American Society of Mechanical Engineers: https://www.asme.org/codes-standards/find-codes-standards/bpvc-viii-2-bpvc-section-viii-rules-construction-pressure-vessels-division-2-alternative-rules?productKey=900082:900082.

Shape memory material (nitinol) was used as the material for the stents. The main parameters are as follows: Isotropic Elasticity (Density: 7850 kg m^-3, Young's Modulus: 75000 MPa, Poisson's Ratio: 0.33, Bulk Modulus: 7,3529E+10 Pa, Shear Modulus:

2.8195E+10 Pa, Compressive Yield Strength: 250,000 MPa), Thermal (Isotropic Thermal Conductivity: 0.060500 W/mm•℃, Specific Heat Constant Pressure, 4.34E+05 mJ/kg•℃), Strain-Life Parameters (Strength Coefficient: 9.2E+08 Pa, Strength Exponent: -0.106, Ductility Coefficient: 0.213m, Ductility Exponent: -0.47, Cyclic Strength Coefficient: 1E+09 Pa, Cyclic Strain Harding Exponent: 0.2); see **Figure 20**.

**Geometry setup:** The SAT files of the stents were imported into the SpaceClaim module to repair the 3D geometries by detecting faults in the stents, which were thereafter imported into the design modeler.

❖ Definition] settings: [Flexible] was selected under [Stiffness Behavior], [Default Coordinate System] under [Coordinate System], and [No] under [Suppressed]. [Material]: [Nitinol] was selected under [Assignment], and [Nonlinear Effects] and [Thermal Strain Effects] were applied.

❖ [Basic Geometry Options] settings: [Yes] was selected under [Solid Bodies], [Surface Bodies], [Line Bodies], [Attributes], [Named Selections] and [Material Properties]. [Independent] was selected under [Parameters].

❖ [Advanced Geometry Options] settings: [Yes] was selected under [Use Associativity], [Coordinate System], [Use Instances], [Smart CAD Updates], [Decompose Disjoint Geometry] and [Enclosure and Symmetry Processing]. [Independent] was selected under [Parameters]. [No] was selected under [Reader Mode Saves Updated File], [Compare Parts On Update], [Clean Bodies On Import], and [Stitch Surfaces On Import].

### 2.5.2 Coordinate system setup

[Global Coordinate System] was selected under [Coordinate System], [Cylindrical] and [Cartesian] under [Type], [Program Controlled] under [Coordinate System], and [Absolute] under [Base Configuration].

### 2.5.3 Meshing setup

[Use Geometry Setting] was selected under [Display Style], [Mechanical] under [Physics Preference], [Program Controlled] under [Element Order], and [Default] under [Element Size] and [Defeature].

The meshing quality was controlled by [Standard Mechanical] error limits, [Default] target quality, [Element Quality] mesh metric and [Medium] smoothing method. The element size of meshing for the stent was 0.05 mm or by default according to each stent design, which was then used to confirm each grid of the stent as having three element layers for appropriate meshing or the proper geometry for the subsequent deformation.

Advanced settings were controlled by [Dimensionally Reduced] under [Rigid Body Behavior] and [Program Controlled] under [Triangle Surface Mesher].

### 2.5.4 Boundary conditions

To setup the boundary conditions, a coordinate system was initially created at the center of the stent. The conditions were modified to fit the stent's geometry.

### 2.5.5 Analysis settings

❖ [Analysis Definition] settings: [Structural] was selected under [Physics Type], [Static Structural] under [Analysis Type], and [Mechanical APDL] under [Solver Target].

❖ [Step Controls] settings: "1" was selected as the [Number Of Steps], [Program Controlled] under the [Auto Time Stepping].

❖ [Solver Controls] settings: [Program Controlled] was selected under [Solver Type] and [Solver Pivot Checking], [Off] under [Weak Springs], [Large Deflection], [Inertia Relief], and [Quasi-Static Solution].

❖ [Rotordynamics Controls] settings: [Off] was selected under [Coriolis Effect].

❖ [Restart Controls] settings: [Program Controlled] was selected under [Generate Restart Points] and [Combine Restart Files], and [No] under [Retain Files After Full Solve].

❖ [Nonlinear Controls] settings: [Program Controlled] was selected under [Newton-Raphson Option], [Force Convergence], [Moment Convergence], [Displacement Convergence], [Rotation Convergence], [Line Search], and [Stabilization].

❖ [Output Controls] settings: [Yes] was selected under [Stress], [Strain], [Contact Data], [Volume and Energy] and [Euler Control]. [No] was selected under [Surface Stress], [Back Stress], [Nonlinear Data], [Nodal Faces], [General Miscellaneous] and [Contact Miscellaneous]. [Program Controlled] was selected under [Result File Compression].

### 2.5.6 Adding displacement

Parameters for total deformation and directional deformation were set according to the crimped and expandable heights and diameters of each stent.

### 2.5.7 Adding [Life] order and [Equivalent stress] order

[Zero-Based] was selected under [Loading Type], [Stress Life] under [Analysis Type], [Equivalent (von-Mises)] under [Stress Component], and [No] under [Suppressed].

### 2.5.8 Adding [Solution] to obtain results

[Definition] settings: [Force Reaction] was selected under [Type], [Boundary Condition] under [Location Method], and [Displacement] under [Boundary Condition].

## 2.6. Stents+ RVOT+PA simulation for the DGS stents' hoop force

The SAT files of the stents and RVOT+PA 3D model were imported into the SpaceClaim module to repair the 3D geometries after detecting faults in the stents, which were then imported into the design modeler. To save computer costs, the RVOT+PA 3D model was modified with a low profile (pulmonary valve area and pulmonary artery trunk). The modified RVOT+PA was then imported into the Design Modeler. After importing the stents and RVOT+PA, contacts were added between the stents and the RVOT+PA using the "Slider" tolerance type. The target contact face was the inner surface of the RVOT+PA. Methods for the stent material and other computational settings were the same as above. Load, total deformation, directional deformation, and force reaction were added to the models as follows to obtain the corresponding results.

### 2.6.1  RVOT+PA 3D model properties setup

The main parameters of the RVOT+PA 3D model were set up as illustrated in section 2.5.

### 2.6.2  Geometry setup

❖  [Basic Geometry Options] settings: [Yes] was selected under [Solid Bodies], [Surface Bodies], [Line Bodies], [Attributes], [Named Selection] and [Material Properties]. [Independent] was selected under [Parameters].

❖  [Advanced Geometry Options] settings: [Yes] was selected under [Use Associativity], [Coordinate System], [Use Instances], [Smart CAD Updates], [Decompose Disjoint Geometry], and [Enclosure and Symmetry Processing]. [Independent] was selected under [Parameters]. [No] was selected under [Reader Mode Saves Updated File], [Compare Parts On Update], [Clean Bodies On Import], and [Stitch Surfaces On Import].

### 2.6.3  Coordinate system setup

❖  [Global Coordinate System] was selected under [Coordinate System], [Cylindrical] and [Cartesian] under [Type], [Program Controlled] under [Coordinate System], and [Absolute] under [Base Configuration].

❖  [Global Coordinates] was selected to define the [Origin], and [Fixed Vector] to define the [Orientation About Principal Axis].

### 2.6.4  Connection of the RVOT+PA model and the DGS stents' setup

❖  [Scope] settings: [Geometry Selection] was selected under [Scoping Method], [1 Face] under [Contact], [1 Face] under [Target], and [Stents] under [Contact Bodies], [RVOT+PA 3D Model] under [Target Bodies], [Bottom] under [Target Shell Face], and [No] under [Shell Thickness Effect] and [Protected].

❖  [Definition] settings: [Frictionless] was selected under [Type], [1 Face] under

[Contact], [Manual] under [Scope Mode], and [Program Controlled] under [Behavior] and [Trim Contact].

❖ [Advanced] settings: [Program Controlled] was selected under [Formulation], [Small Sliding], [Detection Mode], [Penetration Tolerance], [Normal Stiffness], [Update Stiffness], and [Pinball Region].

❖ [Geometric Modification] settings: [Add Offset, No Ramping] was selected under [Interface Treatment], [None] under [Contact Geometry Correction] and [Target Geometry Correction], and [0 mm] under [Offset].

### 2.6.5 Meshing setup

[Use Geometry Setting] was selected under [Display Style], [Mechanical] under [Physics Preference], [Program Controlled] under [Element Order], and [Default] under [Element Size] and [Defeature].

The meshing quality was controlled by [Standard Mechanical] error limits, [Default] target quality, [Element Quality] mesh metric and [Medium] smoothing method.

### 2.6.6 Analysis settings

❖ [Analysis Definition] settings: [Structural] was selected under [Physics Type], [Static Structural] under [Analysis Type], and [Mechanical APDL] under [Solver Target].

❖ [Step Controls] settings: "1" was selected as [Number Of Steps], and [Program Controlled] under the [Auto Time Stepping].

❖ [Solver Controls] settings: [Program Controlled] was selected under [Solver Type] and [Solver Pivot Checking], [Off] under [Weak Springs], [Large Deflection], [Inertia Relief], and [Quasi-Static Solution].

❖ [Rotordynamics Controls] settings: [Off] was selected under [Coriolis Effect].

❖ [Restart Controls] settings: [Program Controlled] was selected under [Generate Restart Points] and [Combine Restart Files], and [No] under [Retain Files After Full Solve].

❖ [Nonlinear Controls] settings: [Program Controlled] was selected under [Newton-Raphson Option], [Force Convergence], [Moment Convergence], [Displacement Convergence], [Rotation Convergence], [Line Search], and [Stabilization].

❖ [Output Controls] settings: [Yes] was selected under [Stress], [Strain], [Contact Data], [Volume and Energy] and [Euler Control]. [No] was selected under [Surface Stress], [Back Stress], [Nonlinear Data], [Nodal Faces], [General Miscellaneous] and [Contact Miscellaneous]. [Program Controlled] was selected under [Result File Compression].

❖ [Analysis Data Management] settings: [Yes] was selected under [Deleted Unneeded Files] and [Nonlinear Solution], [Program Controlled] under [Contact Summary].

❖ Adding [Solution] to obtain results

❖ [Solution Information] settings: [Force Convergence] was selected under [Solution Output], [0] under [Newton-Raphson Residuals] and [Identify Element Violations], and [2.5 s] under [Update Interval].

❖ [FE Connection Visibility] settings: [All FE Connectors] was selected under [Display], [Single] under [Line Thickness] and [Lines], and [2.5 s] under [Display Type].

# 3. Results

## 3.1. Animal cardiac CT and 3D cardiac CT reconstructions in 3D Slicer

All of the sheep in this study successfully underwent a cardiac CT examination one week prior to transcatheter autologous pulmonary valve implantation. Animal J Pre-CT was chosen to be imported into 3D Slicer, from which all segments of the heart were generated in 3D, as shown in **Figure 21**, **Figure 22**, and **Error! Reference source not found.**.
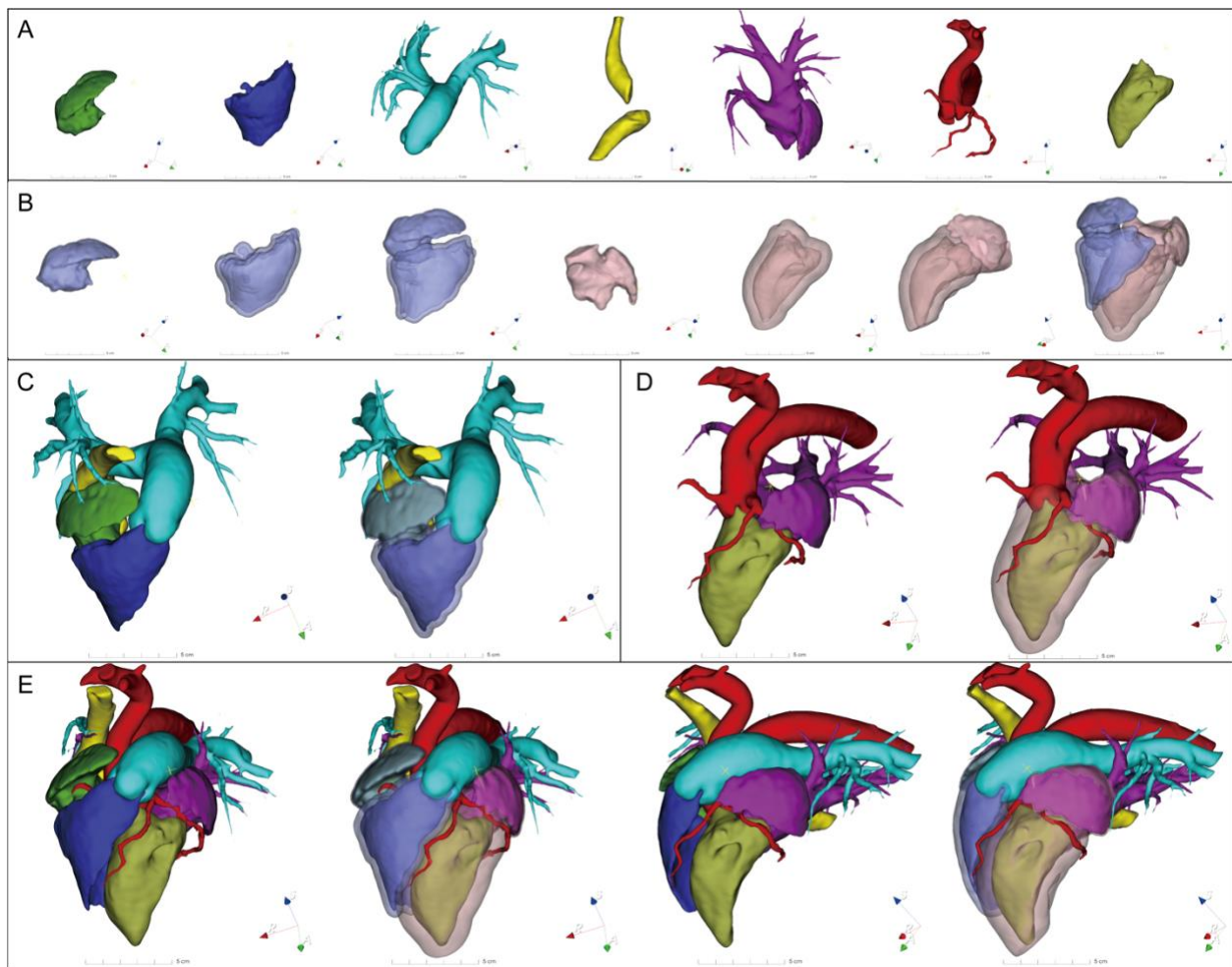


**Figure 21. Sheep J Pre-CT 3D reconstruction in 3D Slicer**
**A:** From left to right: right atrium, right ventricle, pulmonary artery, superior vena cava (SVC) + inferior vena cava (IVC), left atrium + pulmonary vein, aorta + coronary arteries, left ventricle, **B**: Right and left heart myocardium following the sequence of A, **C:** Right heart without/with myocardium, **D**: Left heart without/with myocardium, **E:** Total heart reconstruction with/without myocardium.
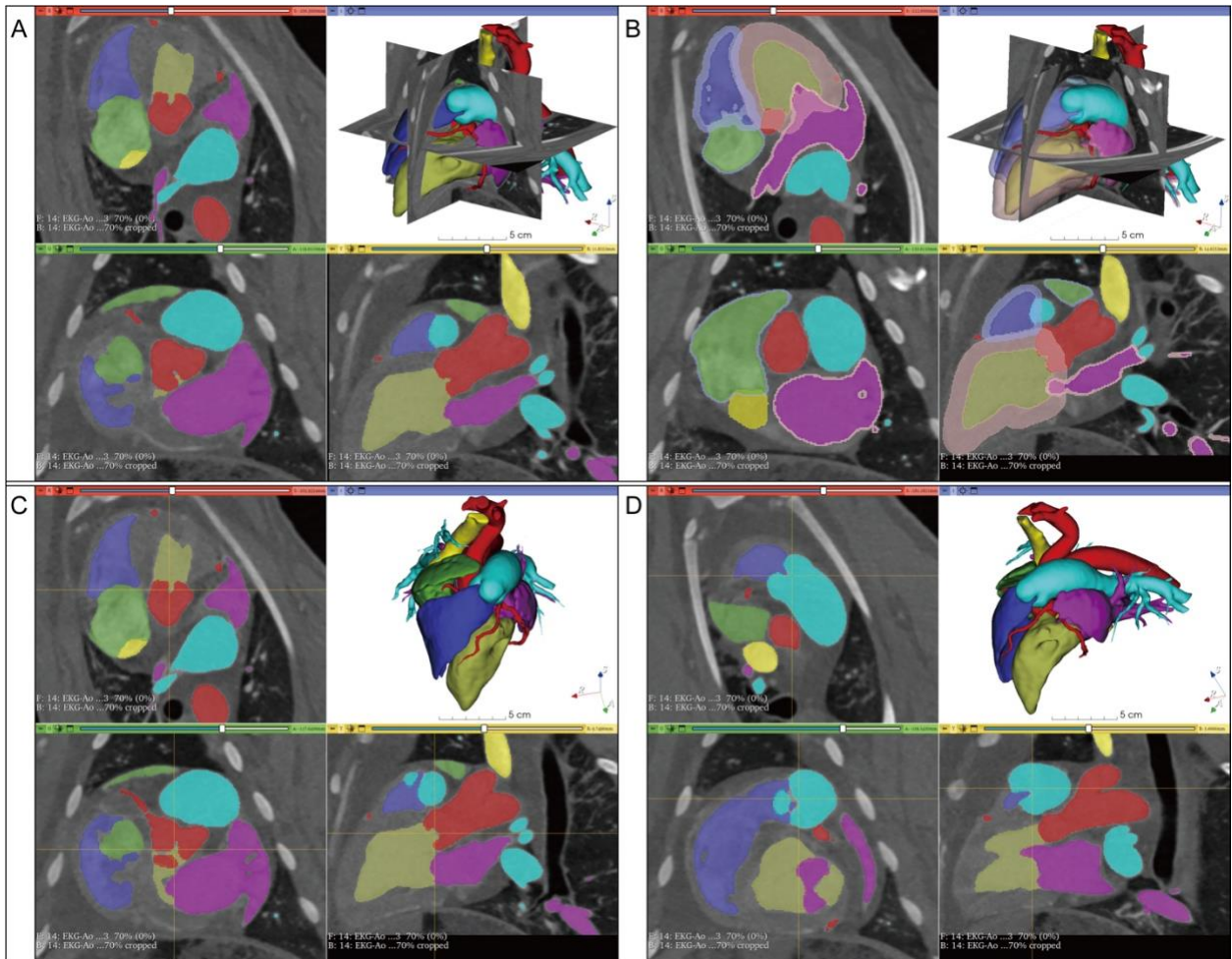
**Figure 22. Sheep J Pre-CT with 3D reconstruction in 3D Slicer**
**A**: Blood pool reconstruction of the heart with CT images, **B**: Blood pool and myocardium reconstruction of the heart with CT images, **C**: Blood pool reconstruction of the heart with the crosshair at the aortic valve position, **D**: Blood pool reconstruction of the heart with the crosshair at th9e pulmonary valve position
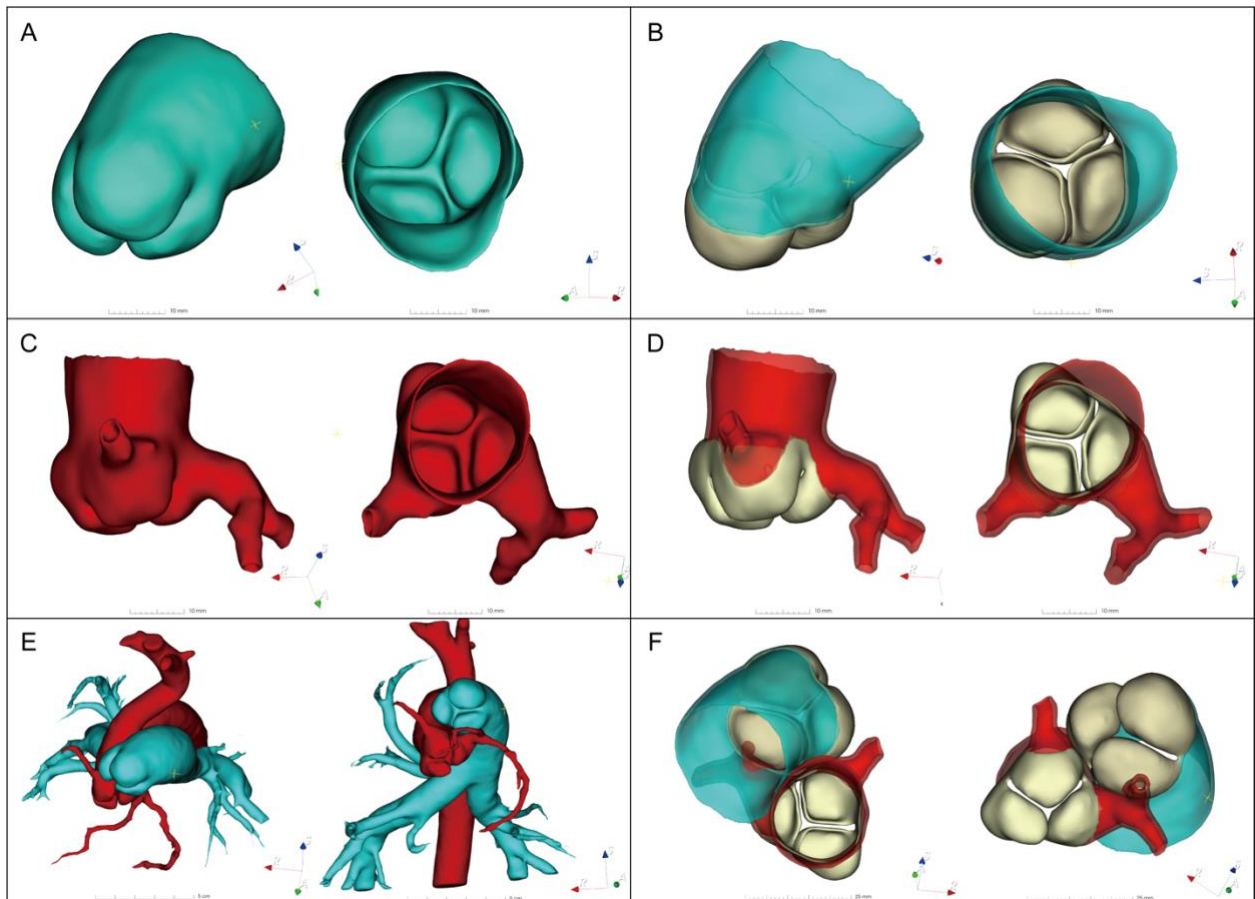
**Figure 23. 3D reconstructions of pulmonary valve, aortic valve, aorta, pulmonary artery, and their relationships**

**A:** Pulmonary root, **B:** Pulmonary valve and main pulmonary artery, **C:** Aortic root, **D**: Aortic valve and ascending aorta, **E:** Relationship between aorta and pulmonary artery, **F:** Relationship between aortic valve and pulmonary valve.

## 3.2. Functional stent designs in Fusion 360 (Educational Version)

Twelve functional stents were designed using various methodologies in Fusion 360.

### 3.2.1   Group 1

❖ **DGS-3**

In this study, DGS-3 was designed to be 30 mm in diameter and 40.4 mm in height to mount a 30-mm diameter new heart valve with a Nitinol shape-memory self-expandable frame. Based on its design, it can be used in patients following TOF surgery with patched RVOT or a narrowed RVOT. The design concept of DGS-3 was divided into three functional segments: 1. A top crown with V-shaped struts for PA anchoring, 2. new leaflet loading zones with two specific suture lines at the commissural horizontal and fixation points for the edges of the new leaflets, and 3. a bottom crown for RVOT anchoring. DGS-3 can be fully crimped to 10.3 mm in diameter and 44.4 mm in height using a crimping tool for deployment at the pulmonary valve position, **Figure 24**.
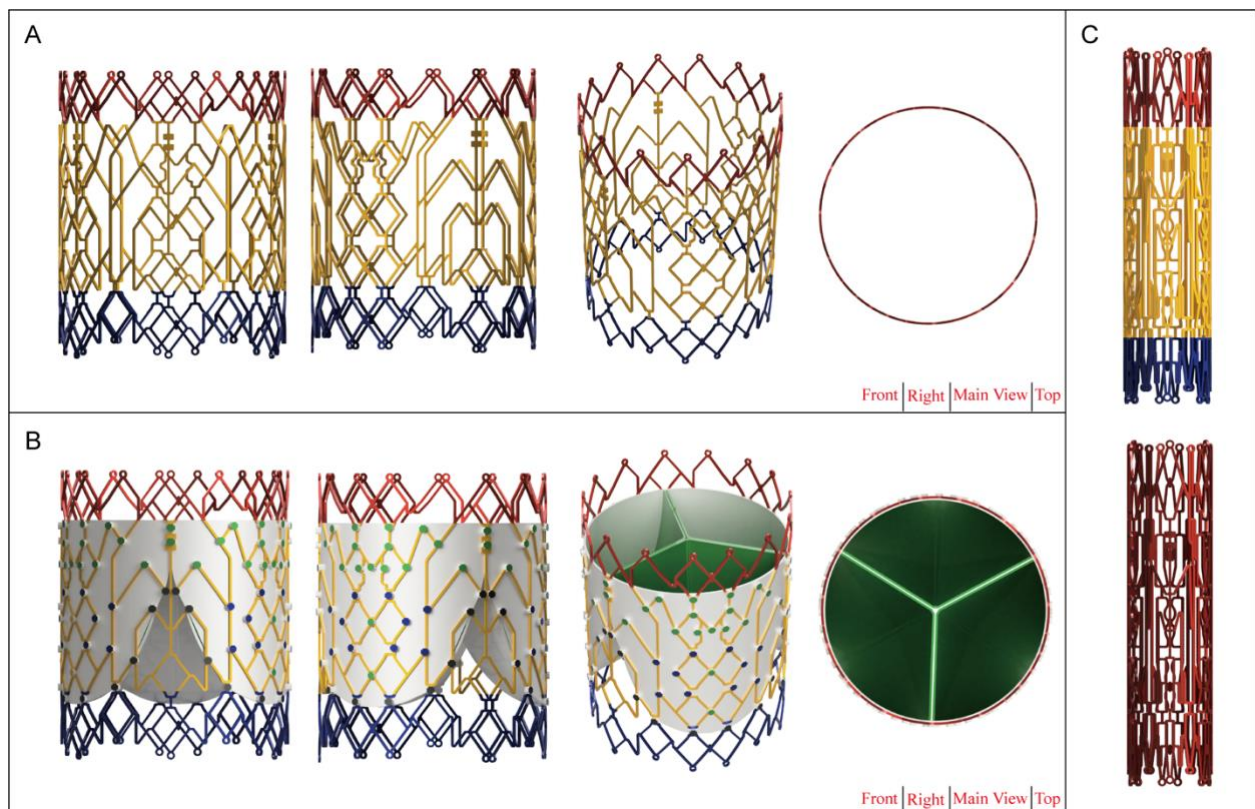


**Figure 24. DGS-3 illustration**
**A:** Illustration of total DGS-3 stent from four directions; **B:** Illustration of DGS-3 with a virtually sutured autologous pulmonary valve; **C:** Illustration of fully crimped DGS-3.

**Segment I:** This segment of DGS-3 was given a V-shaped frame to help the new stented heart valve anchor at the main pulmonary artery. It has six connective zones to link to segment II for each new leaflet to maintain a stable radial force and hoop force following deployment. It has the same diameter as the main zone, which is responsible for hosting the new heart valve (30 mm).

**Segment II:** The most significant component of the DGS-3 was segment II, featuring Y- and V-shaped struts that established two suture lines at the commissural horizontal and maintained the stent's integrity. Surgeons could use either running or interrupted sutures to secure the new heart valve to the stent and to tie surgical knots at the three commissures for a more secure fit. Another useful feature of segment II is that every leaflet edge has balanced support struts for future leaflet hosting, and each leaflet can be sutured at eleven specified suture sites aligned in the grids. There are also 17 potential suture locations to further fix each leaflet if the mounting requires tightening. Segment II was connected to the RVOT crown to maintain the stent's integrity for optimal radial and hoop force. The DGS-3 was designed to resemble the main entrance of the German Heart Center (DHZB). As a result, the sagittate frame at the three commissures was designed as a main support strut to host the new heart valve for better radial force and hoop force after deployment of the stented heart valve in the correct location. Regarding the integrity of the entire stent, the frame was asymmetrical in this section, with large open cells enclosing small, closed cells.

**Segment III**: With symmetrical struts connecting to segment II, segment III was designed for RVOT anchoring and contained six connective struts linked to segment II for each leaflet. The V-shaped struts at the bottom of the stent were not aligned in the same planes after deployment and when crimped.

❖ **DGS-5**

DGS-5 was designed as a Nitinol self-expandable stent to carry a tri-leaflet heart valve for transcatheter pulmonary valve implantation in patients with a patched RVOT or narrowed RVOT. In this study, DGS-5 was designed to be 30 mm in diameter and 35.8 mm in height for a 30-mm diameter new heart valve. It can be fully crimped to 7.6 mm in diameter and 41.2 mm in height using a crimping tool, which can be loaded in the 24Fr head of a delivery system for deployment; see **Figure 25**.
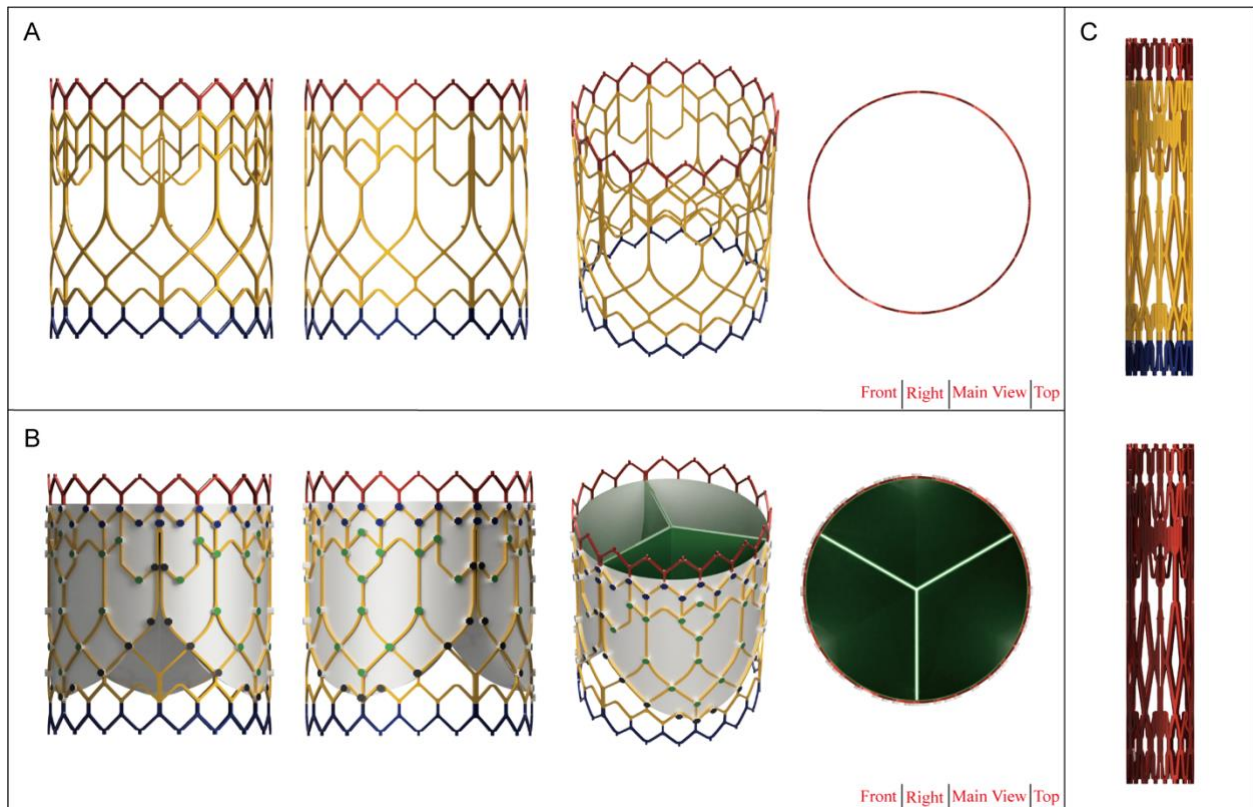


**Figure 25. DGS-5 illustration**
**A:** Illustration of total DGS-5 stent from four directions; **B:** Illustration of DGS-5 with a virtually sutured autologous pulmonary valve; **C:** Illustration of fully crimped DGS-5.

**Segment I:** The top crown was designed with 18 Y-shaped struts to help the stented heart valve anchor at the pulmonary artery trunk with balanced radial force and hoop force. The height of the top crown was only 4.3 mm, reducing the risk of damaging the pulmonary artery during stent deployment. Each strut was linked to segment II in order to maintain the integrity of the stent; three strong struts were designed to connect to the three commissures.

**Segment II:** Segment II was the most important feature of DGS-5, containing Y- and V-shaped struts to form two suture lines at the commissural horizontal and to maintain the integrity of the stent. Surgeons can use either running or interrupted sutures to fix the new heart valve onto the stent; surgical knots can also be placed at the three

commissures for tighter fixation. Another functional feature of segment II were four mellifluous support struts in every leaflet edge for hosting new leaflets, in which each leaflet can be sutured at eleven specific suture points aligned in the grids. Furthermore, it had 16 potential suture points for extra fixation for tighter mounting. Segment II was connected to the RVOT crown in order to maintain the integrity of the stent and to ensure a favorable radial force and hoop force.

**Segment III:** Segment III was designed for RVOT anchoring with symmetrical struts connected to segment II. It had the same geometry as segment I, with three strong connective struts at the sagittal commissure.

❖ **DGS-7**

DGS-7 was designed as a vertical, self-expandable Nitinol stent that was 30 mm in diameter and made to host a 30-mm diameter new tri-leaflet heart valve for TPVR. This stent can be used to treat the patients with a patched RVOT following TOF surgery and with a narrowed RVOT. The expanded DGS-7 (30 mm diameter, 36.1 mm height) can be fully crimped to 40.3 mm in height and 6 mm in diameter and can then be loaded into the 18Fr head of a delivery system; see **Figure 26.**

**Segment I:** The top vertical crown of DGS-7 consisted of 18 symmetrical large open cells circumferentially, supplying favorable hoop force and radial force to the pulmonary artery wall. It had three conterminous zones at each commissure in the stent, which linked to segment II to maintain the integrity of the stent. Furthermore, each cell had two conterminous zones that linked with cells in segment II, excluding the three commissures.

**Segment II:** The middle crown was composed of three parts that linked to the top crown and connected them with each other at the three commissures. Segment II can be divided into two functional parts: 1. Y- and 人- joints of cells at the commissural horizontal as sewing symbols, 2. the diamond cell in the third layer of the stent for native heart valve compression to provide the new heart valve with enough space to deliver its action during the cardiac cycle.

Using the two suture lines, surgeons can suture the new heart valve onto the stent via running or interrupted sutures from one specific commissure in a circular fashion back to the beginning. The struts for suturing were linked to the top crown to maintain the integrity of the stent. The diamond cells for native valve compression had a vertical geometry to secure the cylindrical geometry of the new heart valve. They can also protect part of the new heart valve, which was adhered to the stent from the disorganized blood flow.

**Segment III:** Segment III was designed for mounting the new heart valve with 13 specific suture points for each leaflet, four of which had an approximate 人-shape, while the other nine were aligned on the smooth grid for the leaflet edges. It contained five simplified support struts to connect to segment IV to ensure the integrity of the stent as a whole. The edges where the leaflet was attached to the stent can be modified according to various heart valve designs.

**Segment IV:** The fourth segment of DGS-7 was utilized to help the stent anchor at the RVOT and contained three tiny cells as hooks at the bottom that were 90° to each other. In the event of a misalignment, the three hooks may assist the cardiologist in retrieving the device for stented heart valve repositioning. In order to provide balanced radial and hoop forces after implantation, the cells in the RVOT crown were also symmetrical.
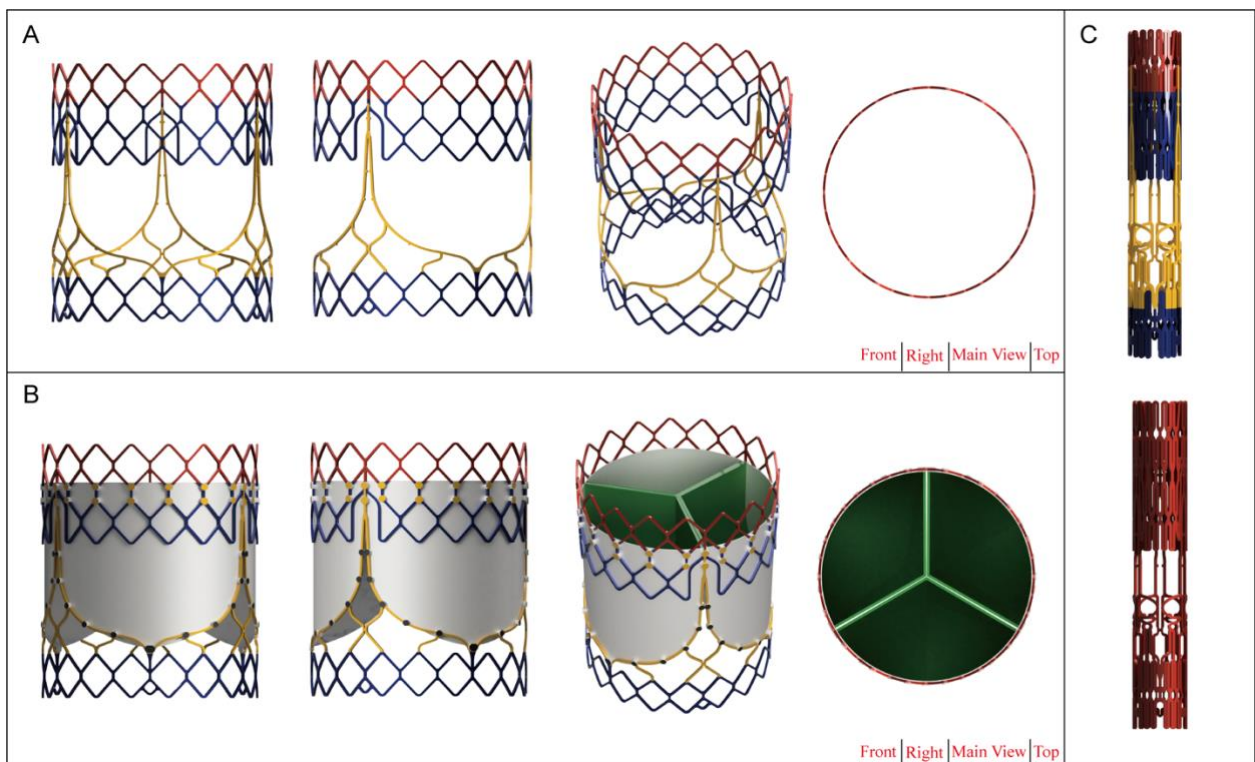


**Figure 26. DGS-7 illustration.**
**A:** Illustration of total DGS-7 stent from four directions; **B:** Illustration of DGS-7 with a virtually sutured autologous pulmonary valve; **C:** Illustration of fully crimped DGS-7.

### ❖ DGS-8B

DGS-8B was a straight tubular stent without crowns at the top, middle, or right atrium of the heart. DGS-8B contained a core segment that was 30 mm in diameter for use with a 30-mm diameter new heart valve. Additionally, DGS-8B may provide an interventional valve-in-valve opportunity for patients who are scheduled to undergo heart valve implantation using other stents to treat valve degradation. In addition, it may be used in patients who experience stented heart valve malfunction during implantation, **Figure 27**.
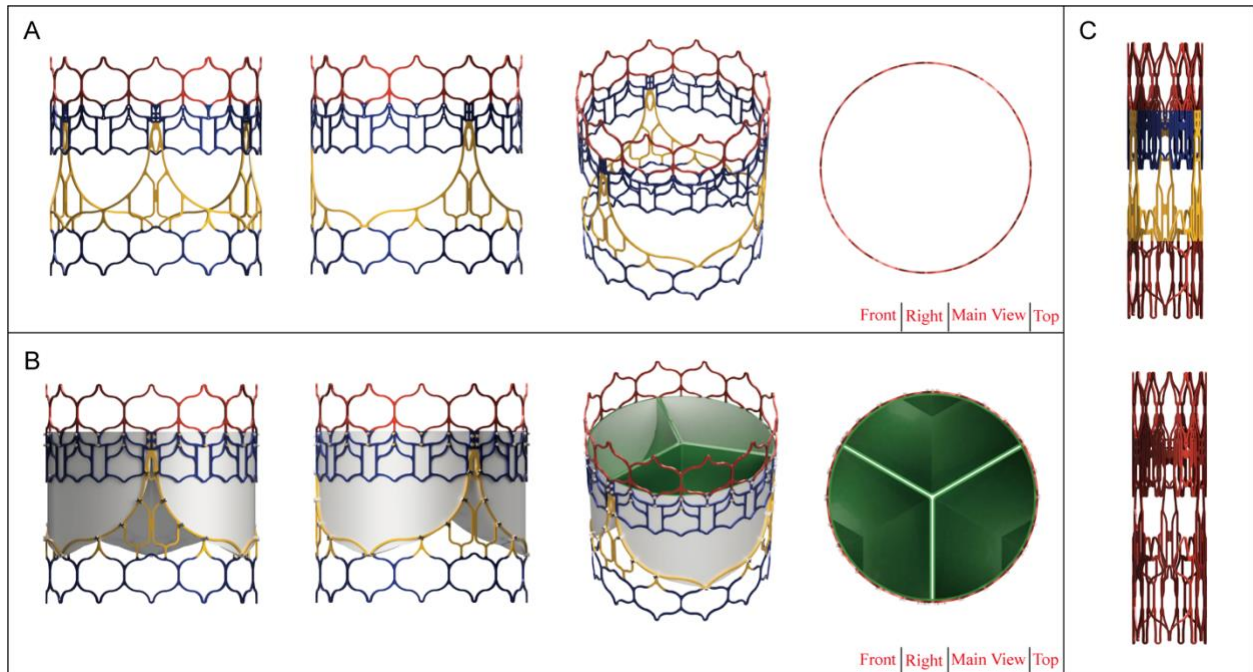


**Figure 27. DGS-8B illustration.**
**A:** Illustration of total DGS-8B stent from four directions; **B:** Illustration of DGS-8B with a virtually sutured autologous pulmonary valve; **C:** Illustration of fully crimped DGS-8B.

### ❖ DGS-10B

DGS-10B was a straight tubular stent with vertical crowns at the top, middle and RVOT, with a diameter of 30 mm to accommodate a 30-mm diameter heart valve, which was available only for straight tubular heart valve designs without a Valsalva sinus. DGS-10B also offers an interventional valve-in-valve opportunity for patients with bioprosthetic valve degradation who are scheduled to undergo interventional heart valve implantation or who experience stented heart valve dysfunction during implantation.

DGS-10B (30 mm diameter) was 30.1 mm in expandable height for transcatheter pulmonary valve implantation. Using a crimping tool, it can be fully crimped to 37.8 mm in height and 7 mm in diameter for use with a 22Fr delivery system; see **Figure 28**.
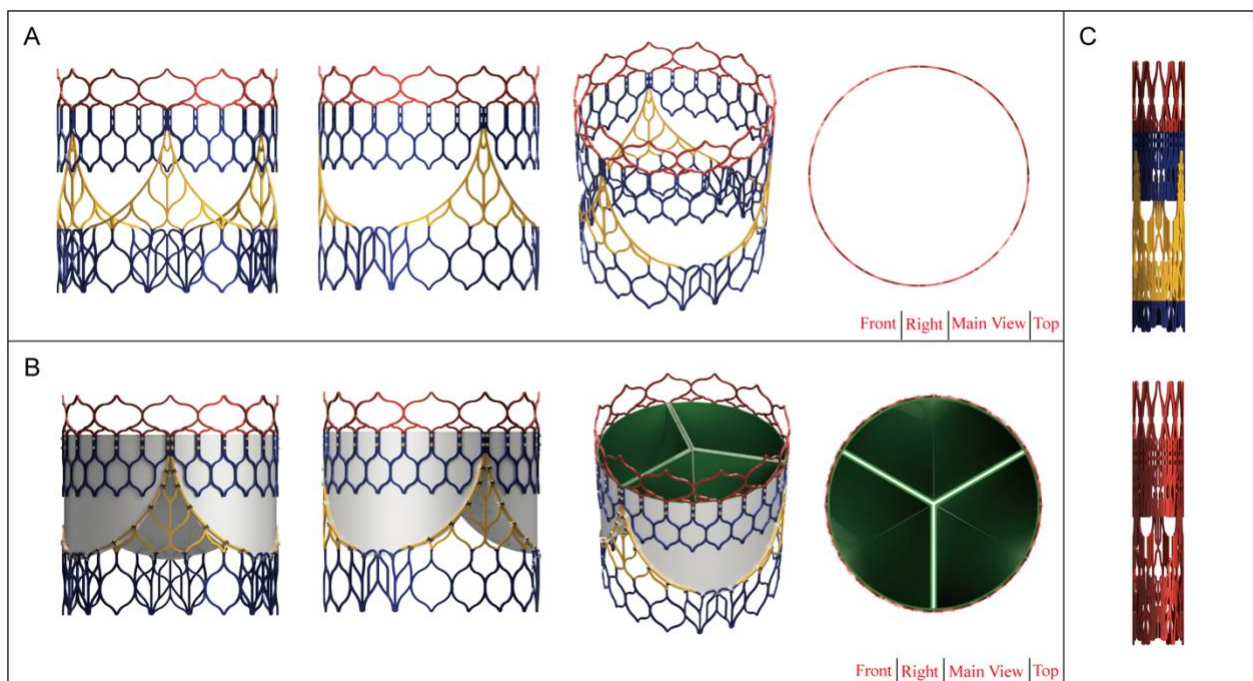


**Figure 28. DGS-10B illustration.**
**A:** Illustration of total DGS-10B stent from four directions; **B:** Illustration of DGS-10B with a virtually sutured autologous pulmonary valve; **C:** Illustration of fully crimped DGS-10B.

### ❖ DGS-12D

DGS-12D was a straight tubular stent with vertical crowns at the top, middle and RVOT. DGS-12D was 30 mm in diameter for a 30-mm diameter heart valve, which was only available for the straight tubular heart valve without a Valsalva sinus. DGS-12D also offers valve-in-valve opportunities for patients with bioprosthetic valve degradation who are scheduled to undergo interventional heart valve implantation or who experience stented heart valve dysfunction during implantation; see **Figure 29.** Using a crimping tool, it can be fully crimped to 37.2 mm in height with 7.2 mm in diameter for use with a 22Fr delivery system.
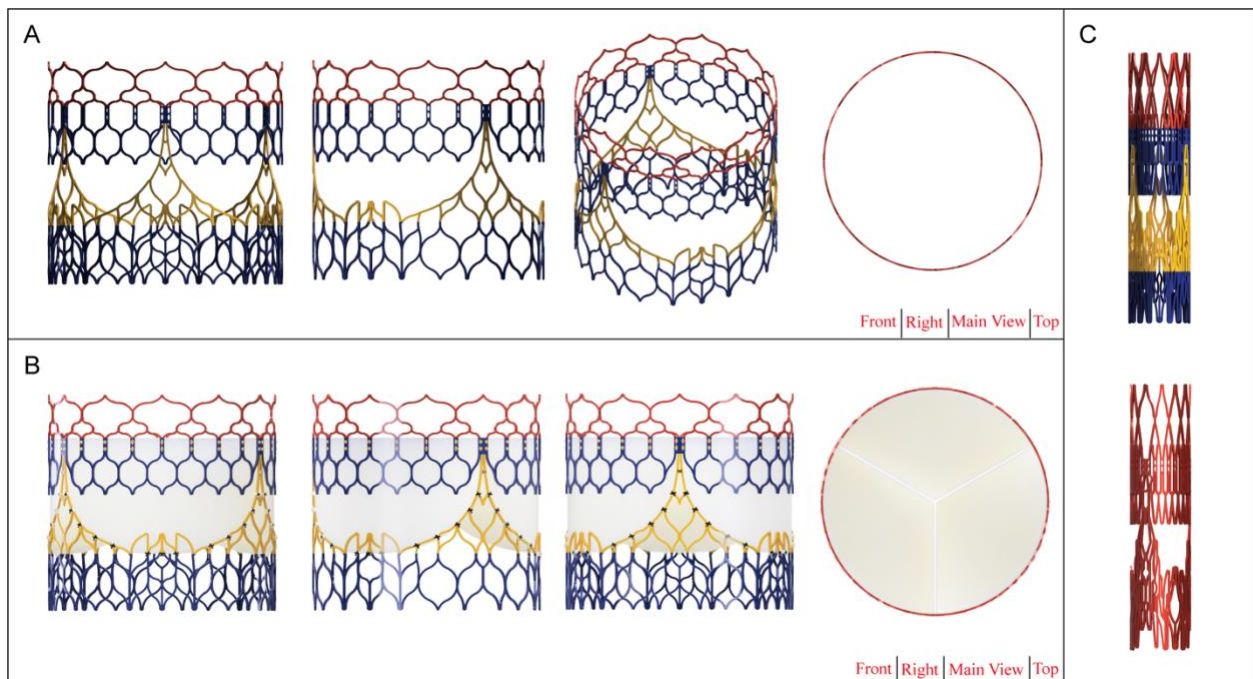


**Figure 29. DGS-12D illustration.**
**A:** Illustration of total DGS-12D stent from four directions; **B:** Illustration of DGS-12D with a virtually sutured autologous pulmonary valve; **C:** Illustration of fully crimped DGS-12D.

### 3.2.2 Group 2

❖ **DGS-8A and DSG-9A**

DGS-8A and DGS-9A can be used to mount tri-leaflets for transcatheter autologous pulmonary valve implantation equipped with self-expandable Nitinol material for treating the patients with a patched RVOT after TOF surgery or with a narrowed RVOT. These stents can be deployed from the top crown going through the middle crown to the basal crown for anchoring at the RVOT. Due to the three crowns, the stents caan be ideally positioned to accommodate various RVOT and PA anatomies, in order to promote benign blood flow conduction through the right ventricle to the pulmonary artery. The large open X-shaped cells at the top and basal crowns, which contain symmetrical structs, can promote a favorable distribution of radial force within the stents. Because of the three crowns, especially the middle and basal crowns, the stent can prevent PVL, coronary artery obstruction and pulmonary annulus rupture peri-operatively. DGS-8A consisted of four functional components; see **Figure 30**.

The difference between DGS-8A and DGS-9A was in the design philosophy of the top lotus crown. The top crown of DGS-8A was designed to be 34 mm in diameter, 2 mm offset from the core segment hosting the 30-mm diameter new heart valve for more extensive dilation of the PA. Furthermore, the top of this crown featured tiny, outstretched arms at the distal end of the cells with an 0.2-mm offset from the top crown. This design served to improve anchoring at the PA and prevent stented heart valve migration during the whole cardiac cycle. DGS-8A can be fully crimped in a crimping tool to 40 mm in height and 10.4 mm in diameter, while the crimped DGS-9A was 10.3 mm in diameter and can be loaded into the head of a 30Fr delivery system.
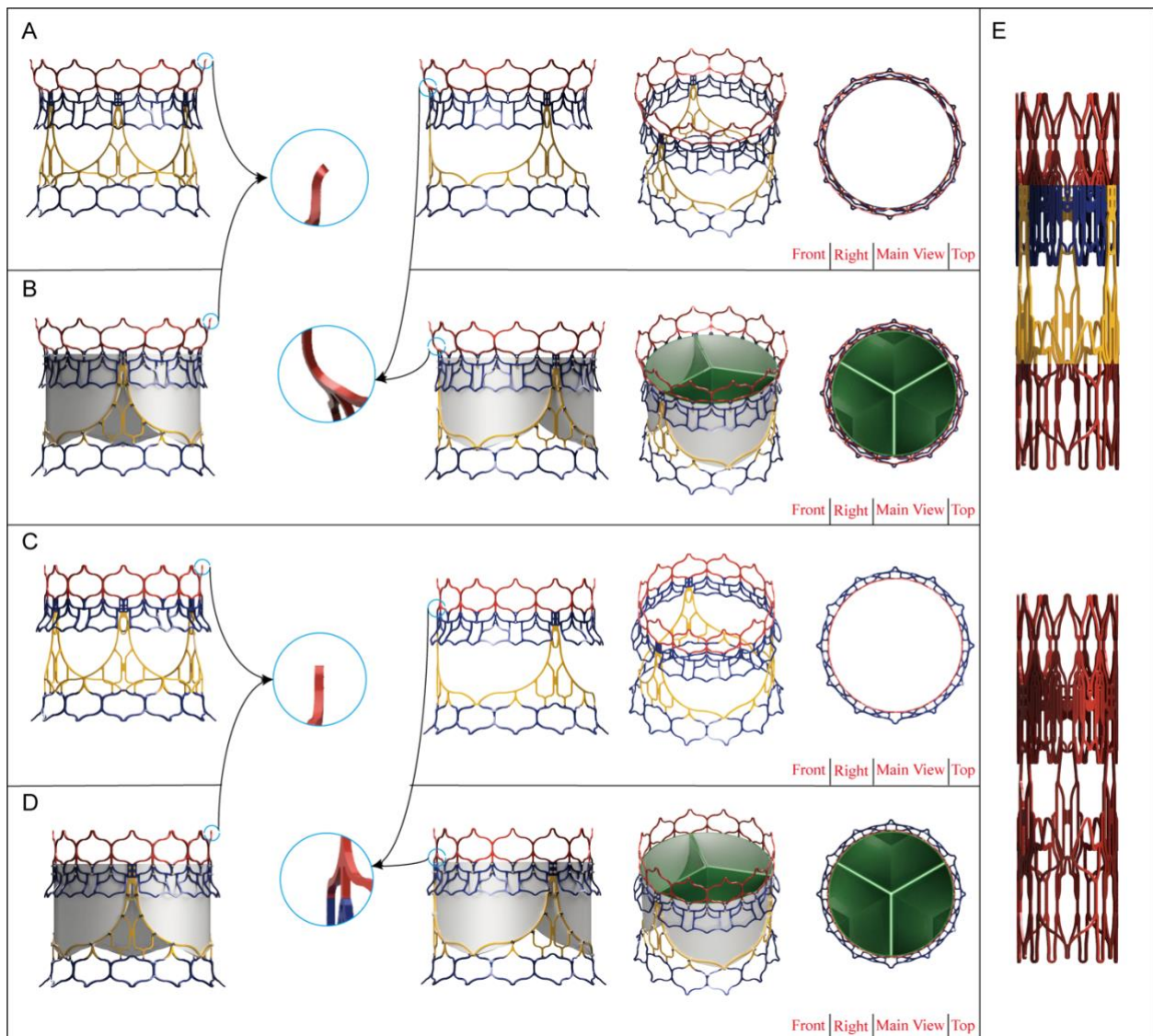
**Figure 30. DGS-8A and DGS-9A illustration.**
**A and C:** Illustration of total DGS-8A and DGS-9A stents from four directions; **B and D:** Illustration of DGS-8A and DGS-9A with virtually sutured autologous pulmonary valves; **E:** Illustration of fully crimped DGS-8A and DGS-9A. Black arrows from **A** and **B**: DGS-8A had a tiny outstretched crown at the top crown, which was also outstretched from segment II, while the top crown of DGS-9A was designed with a vertical geometry aligned to the MPA (see black arrows in **C** and **D**).

## ❖ DGS-10A

DGS-10A was designed into four functional segments with three crowns to host a tri-leaflet heart valve for interventional treatment. The total stent was 31.4 mm in height for a 30-mm diameter heart valve in the fully expanded state, and 39.1 mm in height and 7.1 mm in diameter after being fully crimped in a crimping tool. In this small, crimped configuration, the stented heart valve can be easily manipulated for insertion, **Figure 31**
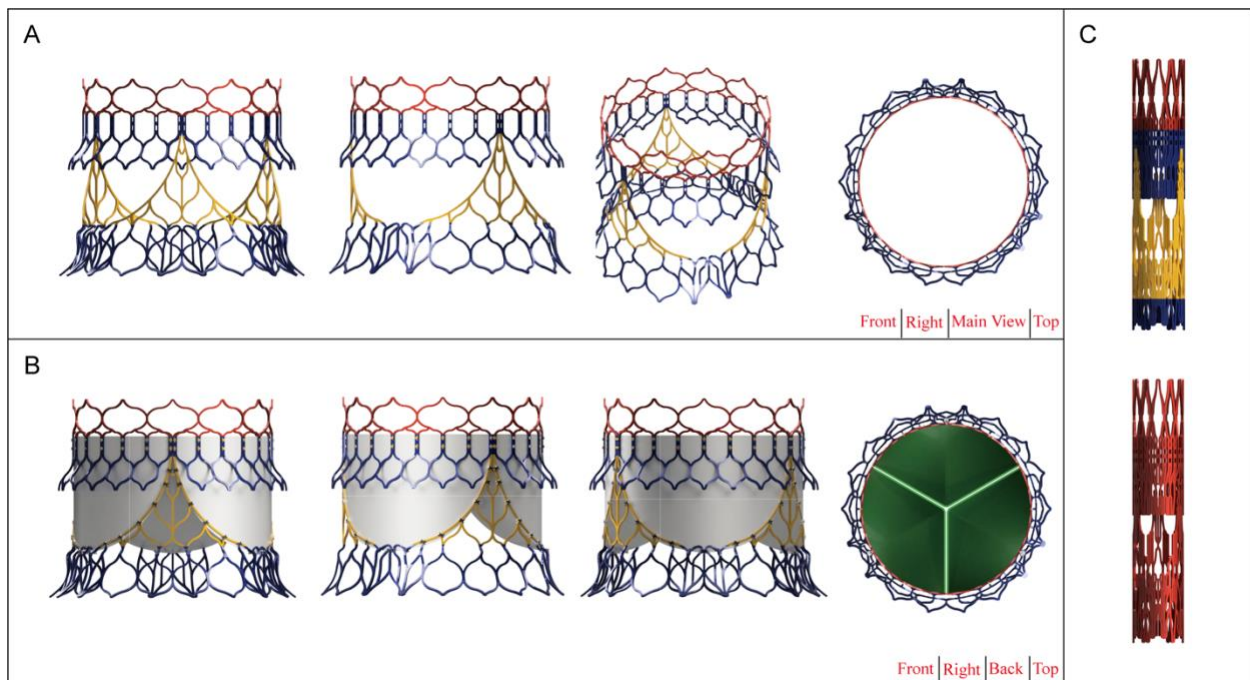


**Figure 31. DGS-10A illustration.**
**A:** Illustration of total DGS-10A stent from four directions; **B:** Illustration of DGS-10A with a virtually sutured autologous pulmonary valve; **C:** Illustration of fully crimped DGS-10A.

**Segment I:** The distal crown to the main pulmonary artery had 12 large open X-shaped cells with a coaxial alignment in accordance with segments II-IV, thus providing ideal blood flow conduction for TOF patients. These large cells were concatenated with the copular struts from segment II, which are designed to keep the stent tranquil during the whole cardiac cycle.

**Segment II:** The two suture lines at the commissural horizontal for heart valve fixation had an equal distance between each suture point and can be sutured with 5-0 polypropylene. The coaptation height of the leaflet was 1.8 mm. At the three commissures, it also provides enough space for the surgeon to further fixate the stent using the Ozaki technique (72) according to the extreme importance of the three commissures.

The three protracted arms linked to the commissural horizontal can compress the native leaflet against the pulmonary wall and provide a relaxed opening to become free of the

opening, especially when the site of implantation has severe calcification and severe surgical scarring. In addition, migration and PVL of the stented heart valve can be prevented by this architecture. Due to the optimized structs, these 2-mm offset arms may be beneficial for a Valsalva heart valve with a low risk of annular rupture, coronary artery obstruction, and paravalvular leak.

**Segment III:** The third segment of DGS-10A was designed to host the new heart valve. Each leaflet had 17 sewing points at approximately equal distances, from 2.7 mm to 3.1 mm, thereby giving the surgeon the option of using running or interrupted sutures at the suture points. With these suture points, each leaflet can be fixed onto the stent appropriately while maintaining the desired geometry of the heart valve. Furthermore, the approximate suturing distance can help the leaflet edges, which are attached to the stent, to withstand the approximate blood pressure during the whole cardiac cycle, ensuring that the stented heart valve has long-term benefits for the patients. Compared to the DGS-12 series, the DGS-10 series lacked the three guard arches at the basal segment. The second functional segment was at the second suture point connection between the two leaflet junctions below the three commissures, which can be used as a hook-connect point with the delivery system to reposition the stented heart valve in case of stent malposition. The stented heart valve may even be retrieved prior to deploying the middle crown.

**Segment IV:** The fourth segment of DGS-10A was designed for RVOT anchoring with two offsets (0.5 mm and 3.5 mm) from the central stent diameter (30 mm). With this crown, migration of the stented heart valve into the pulmonary artery or right ventricle can be prevented during the last step of device deployment. Furthermore, the offsets can minimize the interruption of cardiac conduction bundles and other cardiac structures at the RVOT.

With the three crowns, the stented heart valve may be free of PVL and migration.

### ❖ DGS-12C

DGS-12C was comprised of four functional architectures that can carry the generally circular heart valve; see **Figure 32**. The middle crown of DGS-12C was designed in a circular fashion with the same diameter as the top crown and the top of the RVOT crown. The stent was 30 mm in diameter for a 30-mm heart valve and thus suitable for a heart valve with or without a Valsalva sinus. DGS-12C can be fully crimped in a crimping tool to 37.2 mm in height and 7.2 mm in diameter and can be loaded into the head of a 22Fr delivery system.
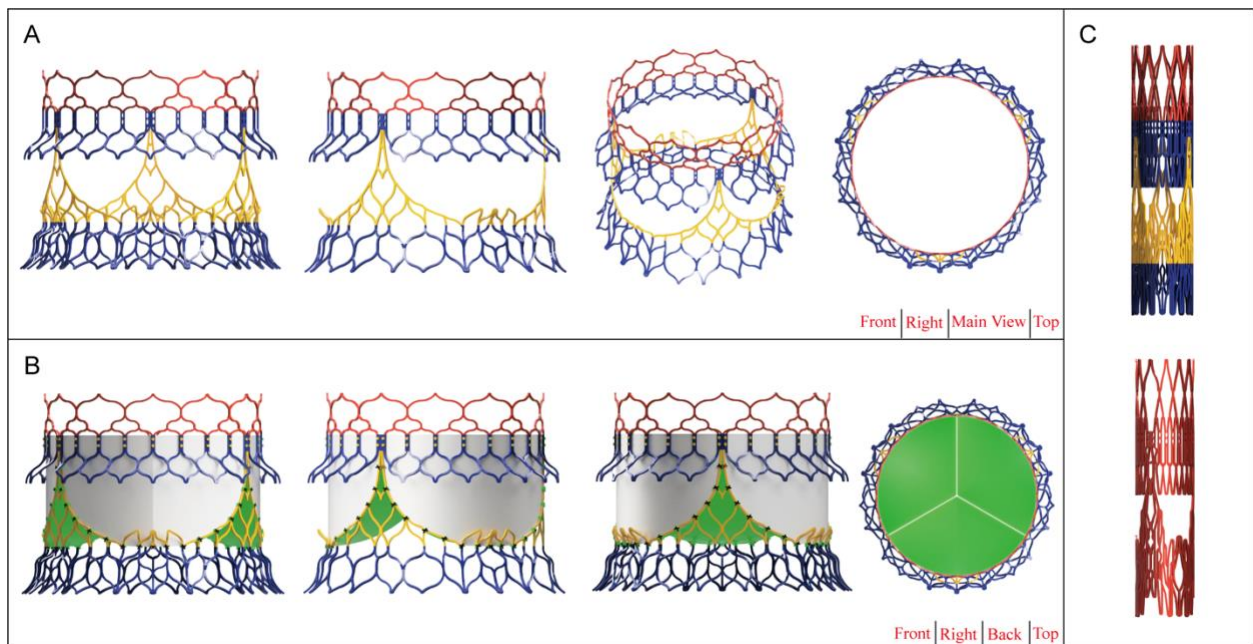


**Figure 32. DGS-12C illustration.**
**A:** Illustration of total DGS-12C stent from four directions; **B:** Illustration of DGS-12C with a virtually sutured autologous pulmonary valve; **C:** Illustration of fully crimped DGS-12C.

### 3.2.3   Group 3

❖ **DGS-12A and DGS-12B**

**Segment I:** The distal segment (34 mm diameter) of the top crown was designed with a circular architecture according to the PA anatomy. Meanwhile, the proximal segment of the top corollaceous crown was oval (30 mm: 36 mm) with a ratio of 1:1.2. The circular segment was gradually transitioned into ovality. Accordingly, the top crown with 12 stabilized cells provided better coaxial alignment, which is beneficial for anchoring at the main pulmonary artery trunk. The large open-cell design can promote better blood flow conduction, especially for TOF patients with a hypoplastic pulmonary artery trunk and/or main branches, prior to radical correction. Three struts of the 12 X-shaped open cells were firmly connected with the two commissural horizontal suture lines in order to maintain the strength of the stent.

**Segment II:** The two suture lines provided adequate space for surgeons to suture the heart valve at the commissural horizontal with running or interrupted sutures using 5-0 polypropylene. At the three commissures, further interrupted suture spaces are also available for fixation using special techniques, such as the Ozaki procedure for commissural fixation. The three guard arms connected to the suture lines provide the new heart valve with enough space to abolish any impact from the native heart valve while simultaneously compressing the native valve, especially in severe calcification, in order to provide ample space for the new heart valve with or without Valsalva sinuses. Furthermore, this architecture can also prevent migration of the stented heart valve from its ideal position despite blood stress during the filling phase of the cardiac cycle. The ovality of this segment was 2 mm offset from the commissural fixation part, providing a balanced profile with a low risk of annular rupture, coronary artery obstruction, and paravalvular leak.

**Segment III:** Each leaflet frame had 17 sewing points at approximately equal distances, from 2.7 mm to 3.1 mm, providing the surgeon with determinate suture points during the surgery for running or interrupted sutures. These suture points can be used to firmly fix the heart valve to the stent while maintaining the approximate stress of the new heart valve during the whole cardiac cycle to prevent it from tearing or loss. The primary function of the three guard arches was to protect the basal segment of the heart valve from blood flow; the second was to compress the native heart valve in order to provide the new heart valve with enough space. The third function was to prevent migration of the stented heart valve in the direction of the pulmonary artery and the RVOT; the fourth

functional segment was at the second suture point connections between the two leaflet junctions below the three commissures, which can be used as a hook-connect point with the delivery system to reposition the stented heart valve in case of stent malposition. The stented heart valve may also be retrieved prior to deploying the middle crown. The outer geometry of this segment was an elliptical cylinder. The distance between the three guard arches and the guard arms at the middle crown was 10 mm, offering enough space for coronary artery catheterization when used in the aortic position.

**Segment IV:** The fourth functional segment of DGS-12A and DGS-12B was designed for RVOT anchoring and comprised two slick secure layers to help the stented heart valve adhere to the RVOT without interrupting cardiac conduction bundles and other cardiac structures at the RVOT. These two secure architectures also help prevent migration of the stented heart valve towards the pulmonary artery.

Segments I-IV were designed with an oval geometry to embrace the RVOT anatomy gently and fully with a short- and long -axis ratio of 1:1.2; see **Figure 34** and **Figure 33**. To a certain extent, this design can reduce the incidence of paravalvular leak and enhance blood flow conduction from the RVOT to the pulmonary artery via the heart valve.

The aim of DGS-12A and DGS-12B was to load a tricuspid valve; however, the heart valve attachment at the three commissures in an oval stent should be two-style, owing to the asymmetrical nature of the ovality. Therefore, the difference between DGS-12A and DGS-12B was the position of one of the commissures sutured into the stent at the long axis or the short axis of the ovality.
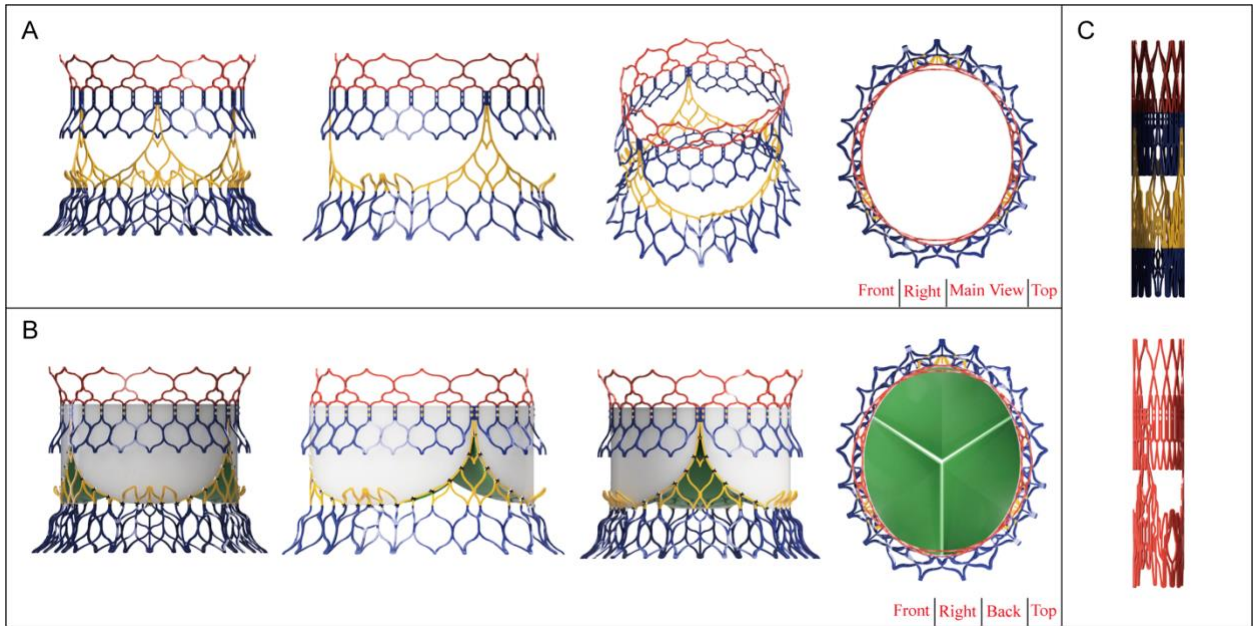
**Figure 34. DGS-12A illustration.**
**A:** Illustration of total DGS-12A stent from four directions; **B:** Illustration of DGS-12A with a virtually sutured autologous pulmonary valve; **C:** Illustration of fully crimped DGS-12A.
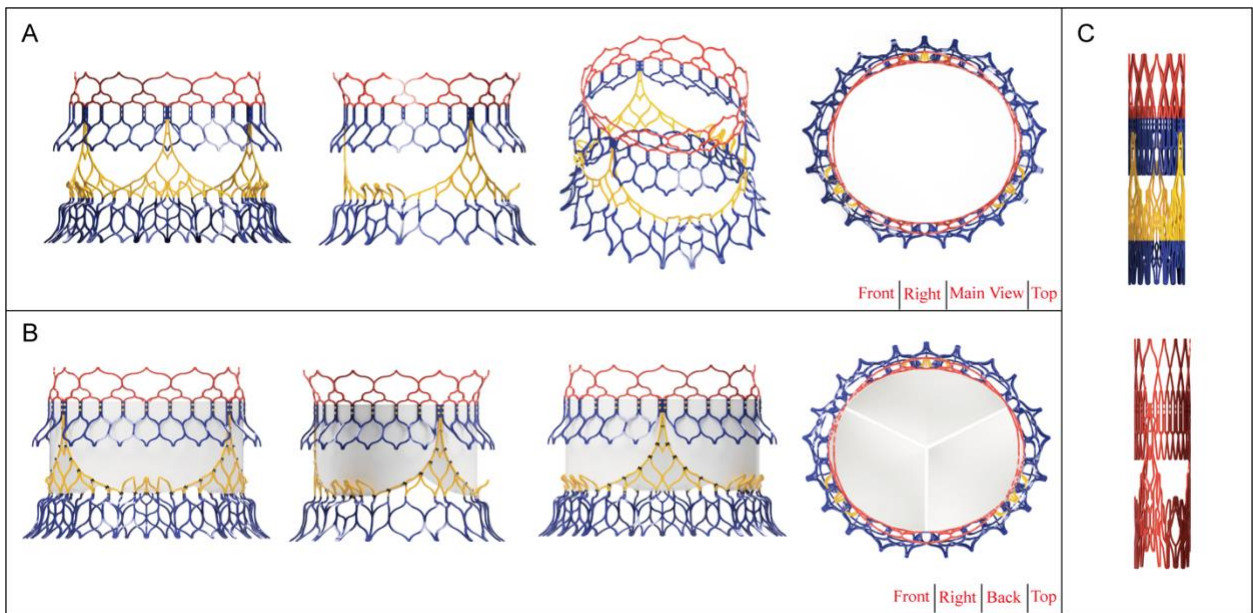


**Figure 33. DGS-12B illustration.**
**A:** Illustration of total DGS-12B stent from four directions; **B:** Illustration of DGS-12B with a virtually sutured autologous pulmonary valve; **C:** Illustration of fully crimped DGS-12B.

## 3.3. Right ventricle + pulmonary artery blood flow simulation

The right ventricular and main pulmonary artery blood flow simulation was successfully computed in Ansys 2021 R2 Fluent using the Animal J Pre-CT model, which demonstrated that the anterior blood flow of the PA had the largest pressure using the velo city-based coupled solver; see **Figure 35**.
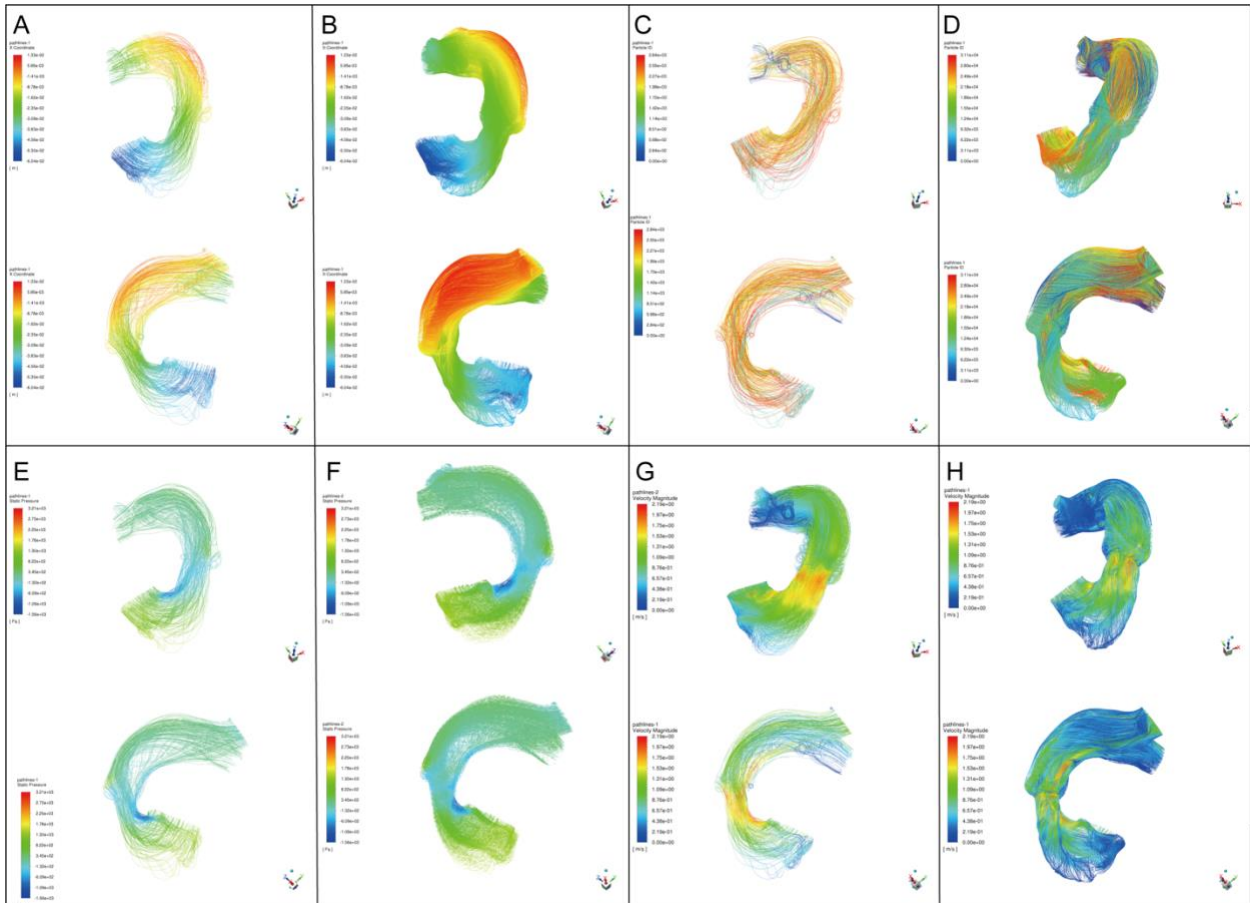


**Figure 35. Right ventricular + main pulmonary artery blood flow simulation**
**A:** Mesh X-coordinate based without pulmonary artery wall, **B:** Mesh X-coordinate based without pulmonary artery wall, **C:** Particle ID based without pulmonary artery wall, **D:** Particle ID based without pulmonary artery wall, **E:** Velocity-based without pulmonary artery wall, **F:** Velocity-based with pulmonary artery wall, **G:** Pressure-based without pulmonary artery wall, **H:** Pressure-based with pulmonary artery wall.

### 3.4. Right ventricle + pulmonary artery shear force simulation

The right ventricular and main pulmonary artery blood flow simulation was successfully computed in Ansys 2021 R2 Fluent using the Animal J Pre-CT model, which demonstrated that the anterior leaflet and anterior of the PA wall had the largest shear force; see **Figure 36**.
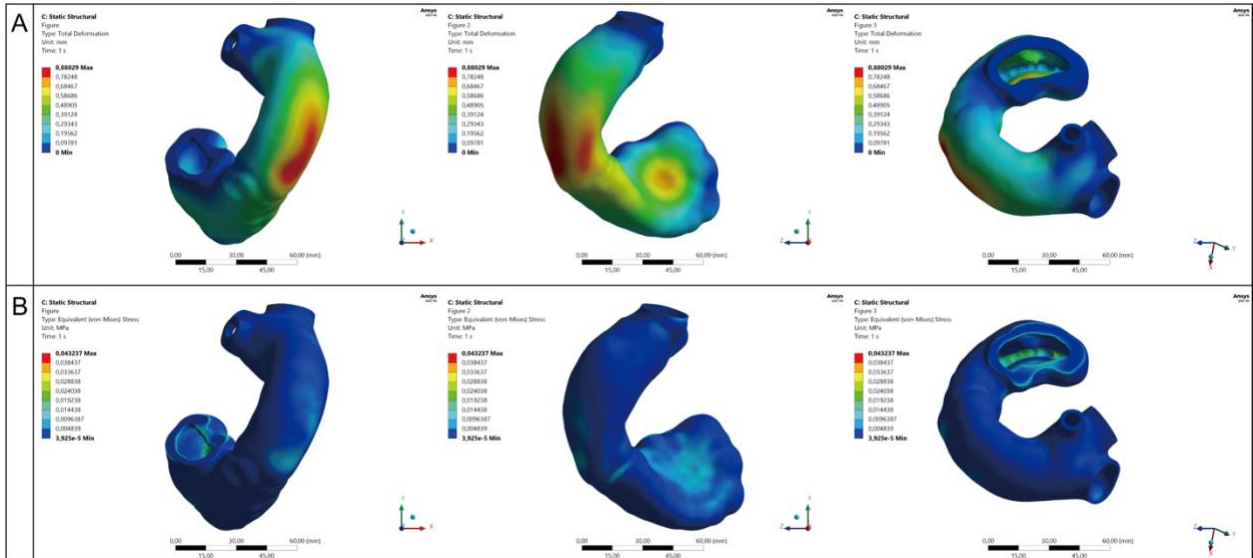


**Figure 36. Simulation of shear force.**
**A:** Total deformation of 3D model shows the shear force of blood flow at the anterior wall of the pulmonary artery, **B:** Equivalent stress from cardiac cycle: Minimum [MPa]: 3.925e-005 Maximum [MPa]: 4.3237e-002, and Average [MPa]: 3.2188e-003.

### 3.5. DGS stent simulation for stent life and radial force

### 3.5.1 Simulation of DGS stent life and radial force in Group 1

#### ❖ Simulation of <u>DGS-3</u> stent life and radial force

After model fault examinations and repairs in SpaceClaim, the DGS-3 mesh was generated using the Triangle method with 0.05 mm element size, 102218 nodes, and 42859 elements. DGS-3 was crimped to 11.211 mm on the X-axis and 5.3474 mm on the Z-axis in the coordinate system to mimic the final crimping procedure at the head of the delivery system. After adding the displacements of total deformation and directional deformation while setting the analysis data, the DGS-3 life was obtained as Minimum: 0, Maximum: 3219.2, and Average: 0.77241. After preforming the total deformation and directional deformation, the radial force was obtained as: X-axis: -1.8811e+005 [N], Y-axis: -5.2971e-003 [N], Z-axis: -79.375 [N], total: 1.8811e+005 [N]; see **Figure 37**.
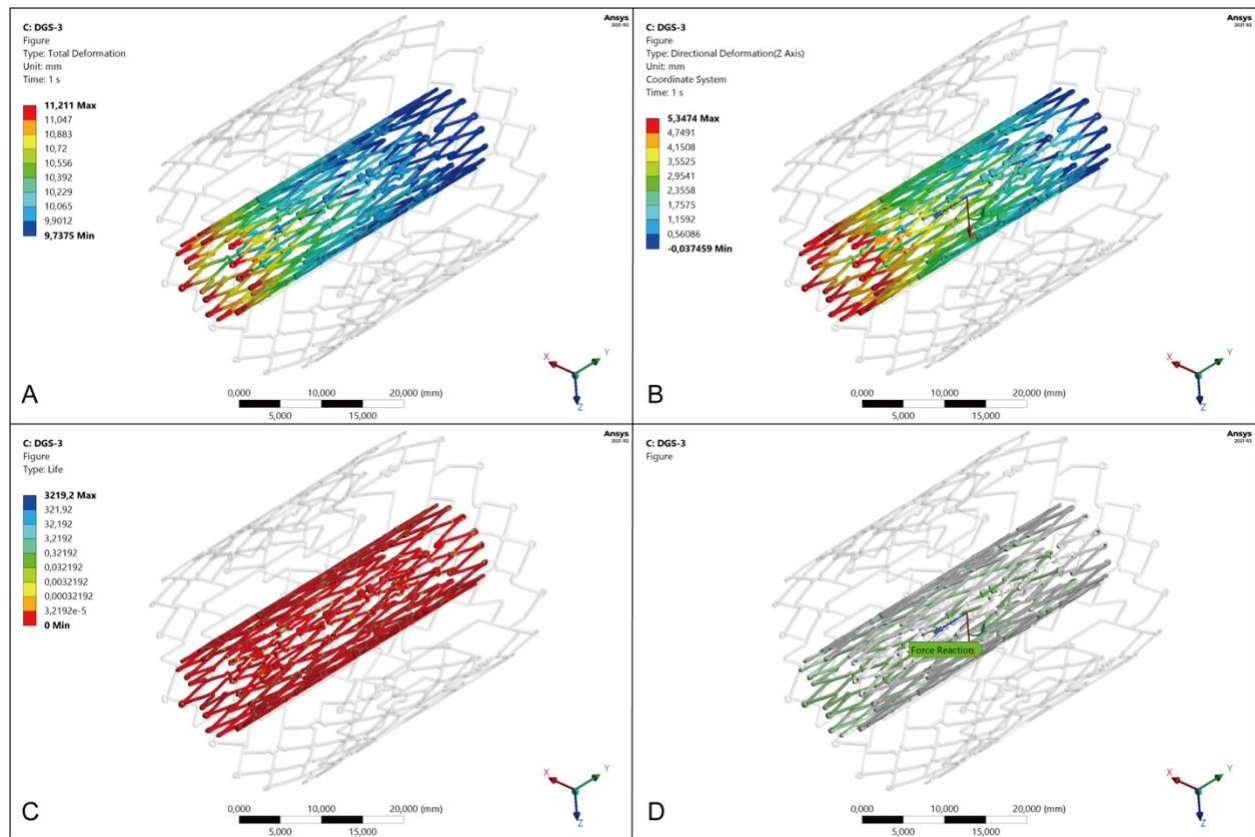


**Figure 37. Simulation of DGS-3 stent life and radial force**
**A:** Total deformation of DGS-3, **B:** Directional deformation of DGS-3, **C:** Maximum life of DGS-3: 3219.2, **D:** Average radial force of DGS-3: X-axis: -1.8811e+005 [N], Y-axis: -5.2971e-003 [N], Z-axis: -79.375 [N], total: 1.8811e+005 [N].

## ❖ Simulation of <u>DGS-5</u> stent life and radial force

After model fault examinations and repairs in SpaceClaim, the DGS-5 mesh was generated using the Triangle method with 0.05 mm element size, 358334 nodes, and 179521 elements. DGS-5 was crimped to 12.462 mm on the X-axis and 5.4818 mm on the Z-axis in the coordinate system to mimic the final crimping procedure at the head of the delivery system. After adding the displacements of total deformation and directional deformation while setting the analysis data, the DGS-5 life was obtained as Minimum: 0, Maximum: 16406, and Average: 5.8185. After preforming the total deformation and directional deformation, the radial force was obtained as: X-axis: -1.9404e+005 [N], Y-axis: -0.21931 [N], Z-axis: 42.752 [N], total: 1.9404e+005 [N] as shown in **Figure 38.**
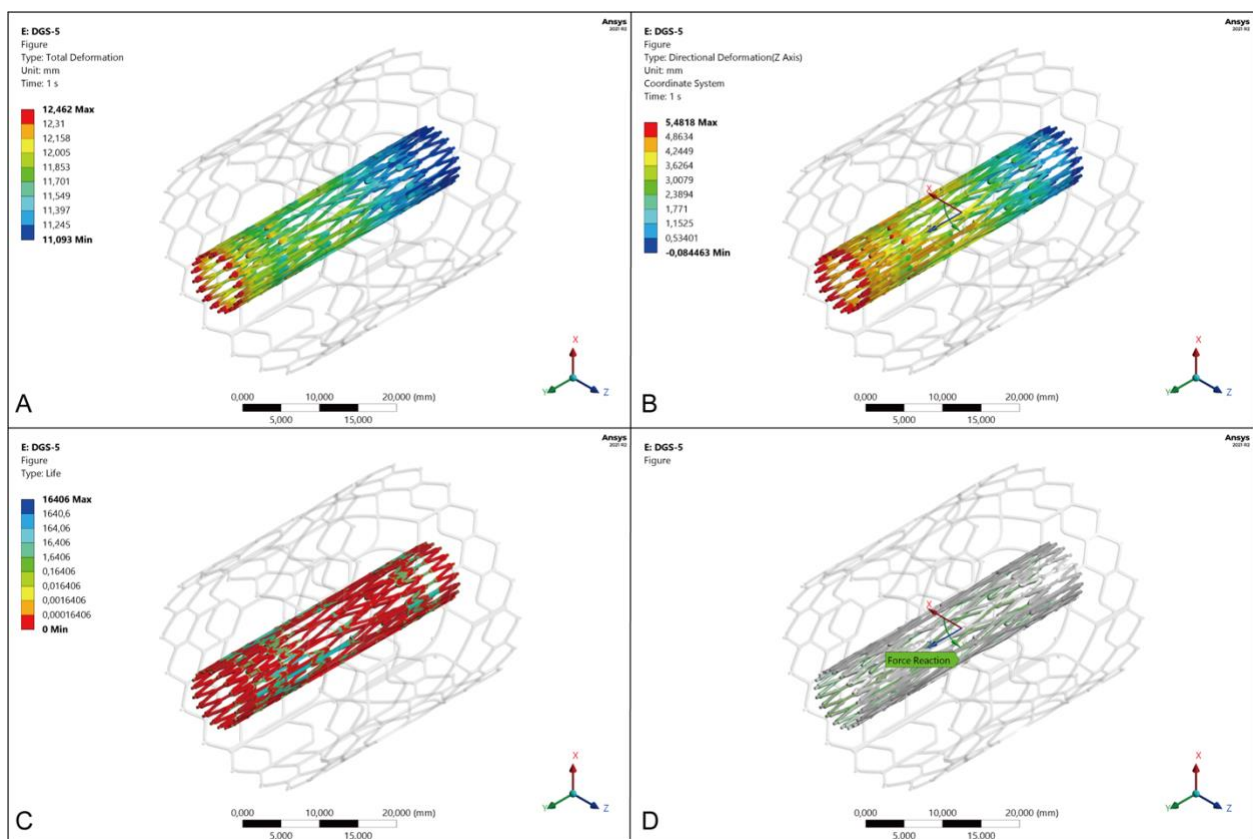


**Figure 38. Simulation of DGS-5 stent life and radial force**
**A:** Total deformation of DGS-5; **B:** Directional deformation of DGS-5, **C:** Maximum life of DGS-5: 16406, **D**: Average radial force of DGS-5: X-axis: -1.9404e+005 [N], Y-axis: -0.21931 [N], Z-axis: 42.752 [N], total: 1.9404e+005 [N].

## ❖ Simulation of <u>DGS-7</u> stent life and radial force

After model fault examinations and repairs in SpaceClaim, the DGS-7 mesh was generated using the Triangle method with 0.05 mm element size, 332183 nodes, and 165706 elements. DGS-7 was crimped to 13.096 mm on the X-axis and 5.2819 mm on the Z-axis in the coordinate system to mimic the final crimping procedure at the head of the delivery system. After adding the displacements of total deformation and directional deformation while setting the analysis data, the DGS-7 life was obtained as Minimum: 0, Maximum: 1e+006, and Average: 8.5584. After preforming the total deformation and directional deformation, the radial force was obtained as: X-axis: -1.8868e+005 [N], Y-axis: 0.16787 [N], Z-axis: -39.121 [N], total: 1.8868e+005 [N] as shown in **Figure 38**.
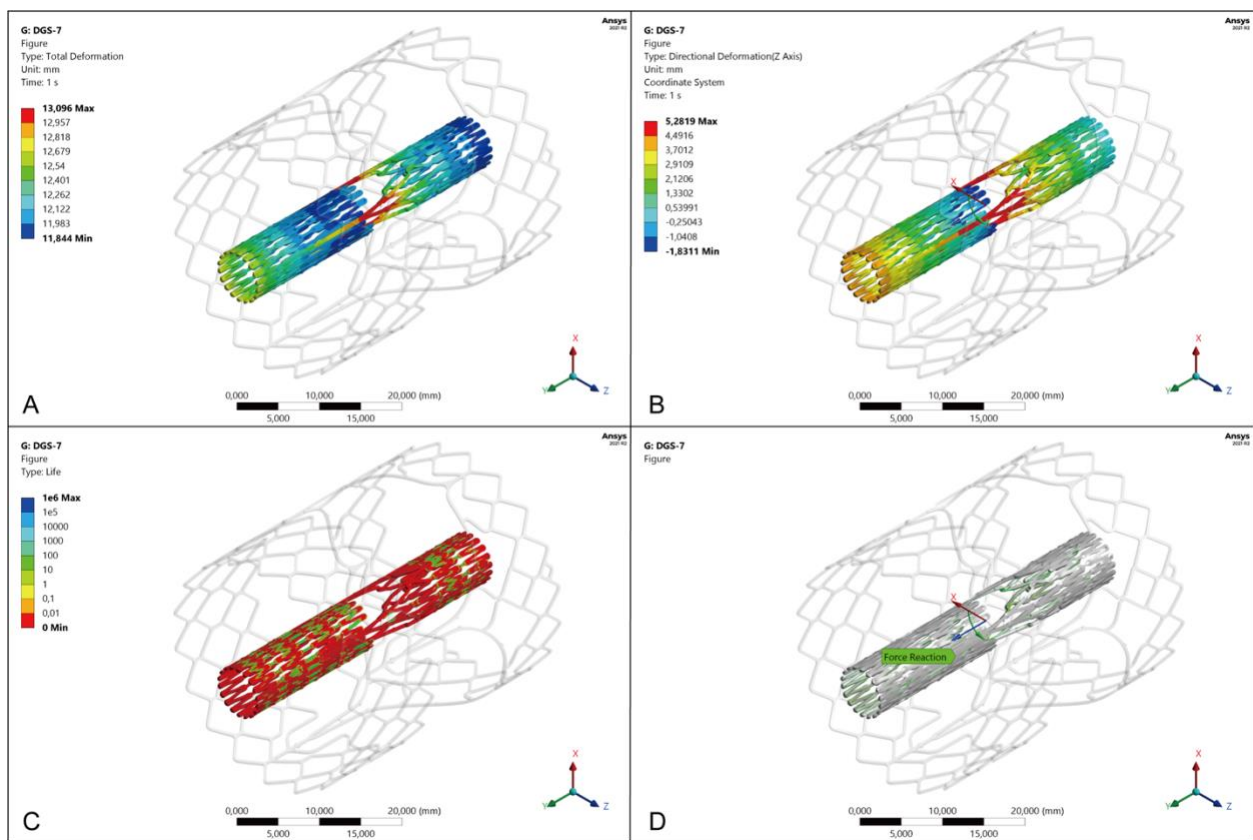


**Figure 39. Simulation of DGS-7 stent life and radial force.**
**A:** Total deformation of DGS-7; **B:** Directional deformation of DGS-7, **C:** Maximum life of DGS-7: 1. e+006, **D**: Average radial force of DGS-7: X-axis: -1.8868e+005 [N], Y-axis: 0.16787 [N], Z-axis: -39.121 [N], total: 1.8868e+005 [N].

## ❖ Simulation of <u>DGS-8B</u> stent life, radial force, and hoop force

After model fault examinations and repairs in SpaceClaim, the DGS-8B mesh was generated using the Triangle method with 0.1 mm element size, 52177 nodes, and 81334 elements. DGS-8B was crimped to 12.865 mm on the X-axis and 3.432 mm on the Z-axis in the coordinate system to mimic the final crimping procedure at the head of the delivery system. After adding the displacements of total deformation and directional deformation and setting the analysis data, the DGS-8B life was obtained as 0, radial force: X-axis  -3.7378e+005  [N],  Y-axis  1.6704e-004  [N],  Z-axis  -2.1931e-008  [N],  total 3.7378e+005 [N]; see **Figure 40**.
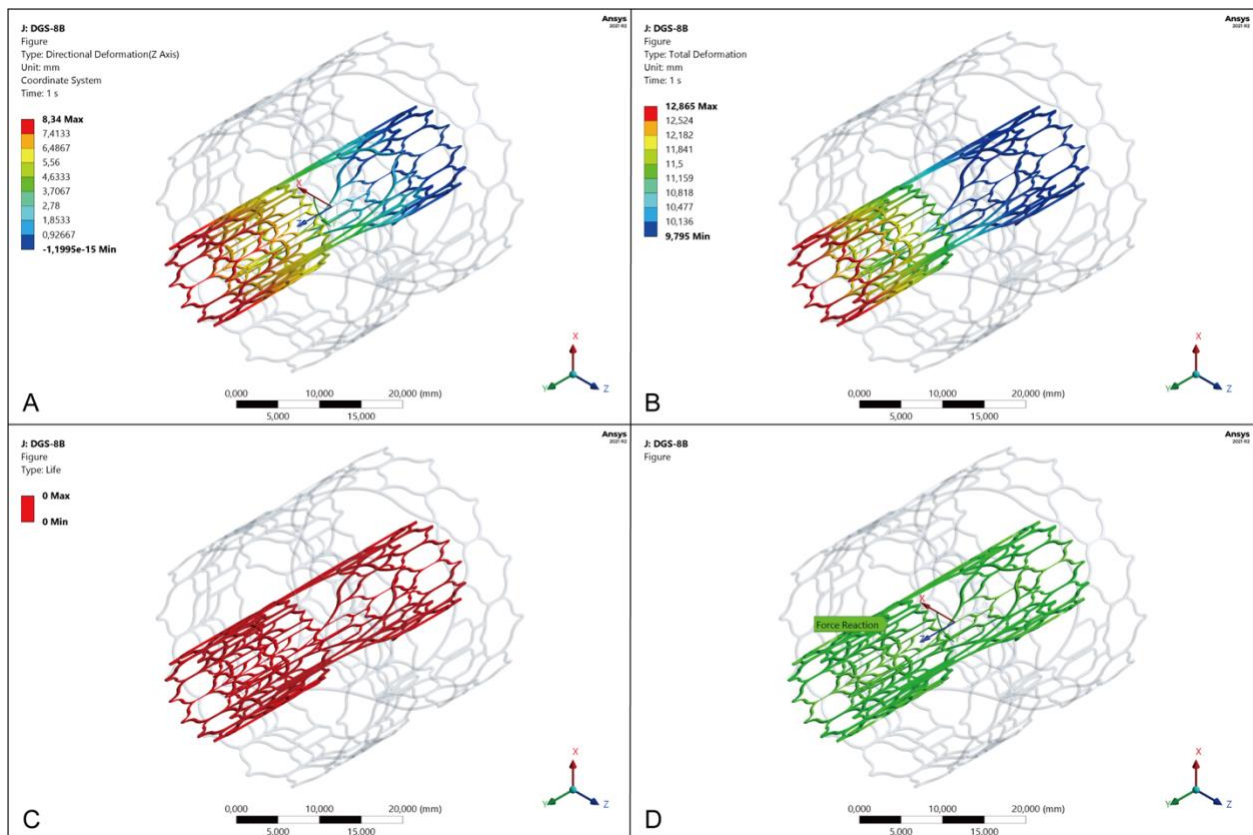


**Figure 40. Simulation of DGS-8B stent life and radial force**
**A:** Total deformation of DGS-8B; **B:** Directional deformation of DGS-8B, **C**: Maximum life of DGS-8B: 0, **D:** Average radial force of DGS-8B: X-axis -3.7378e+005 [N], Y-axis 1.6704e-004 [N], Z-axis -2.1931e-008 [N], total 3.7378e+005 [N].

❖ **Simulation of <u>DGS-10B</u> stent life, radial force, and hoop force**

After model fault examinations and repairs in SpaceClaim, the DGS-10B mesh was generated using the Triangle method with 0.1 mm element size, 55065 nodes, and 83828 elements. DGS-10B was crimped to 12.575 mm on the X-axis and 3.432 mm on the Z-axis in the coordinate system to mimic the final crimping procedure at the head of the delivery system. After adding the displacements of total deformation and directional deformation while setting the analysis data, the DGS-10B life was obtained as Minimum: 0, Maximum: 8370.1, Average: 1.0603. After preforming the total deformation and directional deformation, the radial force was obtained as: X-axis: -2.4127e+005[N], Y-axis: 2.8678e-002 [N], Z-axis: 2.3733e-008 [N], total: 2.4127e+005 [N]; see **Figure 41**.
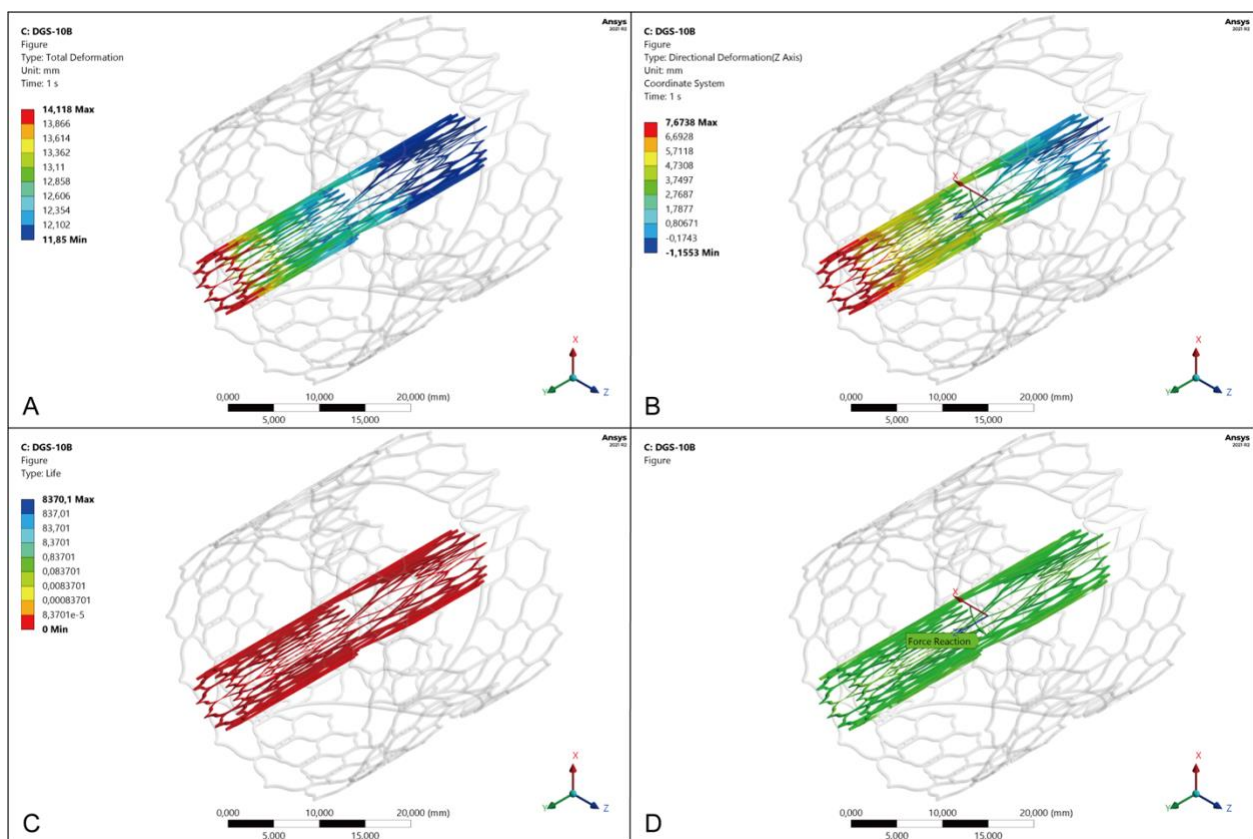


**Figure 41. Simulation of DGS-10B stent life and radial force**
**A:** Total deformation of DGS-10B; **B:** Directional deformation of DGS-10B, **C:** Maximum life of DGS-10B: 1.0603, **D**: Average radial force of DGS-10B: X-axis: -2.4127e+005, Y-axis: 2.8678e-002 [N], Z-axis: 2.3733e-008 [N], total: 2.4127e+005 [N].

❖ **Simulation of <u>DGS-12D</u> stent life, radial force, and hoop force**

After model fault examinations and repairs in SpaceClaim, the DGS-12D mesh was generated using the Triangle method with default element size, 62353 nodes, and 180759 elements. DGS-12D was crimped to 11.168 mm on the X-axis and 4 mm on the Z-axis in the coordinate system to mimic the final crimping procedure at the head of the delivery system. After adding the displacements of total deformation and directional deformation and setting the analysis data, the DGS-12D life was obtained as Minimum: 1e+006, Maximum: 1e+006, Average: 1e+006. After preforming the total deformation and directional deformation, the radial force was obtained as: X-axis: -2.4068e+008 [N], Y-axis: -7049.8 [N], Z-axis-43.719 [N], total: 2.4068e+008 [N]; see **Figure 42**.
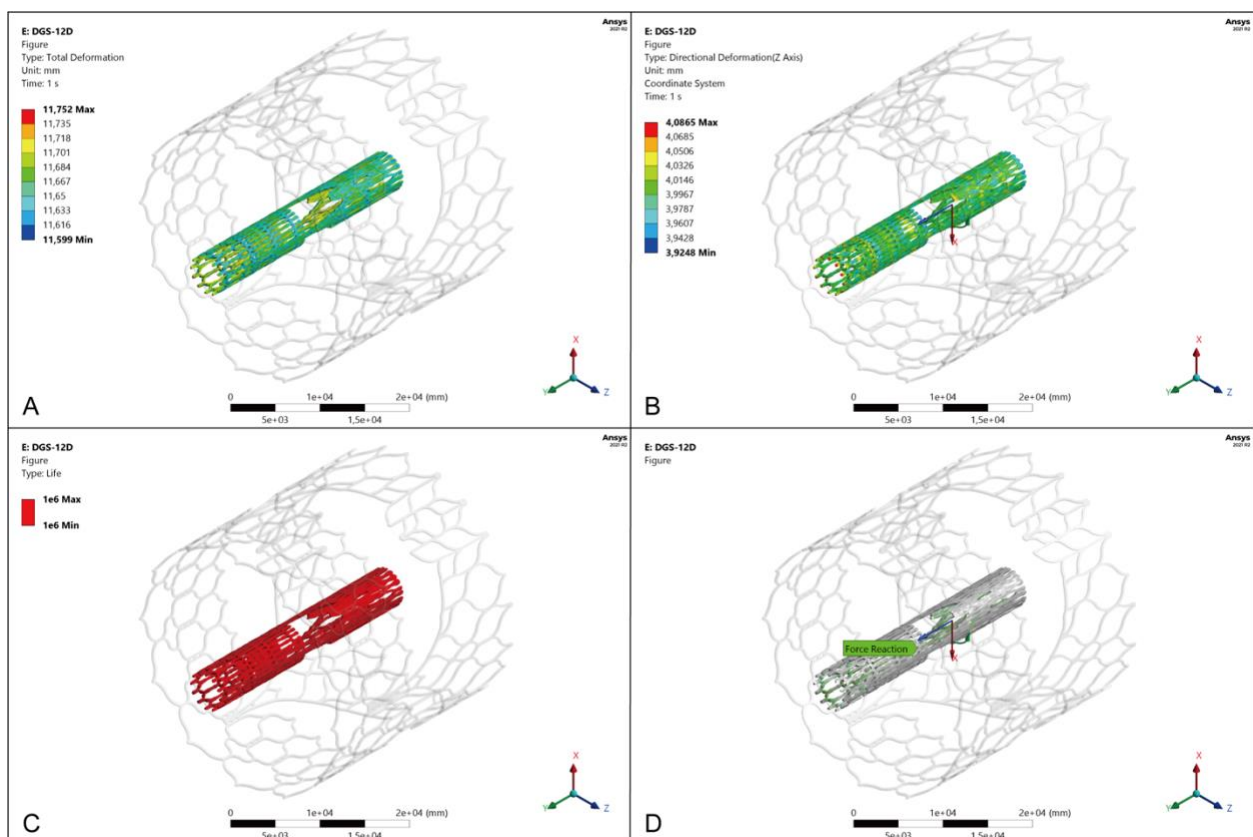


**Figure 42. Simulation of DGS-12D stent life and radial force**
**A:** Total deformation of DGS-12D, **B:** Directional deformation of DGS-12D, **C:** Maximum life of DGS-12D: 1. e+006, **D:** Average radial force of DGS-12D:  X axis 2.4068e+008 [N], Y axis:  7049.8 [N], Z axis-43.719 [N], total: 2.4068e+008 [N].

### 3.5.2 Simulation of DGS stent life, radial force, and hoop force in Group 2

### ❖ Simulation of <u>DGS-8A</u> stent life, radial force, and hoop force

After model fault examinations and repairs in SpaceClaim, the DGS-8A mesh was generated using the Triangle method with 0.1 mm element size, 53836 nodes, and 84234 elements. DGS-8A was crimped to 11.622 mm on the X-axis and 5.4805 mm on the Z-axis in the coordinate system to mimic the final crimping procedure at the head of the delivery system. After adding the displacements of total deformation and directional deformation while setting the analysis data, the DGS-8A life was obtained as Minimum: 0, Maximum: 0, Average: 0. After preforming the total deformation and directional deformation, the radial force was obtained as: X-axis: -3.6033e+005 [N], Y-axis: 6.2188 [N], Z-axis: -6,8305e-006 [N], total: 3.6033e+005 [N] as shown in **Figure 43**.
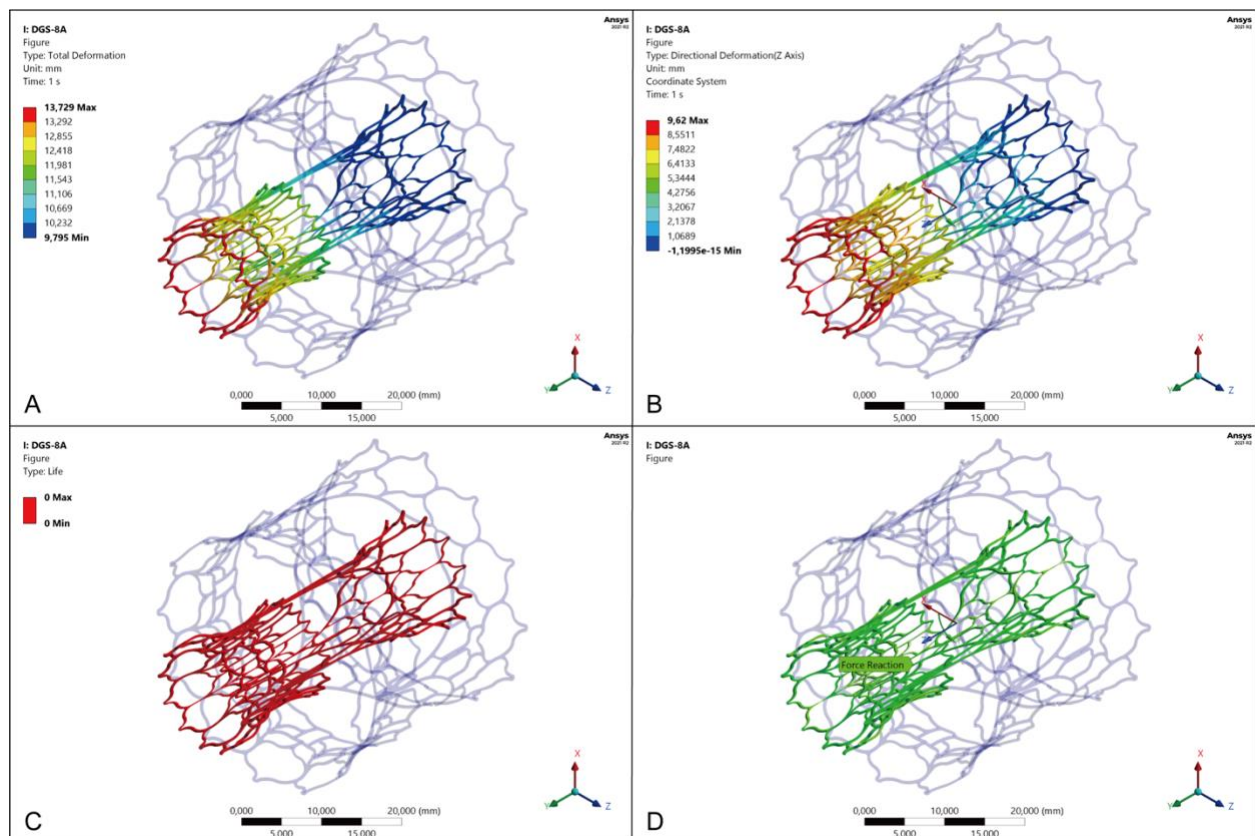


**Figure 43. Simulation of DGS-8A stent life and radial force**
**A:** Total deformation of DGS-8A; **B:** Directional deformation of DGS-8A, **C**: Maximum life of DGS-8A: 46093, **D:** Average radial force of DGS-8A: X-axis: -3.6033e+005 [N], Y-axis: 6.2188 [N], Z-axis: --6,8305e-006 [N], total: 3.6033e+005 [N].

## ❖ Simulation of <u>DGS-9A</u> stent life, radial force, and hoop force

After model fault examinations and repairs in SpaceClaim, the DGS-9A mesh was generated using the Triangle method with 0.1 mm element size, 53836 nodes, and 84234 elements. DGS-9A was crimped to 11.186 mm on the X-axis and 5.1835 mm on the Z-axis in the coordinate system to mimic the final crimping procedure at the head of the delivery system. After adding the displacements of total deformation and directional deformation while setting the analysis data (supplementary file: DGS-9A Mechanical Report), the DGS-9A life was obtained as Minimum: 0, Maximum: 0, and Average: 0. After preforming the total deformation and directional deformation, the radial force was obtained as: Maximum Value Over Time: X-axis: -3,6033 e+005 [N], Y-axis: 6,2188 [N], Z-axis: -6,8305e-006 [N], total: 3,6033 e+005 [N] as shown in **Figure 44**.
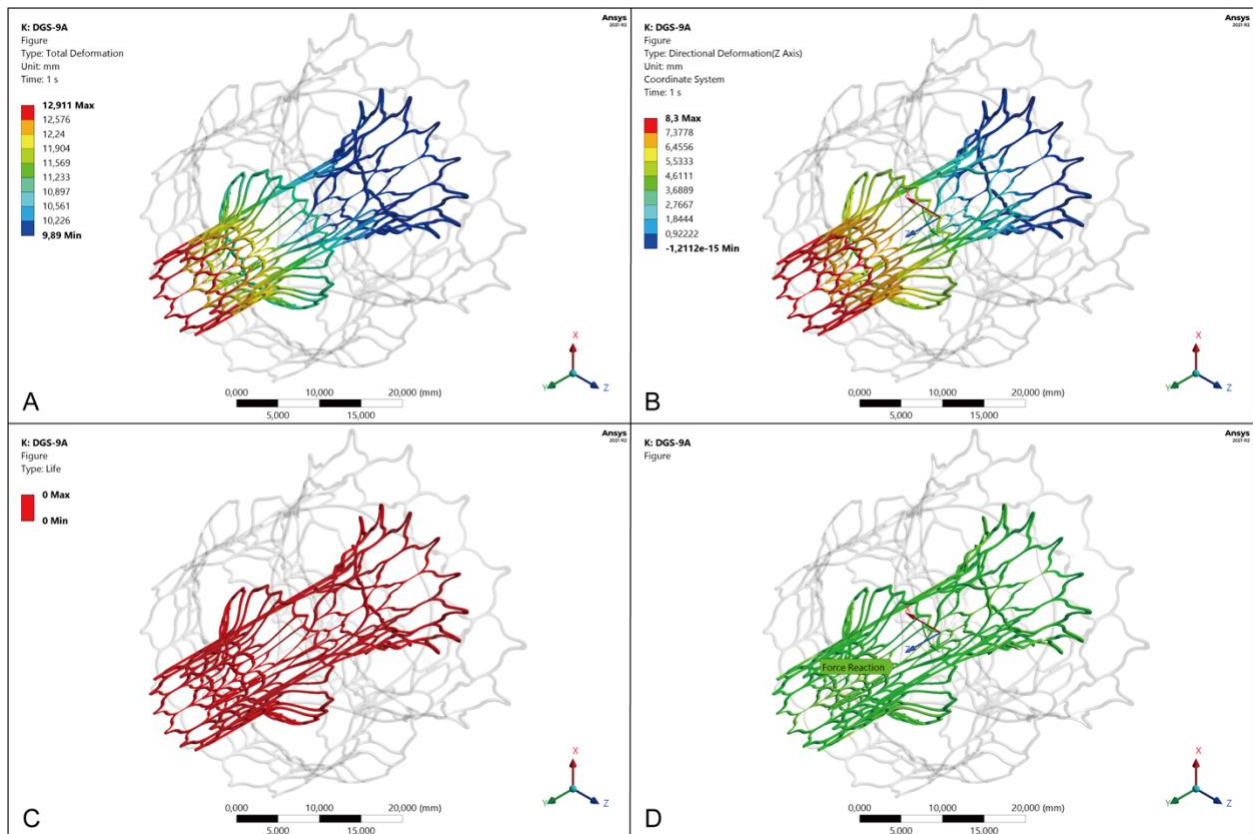


**Figure 44. Simulation of DGS-9A stent life and radial force**
**A:** Total deformation of DGS-9A; **B:** Directional deformation of DGS-9A, **C:** Maximum life of DGS-9A: 46093, **D:** Average radial force of DGS-9A: X axis:  3,6033 e+005 [N], Y axis: 6,2188 [N], Z axis: 6,8305e-006 [N], total: 3,6033 e+005 [N].

## ❖ Simulation of <u>DGS-10A</u> stent life, radial force, and hoop force

After model fault examinations and repairs in SpaceClaim, the DGS-10A mesh was generated using the Triangle method with 0.1 mm element size, 58717 nodes, and 90344 elements. DGS-10A was crimped to 13.434 mm on the X-axis and 5.1835mm on the Z-axis in the coordinate system to mimic the final crimping procedure at the head of the delivery system. After adding the displacements of total deformation and directional deformation while setting the analysis data, the DGS-10A life was obtained as Minimum: 0, Maximum: 46093, and Average: 1.7067. After preforming the total deformation and directional deformation, the radial force was obtained as: X-axis -2.278e+005 [N], Y-axis 20.99 [N], Z-axis 9.1749e-007 [N], total: 2.278e+005 [N] as shown in **Figure 45**.
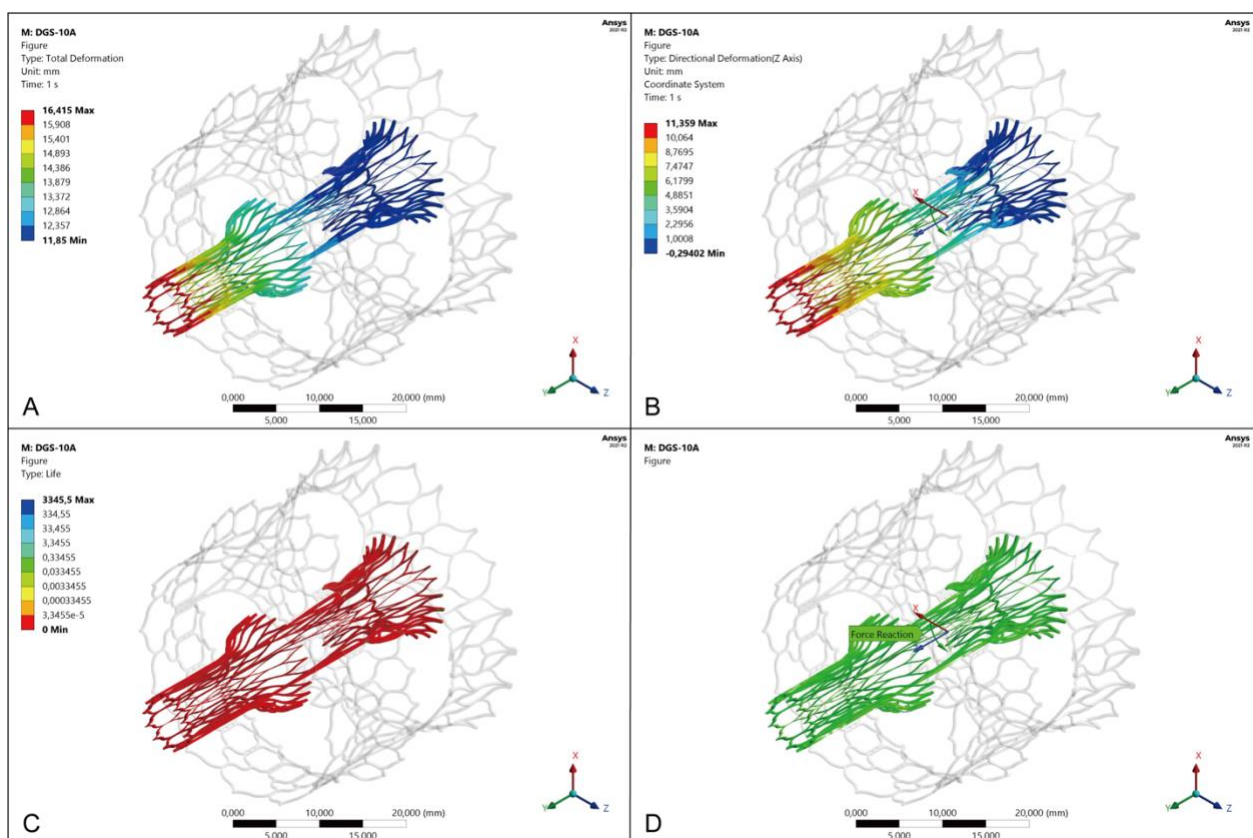


**Figure 45. Simulation of DGS-10A stent life and radial force**
**A:** Total deformation of DGS-10A; **B:** Directional deformation of DGS-10A, **C:** Maximum life of DGS-10A: 46093, **D:** Average radial force of DGS-10A: X axis 2.278e+005 [N], Y axis 20.99 [N], Z axis 9.1749e-007 [N], total: 2.278e+005 [N].

## ❖ Simulation of <u>DGS-12C</u> stent life, radial force, and hoop force

After model fault examinations and repairs in SpaceClaim, the DGS-12C mesh was generated using the Triangle method with default element size, 152811 nodes, and 67107 elements. DGS-12C was crimped to 11.684 mm on the X-axis and 4 mm on the Z-axis in the coordinate system to mimic the final crimping procedure at the head of the delivery system. After adding the displacements of total deformation and directional deformation while setting the analysis data, the DGS-12C life was obtained as Minimum: 0, Maximum: 2.4956e+005, and Average: 5.5056. After preforming the total deformation and directional deformation, the radial force was obtained as: X-axis: -1.9072e+005 [N], Y-axis: -5.1651 [N], Z-axis: -6.7032e-009 [N], total: 1.9072e+005 [N] as shown in **Figure 46**.
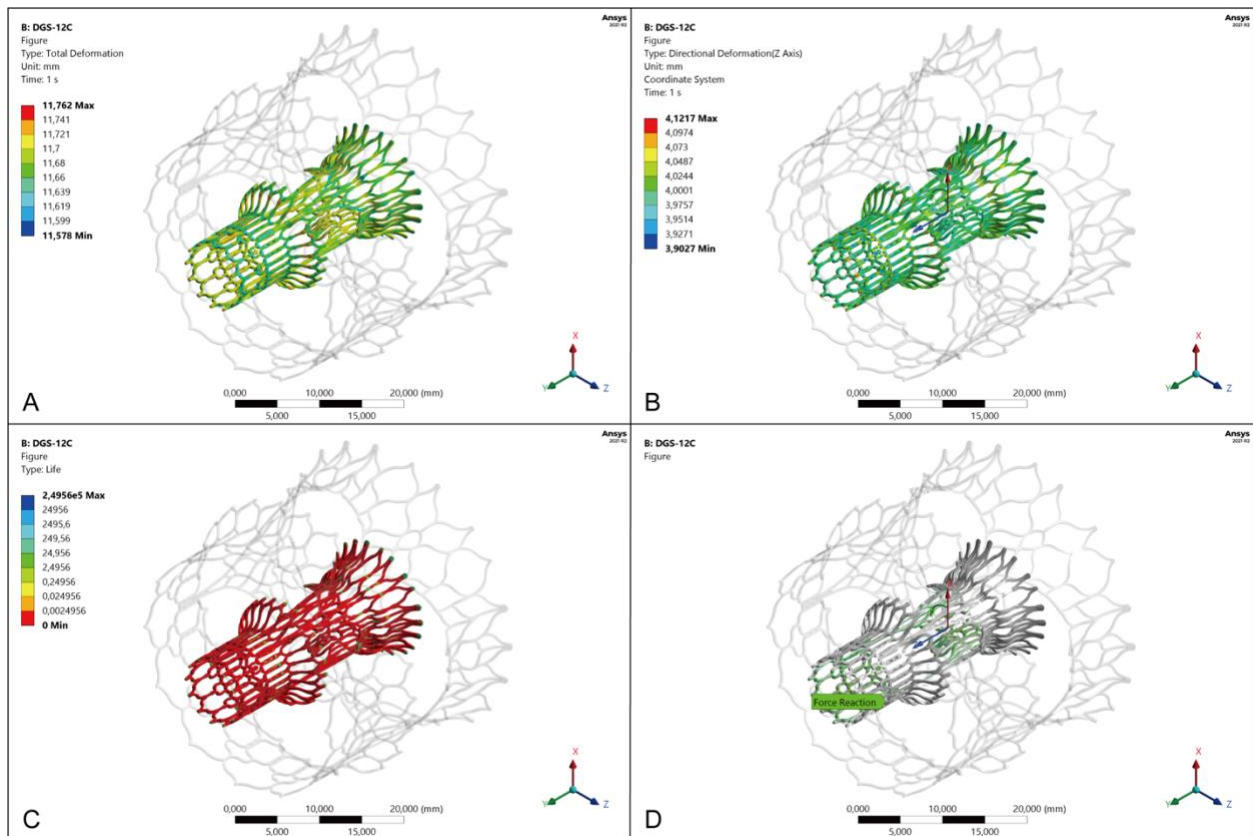


**Figure 46. Simulation of DGS-12C stent life and radial force**
**A:** Total deformation of DGS-12C; **B:** Directional deformation of DGS-12C, **C:** Maximum life of DGS-12C: 2.4956e+005, **D:** Average radial force of DGS-12C: 1.9072e+005 [N], Y axis: 5.1651 [N], Z axis: -6.7032e-009 [N], total: 1.9072e+005 [N].

### 3.5.3 Simulation of DGS stent life, radial force, and hoop force in Group 3

### ❖ Simulation of <u>DGS-12A and 12B</u> stent life, radial force

After model fault examinations and repairs in SpaceClaim, the DGS-12A mesh was then generated using the Triangle method with default element size, 144580 nodes, and 58116 elements. DGS-12A was crimped to 11 mm on the X-axis and 4 mm on the Z-axis in the coordinate system to mimic the final crimping procedure at the head of the delivery system. After adding the displacements of total deformation and directional deformation while setting the analysis data, the DGS-12A life was obtained as Minimum: 1e+006, Maximum: 1e+006, and Average: 1e+006. After preforming the total deformation and directional deformation, the radial force was obtained as: X-axis: -2.363e+008 [N], Y-axis -33161 [N], Z-axis -87.795 [N], total 2.363e+008 [N] as shown in **Figure 47**.
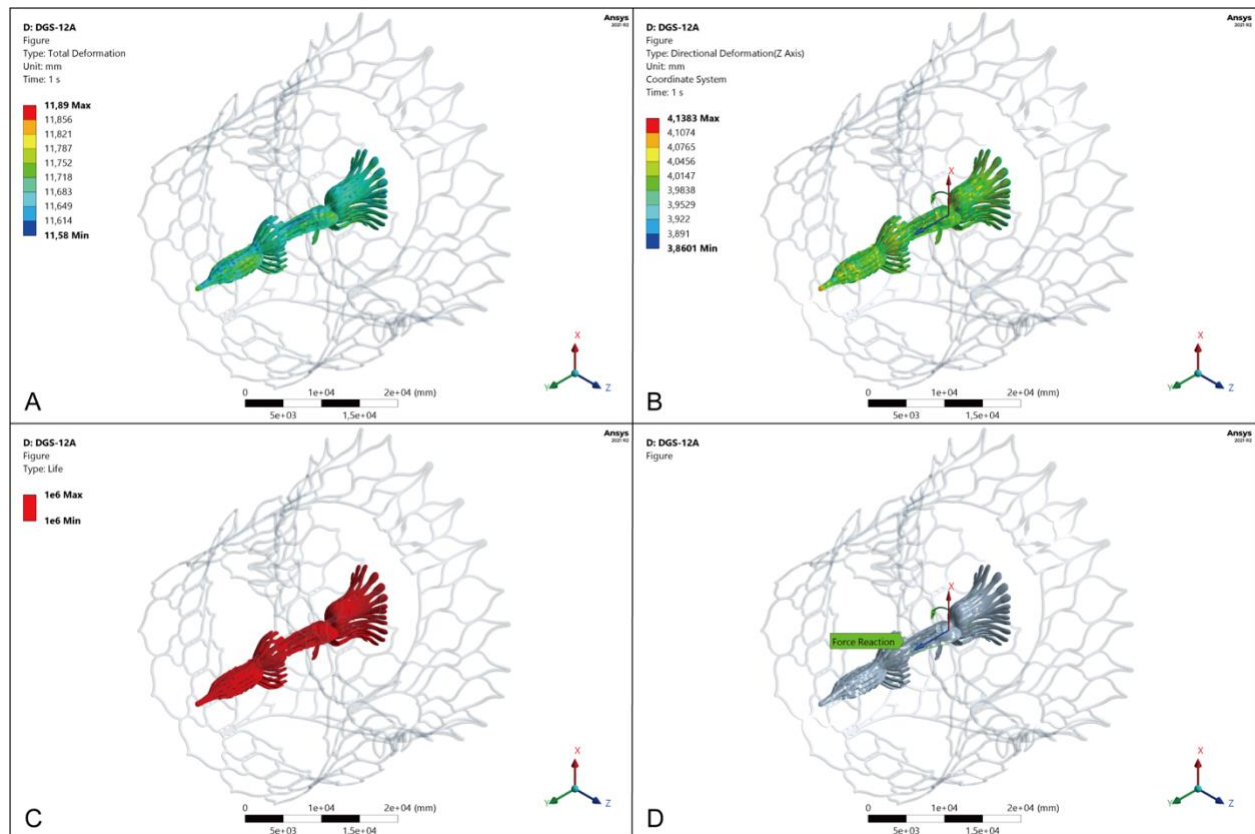


**Figure 47. Simulation of DGS-12A stent life and radial force.**
**A:** Total deformation of DGS-12A; **B:** Directional deformation of DGS-12A, **C:** Maximum life of DGS-12A: 1.00E+06, **D:** Average radial force of DGS-12A: X-axis: -2.363e+008 [N], Y-axis -33161 [N], Z-axis -87.795 [N], total 2.363e+008 [N].

After model fault examinations and repairs in SpaceClaim, the DGS-12B mesh was then generated using the Triangle method with default element size, 75223 nodes, and 118441 elements. DGS-12B was crimped to 11.373 mm on the X-axis and 4 mm on the Z-axis in the coordinate system to mimic the final crimping procedure at the head of the delivery system. After adding the displacements of total deformation and directional Minimum: 0, Maximum: 54509, and Average: 1,5791. After preforming the total deformation and directional deformation, the radial force was obtained as: X-axis -2.1989e+005 [N], Y-axis 34.374 [N], Z-axis 8.0838e-007 [N], total 2.1989e+005 [N] as shown in **Figure 48**.



**Figure 48. Simulation of DGS-12B stent life and radial force**
**A:** Total deformation of DGS-12B; **B:** Directional deformation of DGS-12B, **C:** Maximum life of DGS-12B: 54509, **D:** Average radial force of DGS-12B: X-axis -2.1989e+005 [N], Y-axis 34.374 [N], Z-axis 8.0838e-007 [N], total 2.1989e+005 [N].

### 3.6. Stents+ RVOT+PA simulation for the DGS stents' hoop force

### 3.6.1 Stents+ RVOT+PA simulation for the DGS stents' hoop force in Group 1

❖ **Simulation of <u>DGS-3</u> stent + RVOT+PA for the hoop force**

Due to the large crimped diameter, large profile, and short stent life, the DGS-3 was not imported into Ansys to pursue the calculation of the hoop force with the RVOT+PA 3D model.

❖ **Simulation of <u>DGS-5</u> stent + RVOT+PA for the hoop force**

The Triangle method was carried out to mesh DGS-5 and RVOT+PA with element size 0.1 mm for the stent (advanced defeature size 6.0107e-004 mm) and 1 mm for RVOT+PA (advanced defeature size 1 mm). DGS-5 was meshed into 56737 nodes with 90672 elements, while the RVOT+PA model was meshed into 4412 nodes with 8661 elements. After making contact with each other, total deformation action was added into the model along with the force reaction. After setting all the data, the average hoop force results were generated with a 1-second displacement time: X-axis: 57802 [N], Y-axis: 0.12076[N], Z-axis: 1.952e-002 [N], total: 57802 [N]; see **Figure 49**.
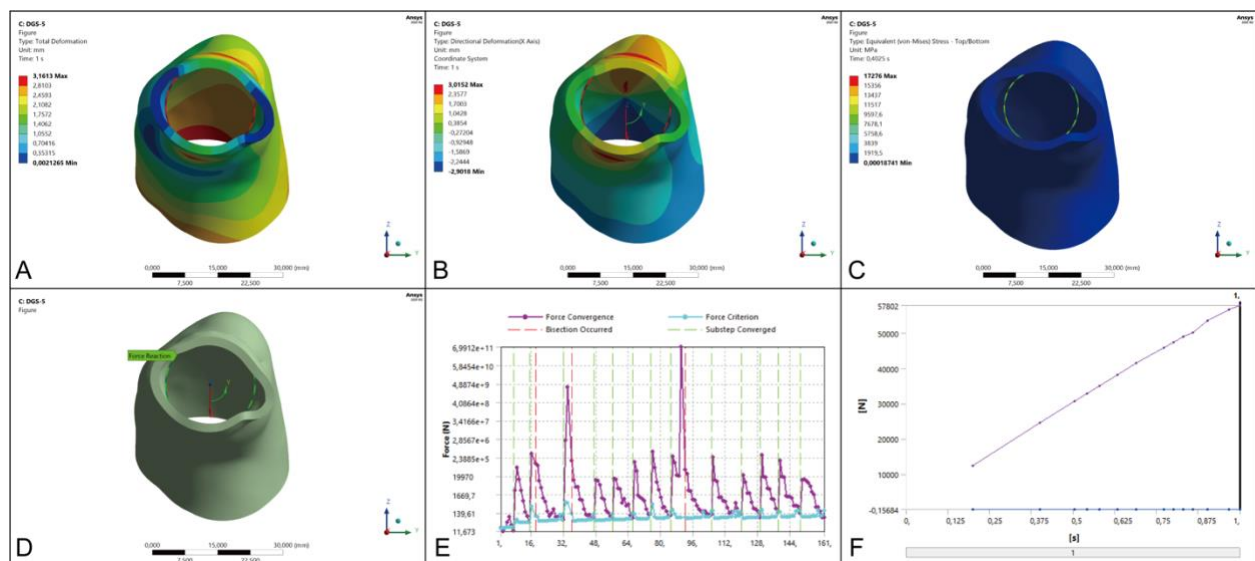


**Figure 49. Simulation of DGS-5 stent hoop force with RVOT+PA 3D model**
**A:** Total deformation of DGS-5 in RVOT+PA model after expansion, **B:** Directional deformation of DGS-5 in RVOT+PA model after expansion, **C:** Equivalent stress of DGS-5, **D-F:** Hoop force from 11649 [N] to 57802 [N] during the stent self-expandable attachment to the RVOT+PA.

❖ **Simulation of <u>DGS-7</u> stent + RVOT+PA for the hoop force**

The Triangle method was then performed to mesh DGS-7 and RVOT+PA with element size 0.1 mm for the stent (advanced defeature size 6.0107e-004 mm) and 1 mm for RVOT+PA (advanced defeature size 1 mm). DGS-7 was meshed into 50250 nodes with 79609 elements, while the RVOT+PA model was meshed into 4339 nodes with 8516 elements. After setting all the data, the average hoop force results were generated with a 1-second displacement time: X-axis: 54647 [N], Y-axis: 5.5695e-002 [N], Z-axis: -9.6831e-003 [N], total: 54647 [N]; see **Figure 50**.
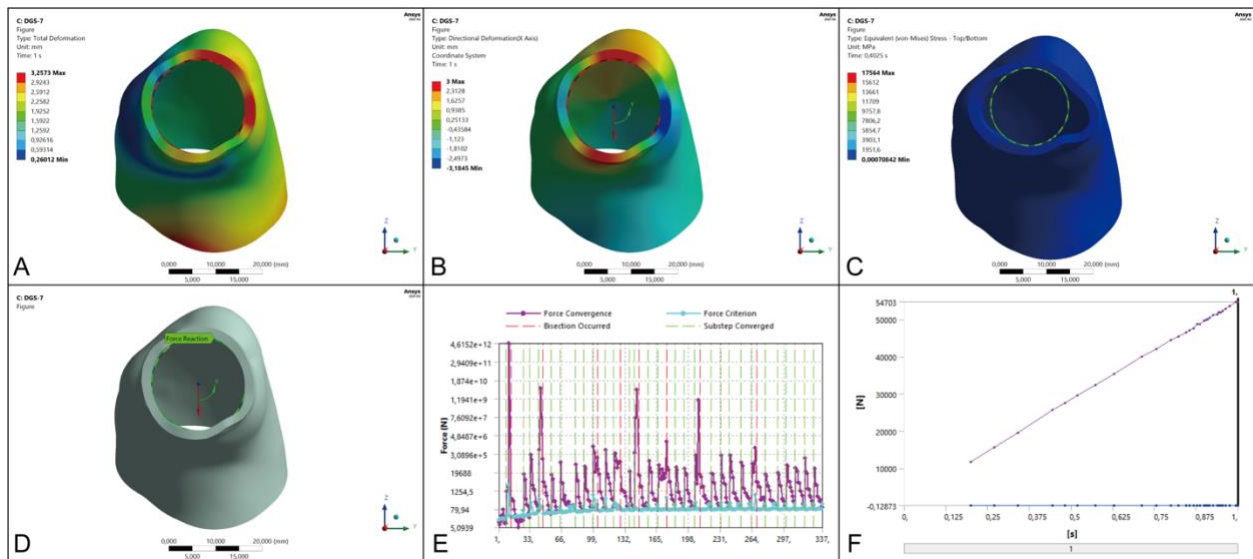


**Figure 50. Simulation of DGS-7 stent hoop force with RVOT+PA 3D model**
**A:** Total deformation of DGS-7 in RVOT+PA model after expansion, **B:** Directional deformation of DGS-7 in RVOT+PA model after expansion, **C:** Equivalent stress of DGS-7, **D-F:** Hoop force from 11649 [N] to 54703 [N] during the stent self-expandable attachment to the RVOT+PA.

❖ **Simulation of <u>DGS-8B</u> stent + RVOT+PA for the hoop force**

The Triangle method was carried out to mesh DGS-8B and RVOT+PA with element size 0.1 mm for the stent (advanced defeature size 6.0107e-004 mm) and 1 mm for RVOT+PA (advanced defeature size 1 mm). DGS-8B was meshed into 17605 nodes with 24280 elements, while the RVOT+PA model was meshed into 4339 nodes with 8516 elements. After setting all the data, the average hoop force results were generated with a 0.89466-second displacement time as: X-axis 53248 [N]; Y-axis: 0.17035 [N], Z-axis: -4.7569e-002 [N], total: 53248 [N]; see **Figure 51**.
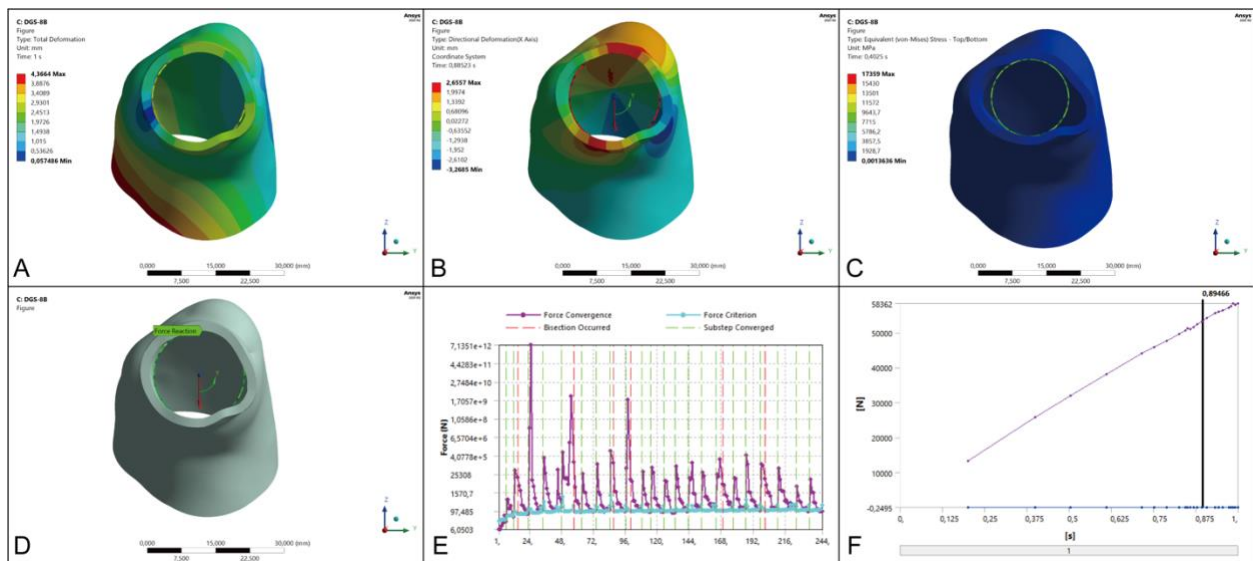


**Figure 51. Simulation of DGS-8B stent hoop force with RVOT+PA 3D model**
**A:** Total deformation of DGS-8B in RVOT+PA model after expansion, **B:** Directional deformation of DGS-8B in RVOT+PA model after expansion, **C:** Equivalent stress of DGS-8B, **D-F:** Hoop force from 13288 [N] to 53248 [N] during the stent self-expandable attachment to the RVOT+PA.

❖ **Simulation of <u>DGS-10B</u> stent + RVOT+PA for the hoop force**

The Triangle method was carried out to mesh DGS-10B and RVOT+PA with element size 0.1 mm for the stent (advanced defeature size 5, e-002 mm) and 1 mm for RVOT+PA (advanced defeature size 1 mm). DGS-10B was meshed into 19848 nodes with 27144 elements, while the RVOT+PA model was meshed into 4133 nodes with 8104 elements. After setting all the data, the average hoop force results were generated with a 1-second displacement time as: X-axis 56650 [N]; Y-axis: 0.22527 [N], Z-axis: -0.6212 N, total: 56650 [N]; see **Figure 52**.
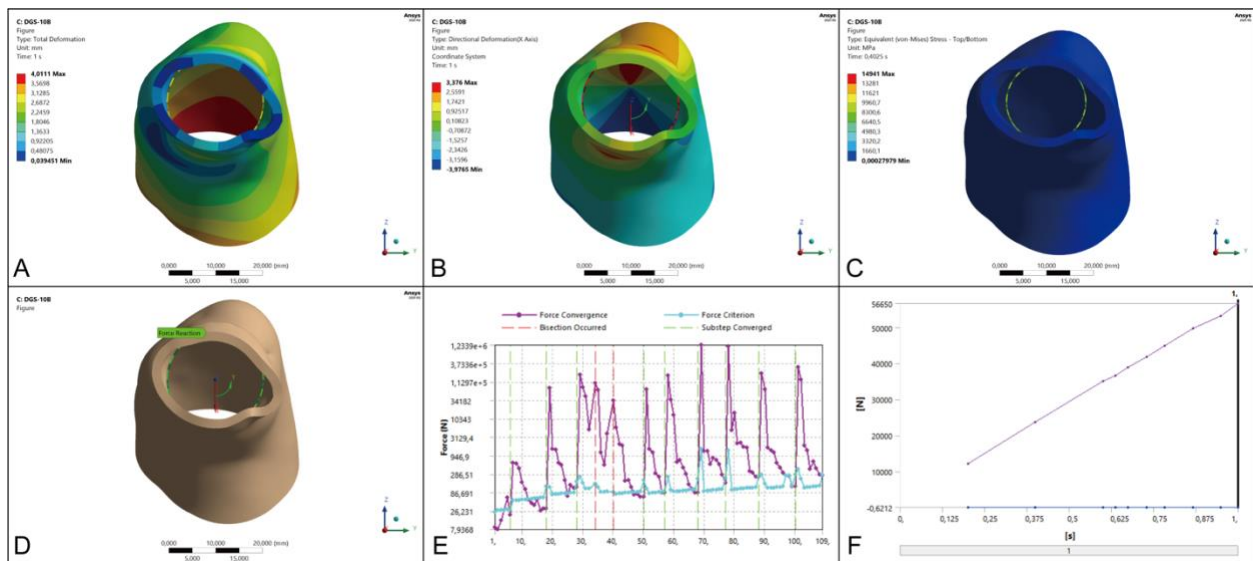


**Figure 52. Simulation of DGS-10B stent hoop force with RVOT+PA 3D model**
**A:** Total deformation of DGS-10B in RVOT+PA model after expansion, **B:** Directional deformation of DGS-10B in RVOT+PA model after expansion, **C:** Equivalent stress of DGS-10B, **D-F:** Hoop force from 5801.4 [N] to 16368 [N] during the stent self-expandable attachment to the RVOT+PA.

### ❖ Simulation of <u>DGS-12D</u> stent + RVOT+PA for the hoop force

The Triangle method was carried out to mesh DGS-12D with 19575 nodes and 26614 elements, while 4133 nodes and 8104 elements were used for RVOT+PA meshing. After making contact with each other, the total deformation action was added into the model, along with the force reaction. After setting all the data, the average hoop force results were generated with a 0.89466-second displacement time as: X-axis: 46297 [N]; Y-axis: -2.7464e-002 [N], Z-axis: -6.5259e-002 [N], total: 46297 [N]; see **Figure 53**.
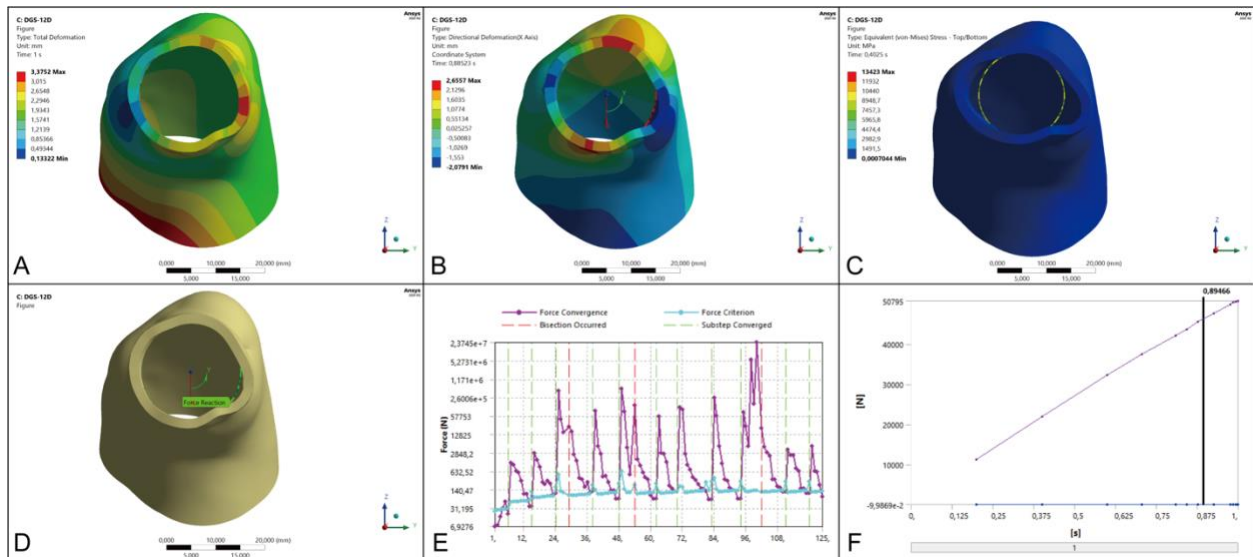


**Figure 53. Simulation of DGS-12D stent hoop force with RVOT+PA 3D model.**
**A:** Total deformation of DGS-12D in RVOT+PA model after expansion, **B:** Directional deformation of DGS-12D in RVOT+PA model after expansion, **C:** Equivalent stress of DGS-12D, **D-F:** Hoop force from 11210 [N] to 50795 [N] during the stent self-expandable attachment to the RVOT+PA.

### 3.6.2  Stents+ RVOT+PA simulation for the DGS stents' hoop force in Group 2

❖  **Simulation of <u>DGS-8A</u> stent + RVOT+PA for the hoop force**

The Triangle method was then carried out to mesh DGS-8A and RVOT+PA with element size 5.e-002 mm for the stent (advanced defeature size 6.0107e-004 mm) and 1 mm for RVOT+PA (advanced defeature size 1 mm). DGS-8A was then meshed into 82088 nodes with 137847 elements, while the RVOT+PA model was meshed into 2111 nodes with 4108 elements. After contacting each other, total deformation action was added into the model along with the force reaction. The average hoop force results were generated with a 1-second displacement time as follows: Maximum Value Over Time: X-axis: 49334 [N]; Y-axis: -68.57 [N], Z-axis: -10746 [N], total: 50490 [N]; see **Figure 54**.
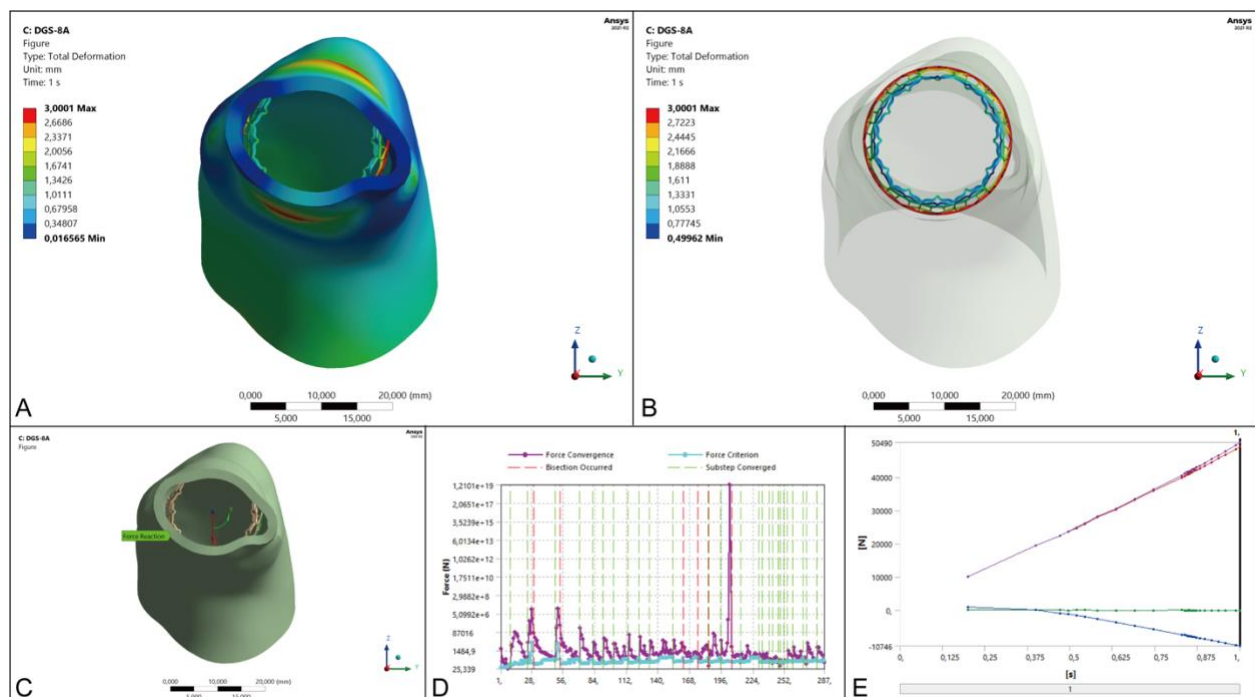


**Figure 54. Simulation of DGS-8A stent hoop force with RVOT+PA 3D model**
**A and B:** Total deformation of DGS-8A in RVOT+PA model after expansion, **C-E:** Hoop force from 10104 [N] to 50490 [N] during the stent self-expandable attachment to the RVOT+PA.

## ❖ Simulation of <u>DGS-9A</u> stent + RVOT+PA for the hoop force

The Triangle method was carried out to mesh DGS-9A and RVOT+PA with element size 0.1 mm for the stent (advanced defeature size 6.1194e-004 mm) and 1 mm for RVOT+PA (advanced defeature size 1 mm). DGS-9A was meshed into 41814 nodes with 66770 elements, while the RVOT+PA model was meshed into 2102 nodes with 4091 elements. After contacting each other, total deformation action was added into the model, along with the force reaction. After setting all the data, the average hoop force results were generated with a 1-second displacement time as follows: X-axis: 60389 [N], Y-axis: -16.652 [N], Z-axis: -667.57 [N], total: 60393 [N]; see **Figure 55**.
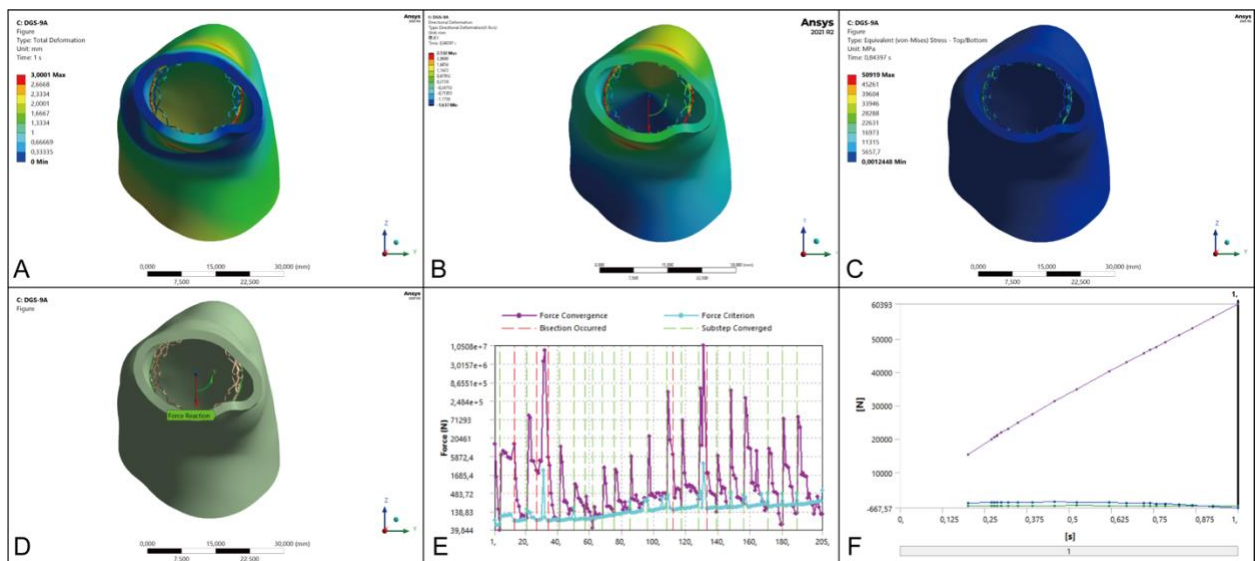


**Figure 55. Simulation of DGS-9A stent hoop force with RVOT+PA 3D model**
**A:** Total deformation of DGS-9A in RVOT+PA model after expansion, **B:** Directional deformation of DGS-9A in RVOT+PA model after expansion, **C:** Equivalent stress of DGS-9A, **D-F:** Hoop force from 15340 [N] to 60393 [N] during the stent self-expandable attachment to the RVOT+PA.

❖ **Simulation of <u>DGS-10A</u> stent + RVOT+PA for the hoop force**

The Triangle method was carried out to mesh DGS-10A and RVOT+PA with element size 0.1 mm for the stent (advanced defeature size 5, e-002 mm) and 1 mm for RVOT+PA (advanced defeature size 1 mm). DGS-10A was meshed into 20441 nodes with 27744 elements, while the RVOT+PA model was meshed into 2110 nodes with 4106 elements. After making contact with each other, total deformation action was added into the model, along with the force reaction. After setting all the data, the average hoop force results were generated with a 1-second displacement time as: X-axis: 23639 [N]; Y-axis: -0.10977 [N], Z-axis: 0.29715 [N], total 23639 [N]; see **Figure 56**.
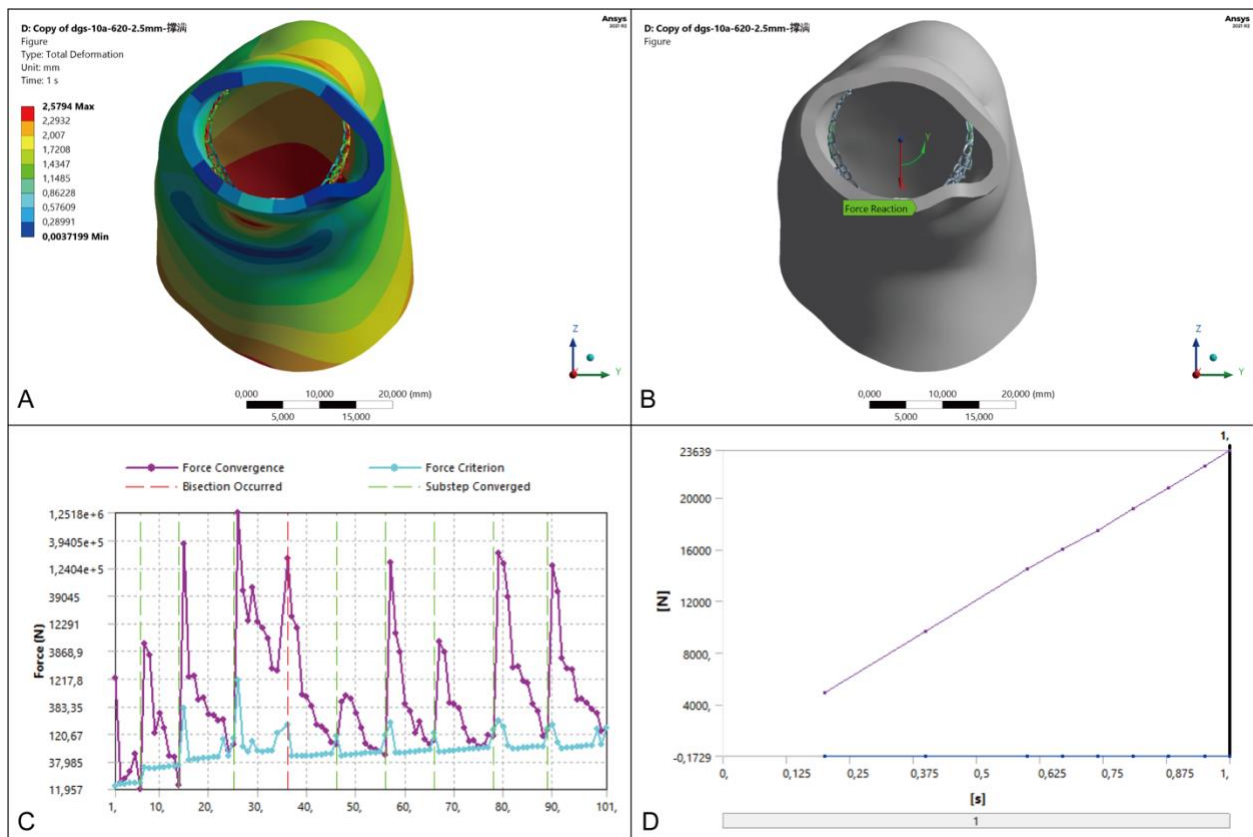


**Figure 56. Simulation of DGS-10A stent hoop force with RVOT+PA 3D model**
**A:** Total deformation of DGS-10A in RVOT+PA model after expansion, **B-D:** Hoop force from 4913.5 [N] to 23639 [N] during the stent self-expandable attachment to the RVOT+PA.

## ❖ Simulation of <u>DGS-12C</u> stent + RVOT+PA for the hoop force

The Triangle method was carried out to mesh DGS 12C and RVOT+PA with default element size 0.11945 mm for the stent (advanced defeature size 5, e-002 mm) and1 mm for RVOT+PA (advanced defeature size 1 mm). After making contact with each other, total deformation action was added into the model, along with the force reaction. After setting all the data, the average hoop force results were generated with a0.72 second displacement time as: X axis: 29762 [N]; Y axis:  6.3998 [N], Z axis:  1548.2 [N], total: 29802 [N]; see **Figure 57**.
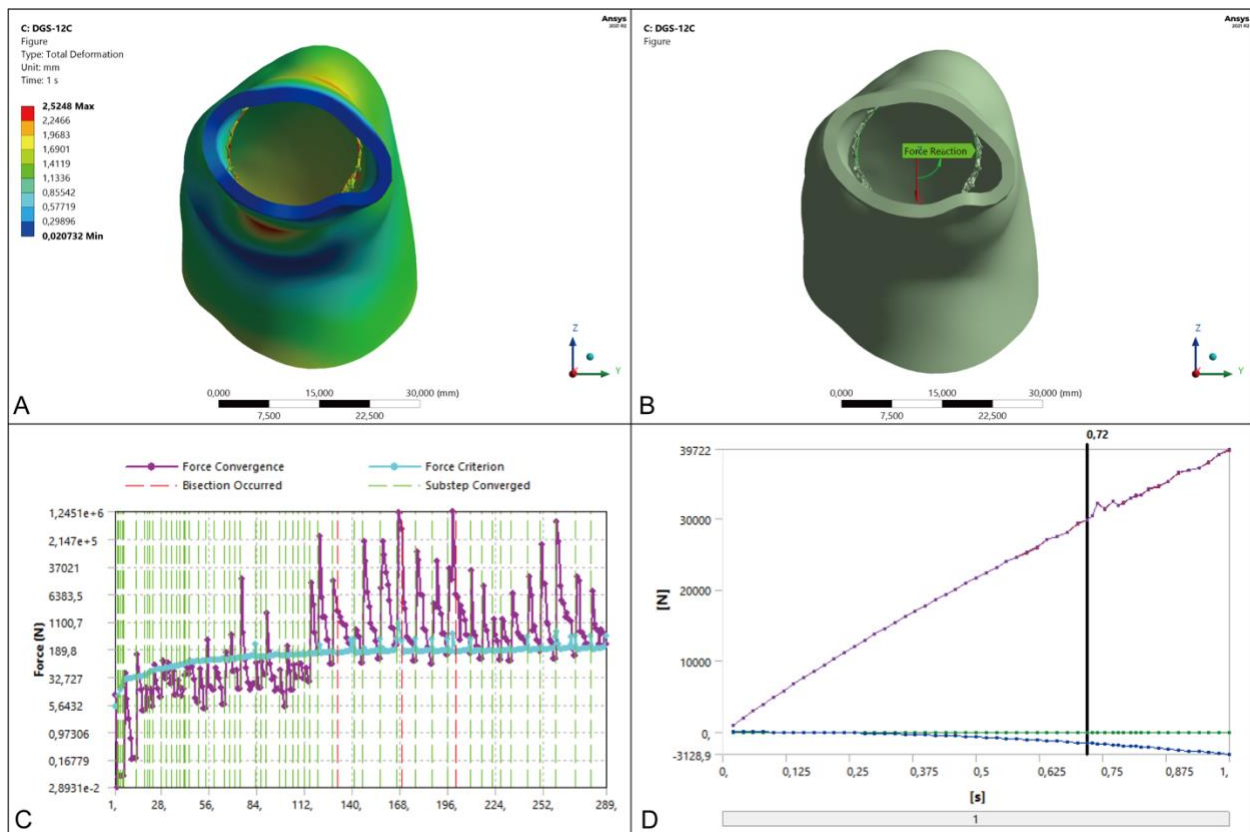


**Figure 57. Simulation of DGS-12C stent hoop force with RVOT+PA 3D model**
**A:** Total deformation of DGS-12C in RVOT+PA model after expansion, **B-D:** Hoop force from 1002.6 [N] to 39722 [N] during the stent self-expandable attachment to the RVOT+PA.

### 3.6.3 Stents+ RVOT+PA simulation for the DGS stents' hoop force in Group 3

### ❖ Simulation of <u>DGS-12A</u> and <u>DGS-12B</u> stents + RVOT+PA for the hoop force

After model fault examinations and repairs in SpaceClaim, the DGS-12B mesh was then generated using the Triangle method with default element size, 75223 nodes, and 118441 elements. DGS-12B was crimped to 11.373 mm on the X-axis and 4 mm on the Z-axis in the coordinate system to mimic the final crimping procedure at the head of the delivery system. After adding the displacements of total deformation and directional Minimum: 0, Maximum: 54509, and Average: 1,5791. After preforming the total deformation and directional deformation, the radial force was obtained as: X-axis -2.1989e+005 [N], Y-axis 34.374 [N], Z-axis 8.0838e-007 [N], total 2.1989e+005 [N] as shown in **Figure 58**.



**Figure 58. Simulation of DGS-12B stent hoop force with RVOT+PA 3D model**
**A:** Total deformation of DGS-12B in RVOT+PA model after expansion, **B-D:** Hoop force from 5801.4 [N] to 16368 [N] during the stent self-expandable attachment to the RVOT+PA.

**Table 1. Parameters, life, radial force, hoop force of DGS stents**

| | | Expandable diameter (mm) | Expandable height (mm) | Crimped diameter (mm) | Crimped height (mm) | Life of DGS stents | Radial force of DGS stents | Hoop force of DGS stents [N] | | |
|---|---|---|---|---|---|---|---|---|---|---|
| | | | | | | | | MAX | MIN | Average |
| **Group 1** | DGS-3 | 30 | 40.4 | 10.3 | 44.4 | 3219.2 | 1.88E+05 | - | - | - |
| | DGS-5 | 30 | 35.8 | 7.6 | 41.2 | 16406 | 1.94E+05 | 57802 | 11649 | 57802 |
| | DGS-7 | 30 | 36.1 | 6.0 | 40.3 | 1.00E+06 | 1.89E+05 | 54703 | 11649 | 54647 |
| | DGS-8B | 30 | 31.7 | 10.3 | 40.0 | 0 | 3.74E+05 | 58362 | 13288 | 53248 |
| | DGS-10B | 30 | 31.1 | 7.0 | 38.7 | 8370.1 | 2.41E+05 | 56650 | 12150 | 56650 |
| | DGS-12D | 30 | 28.9 | 7.2 | 37.2 | 1.00E+06 | 2.41E+08 | 50795 | 11210 | 46297 |
| **Group 2** | DGS-8A | 30 | 30.9 | 10.4 | 40.0 | 0 | 3.60E+05 | 50490 | 10104 | 50490 |
| | DGS-9A | 30 | 30.3 | 10.3 | 39.7 | 0 | 3.60E+05 | 60393 | 15340 | 60393 |
| | DGS-10A | 30 | 31.4 | 7.1 | 39.1 | 46093 | 2.28E+05 | 23639 | 4913.5 | 23639 |
| | DGS-12C | 30 | 28.9 | 7.2 | 37.2 | 2.50E+005 | 1.91E+05 | 39722 | 1002.6 | 29802 |
| **Group 3** | DGS-12A | 30-36 | 31.4 | 7.9-9.5 | 41.0 | 1.00E+06 | 2.36E+08 | 16368 | 5.80E+03 | 16368 |
| | DGS-12B | 36-30 | 31.4 | 9.5-7.9 | 41.0 | 54509 | 2.20E+05 | 16368 | 5.80E+03 | 16368 |

## 4. Discussion

In the present study, 12 functional stent prototypes, radial force and lives with Nitinol and self-expandable features were successfully generated in Autodesk Fusion 360 and Ansys 2021 R2. Furthermore, the hoop force of eleven stents was obtained with the RVOT+PA model after being computed in 3D Slicer. In line with previous studies on the descriptions and specifications of TAVI and TPVR devices currently available on the medical market (41, 73-78), we found that DGS-5, DGS-7, DGS-10B and DGS-12D in Group 1, as well as DGS-10A and DGS-12C in Group 2 can be further tested in vitro due to their long stent lives, proper radial force, and large hoop force, and could then be available for transcatheter autologous pulmonary valve replacement in future large animal studies, or even in clinical application. However, the oval stents DGS-12A and DGS-12B in Group 3 need to be redesigned to optimize the geometries in order to achieve the ideal radial force, life, and hoop force. However, current issues in regard to TPVR, such as stent and RVOT fracture, stented heart valve migration, and coronary occlusion should be addressed to achieve better clinical outcomes. Furthermore, due to the increasing number of patients suffering from valvular diseases including dysfunctional RVOT, numerous stents for transcatheter heart valve treatments are being improved to adapt to various RVOT anatomies, suggesting that a "one-size-fits-all" self-expandable stent as a carrier is needed to design a 3D shape autologous heart valve in order to determine anatomical and clinical issues.

### 4.1. Animal 3D cardiac CT reconstructions in 3D Slicer

Technological developments in 3-dimensional (3D) -CTA have opened the door to the novel way in personalized planning of transcatheter heart valve implantation for patients with structural heart valve diseases (79-81). Cross-sectional imaging with 3D C-CTA is critical to reveal the suitability for TPVR: comprehension of RVOT anatomy, the proximity of the left coronary artery to the native pulmonary root, and distensibility of RVOT are needed pre-requisites for TPVR (82, 83). In addition to this, 3D C-CTA can predict the indication of candidate percutaneous access routes, including the transfemoral, trans jugular, and subclavian routes, and answer any key anatomical questions. Furthermore, the landing zone— the ideal implantation site for TPVR— is a conduit to guarantee the protection of the stented pulmonary valve free from PVL, migration, and coronary compression. To create an accurate 3D segmentation of landing zone anatomy at RVOT, CT datasets should undergo segmentation, wherein the personalized CT data is assigned to a region of interest to generate the 3D structures. To demonstrate the cardiac

architecture, including the four heart chambers and great vessels, 3D reconstructions of the cardiac anatomy were performed on all animal cardiac CT scans. The right ventricle and main pulmonary artery in 3D models were trimmed to provide a landing zone for the DGS stents in order to do the hoop force simulation.

## 4.2. Functional stent designs in Fusion 360

### 4.2.1 Design principles for TPVR devices

#### 4.2.1.1. Comprehensive components of functional stents for TPVR

TPVR devices should be equipped with numerous comprehensive components. Specifically, they should be suitable for a wide range of annulus sizes, different pulmonary valve pathologies, ensure long-term durability, minimal paravalvular leak, optimal effective orifice area, minimal vascular access size, easy coronary access or freedom from occlusion, consistent commissural alignment, use in patients with low EF (e.g., no need for rapid pacing), have a low risk of permanent pacemaker implantation and/or new permanent conduction abnormalities, confer a minimal need for using contrast media, be repositionable and retrievable, and have an easy-to-use delivery system.

Although most patients with aortic valve diseases and dysfunctional RV-to-PA conduits or a patched RVOT are suitable for stented valve types that are currently available on the market, certain scenarios may slightly favor one particular design. It may also not be possible to find an appropriate device for patients with pulmonary artery root dilation.

#### 4.2.1.2. A "one-size-fits-all" functional stent

A "one-fits-all" functional stent, which would be used to mount an autologous pulmonary valve in place for transcatheter implantation, should be equipped with additional capabilities in order to accommodate different RVOT anatomies. To optimize transcatheter application, the ideal stent should have the following features:

❖ Ideal radial force, which constitutes having enough strength to resist the rebound force of the vessel after full expansion.

❖ Capacity for expansion, i.e., be evenly expandable to the required diameter.

❖ Biocompatibility, i.e., a strong anti-blood corrosion ability without the occurrence of thrombosis.

❖ Flexibility to accurately reach the right position through various vascular anatomies.

❖ Ideal tracer, which should make it easy to track the position of the stent for accurate positioning during angiography.

❖ Low risk of damage to the vascular wall, i.e., the reduction of intimal hyperplasia and in-stent restenosis following implantation, retrieval, and repositioning.

❖ Long stent life, making this a once-in-a-lifetime opportunity.

❖ Low crimped profile for easy delivery; low axial shortening, which can be convenient for accurate release and positioning.

❖ High-cost performance, which can be affordable for patients and healthcare providers worldwide.

In view of the above "ideal standards" for the design of a pulmonary valve stent, an "one-fits-all" autologous pulmonary valve stent for interventional application should be designed in the hope of mounting a flawless autologous pulmonary valve for both adults and children. Additionally, a stent for interventional heart valve implantation should also be equipped with serviceable functions. For instance, it should be possible to mount the new autologous pulmonary valve with its original architecture, offer easy real-time suturing prior to implantation, possess an ideal anchoring ability without stented pulmonary valve migration during the whole cardiac cycle, provide ample opening space for the new heart valve, and be free from interference of diseased tissue (calcification, hyperplasia, etc.) as well as the normal architectures of the heart (conduction bundles, coronary arteries, etc.).

### 4.2.2 Functional features of DGS stents

### 4.2.2.1. The concept of a functional "one-fits-all" stent for TPVR

A stent for TPVR should not only be used to mount an autologous pulmonary valve for real-time application, but should also have with the desired radial and hoop force, possess a durable stent life, have a large opening space for the heart valve, provide an appropriate combination with the RVOT anatomy, have easy suturing availability to retain an autologous heart valve, have a low profile, possess benign blood flow conduction, stable metallic characteristics, adopt an invigorative anchoring configuration and an attractive architectural design.

### 4.2.2.2. The methodology of the stent design

The methodology of the stent design in this study followed the concept outlined above. To recap, the designs of the twelve DGS stents can be divided into three different types according to their architectures: vertical stents (DGS-3, DGS-5, DGS7, DGS-8B, DGS-10B, DGS-12D), cylindrical stents with outstretched crowns (DGS-8A, DGS-9A, DGS-10A DGS-12C), and transitional oval stents with outstretched crowns (DGS-12A and DGS-12B).

### 4.2.2.3. Vertical stents

The DGS-3 and DGS-5 stents were designed with three functional segments: A top crown with V-shaped struts for PA anchoring, new leaflet loading zones with two specific suture lines at the commissural horizontal and fixation points for the edges of the new leaflets, and a bottom crown for RVOT anchoring. The top crowns of these two stents help the stented autologous heart valve to anchor inside the annulus at the main pulmonary artery, while the bottom crowns help the heart valve to properly anchor at the RVOT. The main functional segment of these two stents is the new leaflet loading zones with two specific suture lines at the commissural horizontal and fixation points for the edges of the new leaflets. Moreover, various potential suture points (DGS-3: 17, DGS-5: 16) enable the surgeon to perform extra fixations for the new leaflets. However, due to the large, crimped profile (44.4 mm) and diameter (10.3 mm) of DGS-3, it is unsuitable for transcatheter interventions, especially in children. Furthermore, it may be troublesome to deploy DGS-3 in the aortic valve position for coronary catheterization. Accordingly, DGS-5 is suitable for pulmonary valves due to its large open-cell design in the middle segment as well as its low crimped profile (41.2 mm) and smaller crimped diameter (7.6 mm), which can be loaded in the 24Fr head of a delivery system for deployment. Furthermore, DGS-3 and DGS-5 both possess capabilities for repositioning or retrieval.

DGS-7 and DGS-8B share a similar design and have four functional segments: A top lotus crown for pulmonary artery anchoring, a middle crown for native leaflet compression and two suture lines at the commissural horizontal, symmetrical support architectures for suturing new leaflets, and a basal crown for RVOT anchoring. DGS-8B and DGS-9B have larger open-cell top and bottom crowns compared to those of DGS-7. In addition, DGS-8B and DGS-9B have equal distances at the top two suture lines (commissural horizontals), which help surgeons in real time while sewing stented heart valves due to the fixed suture holes. Meanwhile, the new heart valve can be sutured onto the Y-shaped struts of DGS-7 with two suture lines. These three stents have nine approximately equal suture distances aligned to the edges of each leaflet along with similar struts to compress the native pulmonary valve against the artery wall or the tissues aligned at the annular zones in order to provide the new heart valve with large opening orifices. Hooks at the bottom crowns of these three stents are also available for stented heart valve repositioning. The space between the compression struts and the basal segment of the new leaflet can facilitate coronary catheterization; hence, these three stents are suitable for TPVR. DGS-7 has a smaller crimped diameter (6 mm) and larger profile (40.3 mm crimped

height) compared to DGS-8B (10.3 mm crimped diameter and 40 mm crimped height) which can be deployed using 18Fr and 32Fr delivery systems.

DGS-10B and DGS-12D have the same crown at the top in conjunction with the middle segments for PA anchoring and native heart valve compression. In addition, they have two suture lines at the commissural horizontal with equal suturing distances. These two segments have large and symmetrical open cells that can help the stented heart valve attain better blood flow conduction and maintain a stable hoop force during the whole cardiac cycle. Segment III of these two stents was designed with approximate determinate suture points (17 points) (2.7 mm to 3.1 mm) for leaflet hosting as well as a strong asymmetrical support frame with retrieving struts for stent repositioning. Furthermore, they all have hook-connect points below the three commissures at the second suture point connection between the two leaflet junctions. The difference in this segment between DGS-10B and DGS-12D is that DGS-10B does not have guard arms at the bottom to protect the new leaflets. Between the middle crown and the basal parts of segment III, these two stents offer ample space for coronary catheterization, making these two stents suitable for TPVR. Furthermore, they can provide valve-in-valve opportunities for patients with bioprosthetic valve degradation who are scheduled to undergo interventional heart valve implantation or who experience stented pulmonary valve dysfunction during implantation. Segment IV of these two stents have similar struts for RVOT anchoring. Additionally, DGS-12D has both a lower expanded profile (expanded height: 28.9 mm) compared to DGS-10B (31.1 mm) and crimped height (37.2 mm vs. 38.7 mm), while the crimped diameter is larger (7.23 mm vs. 7 mm). Accordingly, they can all be deployed using a 22Fr delivery system.

### 4.2.2.4. Cylindrical stents with outstretched crowns

DGS-8A has the same design concept as DGS-9A. This concept includes segment II for native heart valve compression and equal suturing distances at the two suture lines aligned at the commissural horizontal, segment III for new pulmonary valve suturing with strong symmetrical support structures and hooks for heart valve repositioning, and a basal crown for RVOT anchoring. The difference between DGS-8A and DGS-9A is the design philosophy of the top lotus crown. The top crown of DGS-8A was designed to be 34 mm in diameter and 2 mm offset from the core segment hosting the 30-mm diameter new pulmonary valve for more extensive dilation of the PA. Furthermore, the top of this crown features tiny-outstretched arms at the distal end of the cells with a 0.2-mm offset from the top crown. This design was meant to improve anchoring at the PA and prevent

stented pulmonary valve migration during the whole cardiac cycle. However, these tiny-outstretched arms may risk damaging the endangium, which may cause great vessel dissection, especially in calcific aortas in elderly patients. DGS-8A can be fully crimped in a crimping tool to 40 mm in height and 10.4 mm in diameter and can be loaded at the head of a 32Fr delivery system. DGS-9A, on the other hand, is 10.3 mm in diameter and 39.7 mm in height when crimped. Due to their large, crimped profiles, they are unsuitable for preclinical testing unless further improvements are made.

Both DGS-10A and DGS-12C have similar top corollaceous crown struts, with 12 stabilized cells that can provide better coaxial alignment and are beneficial for anchoring at the main pulmonary artery trunk. Furthermore, segment II of these two stents has the same function, including two suture lines at the commissural horizontal for heart valve fixation and three outstretched arms to guard the leaflets and compress the native leaflets. With these outstretched arms, the whole prosthesis offers ample space for the new autologous pulmonary valve with or without Valsalva sinuses, can rid itself of calcific tissue, maintain the desired geometry of the new autologous pulmonary valve, as well as prevent paravalvular leak and stented heart valve migration from its ideal position despite blood stress during the filling phase of the cardiac cycle. The difference in this segment between DGS-10A and DGS-12C is that the latter has three outstretched guard arms at the bottom that serve not only to protect the new leaflets, but also to prevent paravalvular leak and stented autologous pulmonary valve migration. Between the middle crown and the basal parts of segment III, these two stents offer ample space for coronary catheterization, signifying that these two stents may be suitable for TaPVR. They also have the same 17 sewing points at each leaflet frame at approximate equal distances, offering surgeons determinate suture points during the surgery for running or interrupted sutures. Stented autologous pulmonary valves with DGS-10A and DGS-12C can also be repositioned at the middle crown level with the help of a hook-connect point at the second suture point connection between the two leaflet junctions below the three commissures. The large space between the outstretched arms at segment II and the basal part of the leaflets means that patients can undergo coronary catheterization while freeing them from coronary occlusion in TPVR. In segment IV for RVOT anchoring, DGS-10A and DGS-12C have two slick secure layers to help the stented autologous pulmonary valve adhere at the RVOT without interrupting cardiac conduction bundles and other cardiac structures. These two secure architectures can also help the stented heart valve to avoid migration to the artery and prevent paravalvular leak at the RVOT level. DGS-12 has three

safeguarding architectures: the outstretched guard arms at segment II and segment III, as well as two secure layers in segment IV to address device-related paravalvular leak, device migration, coronary occlusion, and inadaptation in various anatomies. However, DGS-10A has only two safeguarding architectures. With these secure struts, it can be assumed that these two stents may be applied without the need for adopting an oversize strategy during the pre-implantation evaluation. Accordingly, a 30-mm diameter DGS-10A or DGS-12C may be applied in a patient with a 30-mm annulus diameter instead of being 10-20% oversized. DGS-12C has a lower expanded height (28.9 mm) compared to that of DGS-10A (31.4 mm), as well as a lower crimped height (37.2 mm vs. 39.1 mm); however, the crimped diameter is larger (7.23 mm vs. 7.1 mm). They can all be delivered using a 22Fr delivery system.

### 4.2.2.5. Functional stents for an oval autologous pulmonary valve

DGS-12A and DGS-12B were designed to fit the RVOT and PA anatomy, which means an oval shape in the RVOT and an approximate circular shape in the PA (84-86). They possess the same functional architectures as DGS-12C, except for their transitional circular-to-oval geometry. The aim of DGS-12A and DGS-12B is to load a tricuspid valve; however, the heart valve attachment at the three commissures in an oval stent should be two-style owing to the asymmetrical nature of the ovality. Therefore, the difference between DGS-12A and DGS-12B is the position of one of the commissures sutured into the stent at the long axis or the short axis of the ovality. In this study, the distal segment (34 mm in diameter) of the top crown was designed with a circular architecture according to the PA anatomy, while the proximal segment of the top corollaceous crown was oval (30 mm: 36 mm) and had a ratio of 1:1.2, transitioning gradually from the circular segment to ovality. The general shape of segments II, III, and IV was oval and had the same functions as DGS-12C (see above). These two stents may also be applied in a patient without an oversize strategy due to the three outstretched guard arms for each leaflet and the oval geometry. With this oval design, these two stents can adhere to the endangium and may help prevent PVL, migration, coronary occlusion while maintaining the ideal function of the 3D shaping heart valve.

### 4.3. RVOT+PA blood flow and shear force simulation

Simple RVOT+PA blood flow simulation was achieved using the Ansys 2021 R1 Fluent module as shown in Figures 46 and 47. This pressure and velocity (0.6-0.9 m/s)-based coupled solver simulation illustrated that the anterior leaflet and anterior of the PA wall had the largest shear force, which may serve as an important factor for 3D shaping

autologous heart valve designs in the future in attempting to block autologous heart valve degradation from the headstream for long-term durability. However, this simulation lacked a cardiac cycle (systole and diastole) and stent combination. Therefore, a professional workstation is required to save computer costs and accelerate computational calculations.

## 4.4. Radial force, stent life and hoop force in the RVOT+PA 3D model

In order to obtain the radial force, stent life, and hoop force with the RVOT+PA 3D model, Finite Element Analysis (FEA) was performed in Ansys 2021 R1. As shown in Table 1, DGS-12A had the largest radial force (2.38E+08 N) compared with other stents, while DGS-12C had the smallest radial force (1.69E+05 N). In the hoop force tests, DGS-12A and DGS-12B had the smallest hoop force (1.69E+05 N), while DGS-9A had the largest (60393 N). In the stent life tests, DGS-7, DGS-12A, and DGS-12D had the longest stent life (1.00E+06), while the stent lives of DGS-9A, DGS-8A, and DGS-8B were 0. Here, a stent life of "0" was obtained during the crimping procedure in the head of a delivery system, which may have been due to the unreasonable design of segment II. These three stents should therefore be redesigned or improved for further simulation to establish whether they can be applied in future preclinical studies. In terms of radial force, stent life, and hoop force in the RVOT+PA 3D model, all stents except DGS-9A, DGS-8A, and DGS-8B could be used in vitro testing and future animal trials.

Regarding the testing of radial force, stent life, and hoop force in the RVOT+PA 3D model for Nitinol self-expandable stents, several advantages were identified compared to balloon-expandable prostheses. First, they may be deployed on a beating heart; hence, patient hemodynamics can be maintained, and the danger of prosthesis migration due to pacemaker failure can be eliminated (rapid pacing is required for balloon-expandable valved stents). Second, damage to the leaflets may occur during balloon inflation. This form of prosthesis damage can be eliminated when using self-expandable valved stents. Finally, self-expansion offers the significant benefit of allowing for frequent adjustments of a malpositioned prosthesis. When internal pressure is applied to an artery, longitudinal and circumferential strains occur. Longitudinal stress is caused by the internal pressure pressing on the ends of the artery, extending its length. Circumferential (hoop) stress occurs due to internal pressure pushing radially on the artery walls, thus increasing its diameter. The impact of stent deployment on the artery or the effect of a crimping tool on the stent is similar to that of internal or external pressure on the artery or stent, respectively. Consequently, the stent exerts radial force (RF) onto the artery as it

expands, resulting in hoop stress, which is associated with an expanding hoop force (HF) on the artery wall, producing the hoop stress. In a similar manner, the RF applied by the crimping tool generates hoop stress on the stent, from which the HF may be calculated. This force is circumferential in nature since it is regarded as an expanding force that is exerted on the artery, which corresponds to the phrase "hoop force" in terms of producing hoop stress. RF is used to describe the force generated by the stent in order to withstand compression. Despite the fact that it is referred to as radial force, this force is circumferential as it is thought to be a compressive force acting on the stent. It also coincides with the phrase "hoop force" since it is conceived as a compressive force acting on the stent. Regardless of the nomenclature used, RF and HF have distinct differences in amplitude and direction; therefore, they cannot be directly compared with one another (87-89). In regard to the crimped profile and the results of the simulation, DGS-12A, DGS-12B, DGS-12C, DGS-12D, DGS-10A, DGS-10B, DGS-7, and DGS-5 can be used for in-vitro mechanical tests and preclinical studies.

## 5. Conclusions

According to the above results and discussions, the following conclusions can be reached:

### 5.1. Conclusion 1

Following the design of DGS-12C, DGS-12D, DGS-10A, DGS-10B, DGS-7, and DGS-5, these stents can be subsequently tested in vitro due to their long stent lives, proper radial force, and large hoop force, and can be implanted in the pulmonary valve position in future intro testing and large animal studies.

### 5.2. Conclusion 2

Autologous heart valves can be firmly sutured onto the functional stents to maintain the original geometry prior to implantation for real-time application. Here, the stented autologous pulmonary valve can adapt to various RVOT anatomies to ensure ideal anchoring with safe hemodynamic conduction while preventing paravalvular leak and coronary artery occlusion.

### 5.3. Conclusion 3

Peri-implantation cardiac CT 3D reconstruction and stent simulation can be carried out to better evaluate and visualize pre-clinical and clinical studies.

### 5.4. Conclusion 4

The blood flow simulation of RVOT+PA may serve as a significant factor for stent and autologous pulmonary valve design in sustaining the shear force during the whole cardiac cycle in various hemodynamic situations, especially with respect to the anterior leaflet of the pulmonary valve.

## 6. Limitations

This study only provided the functional stent design for transcatheter autologous pulmonary valve implantation. It demonstrated this using limited simulations without conducting mechanical or in-vivo tests. In addition, this study was limited by the computer's RAM in conducting further simulations, such as in the stent+ RVOT+ PA blood flow simulation during the entire phase of stent deployment. Furthermore, In Group 2 and 3, the crimped stents were still with the out-stretched crowns at the top, middle and basal segments due to the author's insufficient background of engineering and metathetic background, which need further improvements in the future design of TPVR devices. Finally, although new leaflet hosting zones for all stents can be designed according to the different designs of a 3D shaping autologous pulmonary valve, the simulation results may change due to the corresponding changes in the stent architectures and sizes. Therefore, "one-size-fits-all" stents require a flawless "one-size-fits-all" autologous pulmonary valve.

# 7. Future perspectives

## 7.1. TPVR from an autologous pulmonary valve

Transcatheter autologous pulmonary valve implantation may have an even greater potential for application in patients suffering from valvular diseases and congenital heart diseases.

## 7.2. TaPVR – A lifetime solution for patients

Functional stents for transcatheter autologous pulmonary valve implantation may address a variety of contemporary clinical issues, such as PVL, coronary occlusion, and inadaptation in various cardiac anatomies, in order to adopt the new autologous heart valve for a patient's lifetime.

## 7.3. Functional stents for TaPVR

The findings of this study will hopefully serve as a foundation for further improvements in transcatheter autologous pulmonary valve implantation devices.

## 8. References

1. Coffey S, Roberts-Thomson R, Brown A, Carapetis J, Chen M, Enriquez-Sarano M, Zühlke L, Prendergast BD. Global epidemiology of valvular heart disease. Nat Rev Cardiol. 2021;18(12):853-64.

2. Cheatham JP, Hellenbrand WE, Zahn EM, Jones TK, Berman DP, Vincent JA, McElhinney DB. Clinical and hemodynamic outcomes up to 7 years after transcatheter pulmonary valve replacement in the US melody valve investigational device exemption trial. Circulation. 2015;131(22):1960-70.

3. Five insights from the Global Burden of Disease Study 2019. Lancet. 2020;396(10258):1135-59.

4. Global, regional, and national burden of congenital heart disease, 1990-2017: a systematic analysis for the Global Burden of Disease Study 2017. Lancet Child Adolesc Health. 2020;4(3):185-200.

5. Roth GA, Mensah GA, Johnson CO, Addolorato G, Ammirati E, Baddour LM, Barengo NC, Beaton AZ, Benjamin EJ, Benziger CP, Bonny A, Brauer M, Brodmann M, Cahill TJ, Carapetis J, Catapano AL, Chugh SS, Cooper LT, Coresh J, Criqui M, DeCleene N, Eagle KA, Emmons-Bell S, Feigin VL, Fernández-Solà J, Fowkes G, Gakidou E, Grundy SM, He FJ, Howard G, Hu F, Inker L, Karthikeyan G, Kassebaum N, Koroshetz W, Lavie C, Lloyd-Jones D, Lu HS, Mirijello A, Temesgen AM, Mokdad A, Moran AE, Muntner P, Narula J, Neal B, Ntsekhe M, Moraes de Oliveira G, Otto C, Owolabi M, Pratt M, Rajagopalan S, Reitsma M, Ribeiro ALP, Rigotti N, Rodgers A, Sable C, Shakil S, Sliwa-Hahnle K, Stark B, Sundström J, Timpel P, Tleyjeh IM, Valgimigli M, Vos T, Whelton PK, Yacoub M, Zuhlke L, Murray C, Fuster V. Global Burden of Cardiovascular Diseases and Risk Factors, 1990-2019: Update From the GBD 2019 Study. J Am Coll Cardiol. 2020;76(25):2982-3021.

6. Strange G, Stewart S, Celermajer D, Prior D, Scalia GM, Marwick T, Ilton M, Joseph M, Codde J, Playford D. Poor Long-Term Survival in Patients With Moderate Aortic Stenosis. J Am Coll Cardiol. 2019;74(15):1851-63.

7. Chehab O, Roberts-Thomson R, Ng Yin Ling C, Marber M, Prendergast BD, Rajani R, Redwood SR. Secondary mitral regurgitation: pathophysiology, proportionality and prognosis. Heart. 2020;106(10):716-23.

8. Rossi A, Dini FL, Faggiano P, Agricola E, Cicoira M, Frattini S, Simioniuc A, Gullace M, Ghio S, Enriquez-Sarano M, Temporelli PL. Independent prognostic value of functional mitral regurgitation in patients with heart failure. A quantitative analysis of 1256 patients with ischaemic and non-ischaemic dilated cardiomyopathy. Heart. 2011;97(20):1675-80.

9. Coffey S, Cairns BJ, Iung B. The modern epidemiology of heart valve disease. Heart. 2016;102(1):75-85.

10. Dziadzko V, Dziadzko M, Medina-Inojosa JR, Benfari G, Michelena HI, Crestanello JA, Maalouf J, Thapa P, Enriquez-Sarano M. Causes and mechanisms of isolated mitral regurgitation in the community: clinical context and outcome. Eur Heart J. 2019;40(27):2194-202.

11. Andell P, Li X, Martinsson A, Andersson C, Stagmo M, Zöller B, Sundquist K, Smith JG. Epidemiology of valvular heart disease in a Swedish nationwide hospital-based register study. Heart. 2017;103(21):1696-703.

12. Everett RJ, Treibel TA, Fukui M, Lee H, Rigolli M, Singh A, Bijsterveld P, Tastet L, Musa TA, Dobson L, Chin C, Captur G, Om SY, Wiesemann S, Ferreira VM, Piechnik SK, Schulz-Menger J, Schelbert EB, Clavel MA, Newby DE, Myerson SG, Pibarot P, Lee S, Cavalcante JL, Lee SP, McCann GP, Greenwood JP, Moon JC, Dweck MR. Extracellular Myocardial Volume in Patients With Aortic Stenosis. J Am Coll Cardiol. 2020;75(3):304-16.

13. Kong WK, Regeer MV, Ng AC, McCormack L, Poh KK, Yeo TC, Shanks M, Parent S, Enache R, Popescu BA, Yip JW, Ma L, Kamperidis V, van der Velde ET, Mertens B, Ajmone Marsan N, Delgado V, Bax JJ. Sex Differences in Phenotypes of Bicuspid Aortic Valve and Aortopathy: Insights From a Large Multicenter, International Registry. Circ Cardiovasc Imaging. 2017;10(3).

14. Zühlke L, Engel ME, Karthikeyan G, Rangarajan S, Mackie P, Cupido B, Mauff K, Islam S, Joachim A, Daniels R, Francis V, Ogendo S, Gitura B, Mondo C, Okello E, Lwabi P, Al-Kebsi MM, Hugo-Hamman C, Sheta SS, Haileamlak A, Daniel W, Goshu DY, Abdissa SG, Desta AG, Shasho BA, Begna DM, ElSayed A, Ibrahim AS, Musuku J, Bode-Thomas F, Okeahialam BN, Ige O, Sutton C, Misra R, Abul Fadl A, Kennedy N, Damasceno A, Sani M, Ogah OS, Olunuga T, Elhassan HH, Mocumbi AO, Adeoye AM, Mntla P, Ojji D, Mucumbitsi J, Teo K, Yusuf S, Mayosi BM. Characteristics, complications, and gaps in evidence-based interventions in rheumatic heart disease: the Global Rheumatic Heart Disease Registry (the REMEDY study). Eur Heart J. 2015;36(18):1115-22a.

15. Celeng C, Kolossváry M, Kovács A, Molnár A, Szilveszter B, Horváth T, Károlyi M, Jermendy Á L, Tárnoki Á D, Tárnoki DL, Karády J, Voros S, Jermendy G, Merkely B, Maurovich-Horvat P. Aortic root dimensions are predominantly determined by genetic factors: a classical twin study. Eur Radiol. 2017;27(6):2419-25.

16. Canciello G, Mancusi C, Izzo R, Morisco C, Strisciuglio T, Barbato E, Trimarco B, Luca N, de Simone G, Losi MA. Determinants of aortic root dilatation over time in patients with essential hypertension: The Campania Salute Network. Eur J Prev Cardiol. 2020:2047487320931630.

17. Li Y, Wei X, Zhao Z, Liao Y, He J, Xiong T, Xu Y, Lv W, Ou Y, Tang H, Feng Y, Chen M. Prevalence and Complications of Bicuspid Aortic Valve in Chinese According to Echocardiographic Database. Am J Cardiol. 2017;120(2):287-91.

18. Virani SS, Alonso A, Benjamin EJ, Bittencourt MS, Callaway CW, Carson AP, Chamberlain AM, Chang AR, Cheng S, Delling FN, Djousse L, Elkind MSV, Ferguson JF, Fornage M, Khan SS, Kissela BM, Knutson KL, Kwan TW, Lackland DT, Lewis TT, Lichtman JH, Longenecker CT, Loop MS, Lutsey PL, Martin SS, Matsushita K, Moran AE, Mussolino ME, Perak AM, Rosamond WD, Roth GA, Sampson UKA, Satou GM, Schroeder EB, Shah SH, Shay CM, Spartano NL, Stokes A, Tirschwell DL, VanWagner LB, Tsao CW. Heart Disease and Stroke Statistics-2020 Update: A Report From the American Heart Association. Circulation. 2020;141(9):e139-e596.

19. Zhao L, Chen L, Yang T, Wang T, Zhang S, Chen L, Ye Z, Luo L, Qin J. Birth prevalence of congenital heart disease in China, 1980-2019: a systematic review and meta-analysis of 617 studies. Eur J Epidemiol. 2020;35(7):631-42.

20. Nistri S, Basso C, Marzari C, Mormino P, Thiene G. Frequency of bicuspid aortic valve in young male conscripts by echocardiogram. Am J Cardiol. 2005;96(5):718-21.

21. Tutar E, Ekici F, Atalay S, Nacar N. The prevalence of bicuspid aortic valve in newborns by echocardiographic screening. Am Heart J. 2005;150(3):513-5.

22. Galian-Gay L, Carro Hevia A, Teixido-Turà G, Rodríguez Palomares J, Gutiérrez-Moreno L, Maldonado G, Gonzàlez-Alujas MT, Sao-Aviles A, Gallego P, Calvo-Iglesias F, Bermejo J, Robledo-Carmona J, Sánchez V, Saura D, Sevilla T, Burillo-Sanz S, Guala A, Garcia-Dorado D, Evangelista A. Familial clustering of bicuspid aortic valve and its relationship with aortic dilation in first-degree relatives. Heart. 2019;105(8):603-8.

23. van der Linde D, Konings EE, Slager MA, Witsenburg M, Helbing WA, Takkenberg JJ, Roos-Hesselink JW. Birth prevalence of congenital heart disease worldwide: a systematic review and meta-analysis. J Am Coll Cardiol. 2011;58(21):2241-7.

24. Edwin F, Zühlke L, Farouk H, Mocumbi AO, Entsua-Mensah K, Delsol-Gyan D, Bode-Thomas F, Brooks A, Cupido B, Tettey M, Aniteye E, Tamatey MM, Gyan KB, Tchoumi JCT, Elgamal MA. Status and Challenges of Care in Africa for Adults With Congenital Heart Defects. World J Pediatr Congenit Heart Surg. 2017;8(4):495-501.

25. Watkins DA, Johnson CO, Colquhoun SM, Karthikeyan G, Beaton A, Bukhman G, Forouzanfar MH, Longenecker CT, Mayosi BM, Mensah GA, Nascimento BR, Ribeiro ALP, Sable CA, Steer AC, Naghavi M, Mokdad AH, Murray CJL, Vos T, Carapetis JR, Roth GA. Global, Regional, and National Burden of Rheumatic Heart Disease, 1990-2015. N Engl J Med. 2017;377(8):713-22.

26. Cribier A, Eltchaninoff H, Bash A, Borenstein N, Tron C, Bauer F, Derumeaux G, Anselme F, Laborde F, Leon MB. Percutaneous transcatheter implantation of an aortic valve prosthesis for calcific aortic stenosis: first human case description. Circulation. 2002;106(24):3006-8.

27. Cahill TJ, Chen M, Hayashida K, Latib A, Modine T, Piazza N, Redwood S, Søndergaard L, Prendergast BD. Transcatheter aortic valve implantation: current status and future perspectives. Eur Heart J. 2018;39(28):2625-34.

28. Mack MJ, Leon MB, Thourani VH, Makkar R, Kodali SK, Russo M, Kapadia SR, Malaisrie SC, Cohen DJ, Pibarot P, Leipsic J, Hahn RT, Blanke P, Williams MR, McCabe JM, Brown DL, Babaliaros V, Goldman S, Szeto WY, Genereux P, Pershad A, Pocock SJ, Alu MC, Webb JG, Smith CR. Transcatheter Aortic-Valve Replacement with a Balloon-Expandable Valve in Low-Risk Patients. N Engl J Med. 2019;380(18):1695-705.

29. Popma JJ, Deeb GM, Yakubov SJ, Mumtaz M, Gada H, O'Hair D, Bajwa T, Heiser JC, Merhi W, Kleiman NS, Askew J, Sorajja P, Rovin J, Chetcuti SJ, Adams DH, Teirstein PS, Zorn GL, 3rd, Forrest JK, Tchétché D, Resar J, Walton A, Piazza N, Ramlawi B, Robinson N, Petrossian G, Gleason TG, Oh JK, Boulware MJ, Qiao H, Mugglin AS, Reardon MJ. Transcatheter Aortic-Valve Replacement with a Self-Expanding Valve in Low-Risk Patients. N Engl J Med. 2019;380(18):1706-15.

30. Gleason TG, Reardon MJ, Popma JJ, Deeb GM, Yakubov SJ, Lee JS, Kleiman NS, Chetcuti S, Hermiller JB, Jr., Heiser J, Merhi W, Zorn GL, 3rd, Tadros P, Robinson N, Petrossian G, Hughes GC, Harrison JK, Conte JV, Mumtaz M, Oh JK, Huang J, Adams DH. 5-Year Outcomes of Self-Expanding Transcatheter Versus Surgical Aortic Valve Replacement in High-Risk Patients. J Am Coll Cardiol. 2018;72(22):2687-96.

31. Makkar RR, Thourani VH, Mack MJ, Kodali SK, Kapadia S, Webb JG, Yoon SH, Trento A, Svensson LG, Herrmann HC, Szeto WY, Miller DC, Satler L, Cohen DJ, Dewey TM, Babaliaros V, Williams MR, Kereiakes DJ, Zajarias A, Greason KL, Whisenant BK, Hodson RW, Brown DL, Fearon WF, Russo MJ, Pibarot P, Hahn RT, Jaber WA, Rogers E, Xu K, Wheeler J, Alu MC, Smith CR, Leon MB. Five-Year Outcomes of Transcatheter or Surgical Aortic-Valve Replacement. N Engl J Med. 2020;382(9):799-809.

32. Hirji SA, Percy ED, Zogg CK, Malarczyk A, Harloff MT, Yazdchi F, Kaneko T. Comparison of in-hospital outcomes and readmissions for valve-in-valve transcatheter aortic valve replacement vs. reoperative surgical aortic valve replacement: a contemporary assessment of real-world outcomes. Eur Heart J. 2020;41(29):2747-55.

33. Webb JG, Murdoch DJ, Alu MC, Cheung A, Crowley A, Dvir D, Herrmann HC, Kodali SK, Leipsic J, Miller DC, Pibarot P, Suri RM, Wood D, Leon MB, Mack MJ. 3-Year Outcomes After Valve-in-Valve Transcatheter Aortic Valve Replacement for Degenerated Bioprostheses: The PARTNER 2 Registry. J Am Coll Cardiol. 2019;73(21):2647-55.

34. Bonhoeffer P, Boudjemline Y, Saliba Z, Merckx J, Aggoun Y, Bonnet D, Acar P, Le Bidois J, Sidi D, Kachaner J. Percutaneous replacement of pulmonary valve in a right-ventricle to pulmonary-artery prosthetic conduit with valve dysfunction. Lancet. 2000;356(9239):1403-5.

35. Nordmeyer J, Ewert P, Gewillig M, AlJufan M, Carminati M, Kretschmar O, Uebing A, Dähnert I, Röhle R, Schneider H, Witsenburg M, Benson L, Gitter R, Bökenkamp R, Mahadevan V, Berger F. Acute and midterm outcomes of the post-approval MELODY Registry: a multicentre registry of transcatheter pulmonary valve implantation. Eur Heart J. 2019;40(27):2255-64.

36. Shahanavaz S, Qureshi AM, Levi DS, Boudjemline Y, Peng LF, Martin MH, Bauser-Heaton H, Keeshan B, Asnes JD, Jones TK, Justino H, Aboulhosn JA, Gray RG, Nguyen H, Balzer DT, McElhinney DB. Transcatheter Pulmonary Valve Replacement With the Melody Valve in Small Diameter Expandable Right Ventricular Outflow Tract Conduits. JACC Cardiovasc Interv. 2018;11(6):554-64.

37. Georgiev S, Ewert P, Eicken A, Hager A, Hörer J, Cleuziou J, Meierhofer C, Tanase D. Munich Comparative Study: Prospective Long-Term Outcome of the Transcatheter Melody Valve Versus Surgical Pulmonary Bioprosthesis With Up to 12 Years of Follow-Up. Circ Cardiovasc Interv. 2020;13(7):e008963.

38. Shahanavaz S, Zahn EM, Levi DS, Aboulhousn JA, Hascoet S, Qureshi AM, Porras D, Morgan GJ, Bauser Heaton H, Martin MH, Keeshan B, Asnes JD, Kenny D, Ringewald JM, Zablah JE, Ivy M, Morray BH, Torres AJ, Berman DP, Gillespie MJ, Chaszczewski K, Zampi JD, Walsh KP, Julien P, Goldstein BH, Sathanandam SK, Karsenty C, Balzer DT, McElhinney DB. Transcatheter Pulmonary Valve Replacement With the Sapien Prosthesis. J Am Coll Cardiol. 2020;76(24):2847-58.

39. Goldstein BH, Bergersen L, Armstrong AK, Boe BA, El-Said H, Porras D, Shahanavaz S, Leahy RA, Kreutzer J, Zampi JD, Hainstock MR, Gudausky TM, Nicholson GT, Gauvreau K, Goodman A, Petit CJ. Adverse Events, Radiation Exposure, and Reinterventions Following Transcatheter Pulmonary Valve Replacement. J Am Coll Cardiol. 2020;75(4):363-76.

40. Riahi M, Ang HL, Jones M, Prachasilchai P, Baruteau AE, Promphan W, Rosenthal E, Qureshi SA. Infolding of the Venus P-Valve After Transcatheter Pulmonary Valve Implantation. Circ Cardiovasc Interv. 2018;11(4):e005923.

41. Morgan GJ, Sivakumar K, Promphan W, Goreczny S, Prachasilchai P, Qureshi S. Early clinical experience with the straight design of Venus P-valve™ in dysfunctional right ventricular outflow tracts. Catheter Cardiovasc Interv. 2020;96(6):E653-e9.

42. Ou-Yang WB, Qureshi S, Ge JB, Hu SS, Li SJ, Yang KM, Zhang GJ, Zhou DX, Chen M, Wang SZ, Zhang FW, Pan XB. Multicenter Comparison of Percutaneous and Surgical Pulmonary Valve Replacement in Large RVOT. Ann Thorac Surg. 2020;110(3):980-7.

43. Otto CM, Nishimura RA, Bonow RO, Carabello BA, Erwin JP, 3rd, Gentile F, Jneid H, Krieger EV, Mack M, McLeod C, O'Gara PT, Rigolin VH, Sundt TM, 3rd, Thompson A, Toly C. 2020 ACC/AHA Guideline for the Management of Patients With Valvular Heart Disease: A Report of the American College of Cardiology/American Heart Association Joint Committee on Clinical Practice Guidelines. Circulation. 2021;143(5):e72-e227.

44. Otto CM, Nishimura RA, Bonow RO, Carabello BA, Erwin JP, 3rd, Gentile F, Jneid H, Krieger EV, Mack M, McLeod C, O'Gara PT, Rigolin VH, Sundt TM, 3rd, Thompson A, Toly C. 2020 ACC/AHA Guideline for the Management of Patients With Valvular Heart Disease: Executive Summary: A Report of the American College of Cardiology/American Heart Association Joint Committee on Clinical Practice Guidelines. Circulation. 2021;143(5):e35-e71.

45. Vahanian A, Beyersdorf F, Praz F, Milojevic M, Baldus S, Bauersachs J, Capodanno D, Conradi L, De Bonis M, De Paulis R, Delgado V, Freemantle N, Gilard M, Haugaa KH, Jeppsson A, Jüni P, Pierard L, Prendergast BD, Sádaba JR, Tribouilloy C, Wojakowski W. 2021 ESC/EACTS Guidelines for the management of valvular heart disease. Eur Heart J. 2022;43(7):561-632.

46. Stout KK, Daniels CJ, Aboulhosn JA, Bozkurt B, Broberg CS, Colman JM, Crumb SR, Dearani JA, Fuller S, Gurvitz M, Khairy P, Landzberg MJ, Saidi A, Valente AM, Van Hare GF. 2018 AHA/ACC Guideline for the Management of Adults With Congenital Heart Disease: A Report of the American College of Cardiology/American Heart Association Task Force on Clinical Practice Guidelines. J Am Coll Cardiol. 2019;73(12):e81-e192.

47. Baumgartner H, De Backer J, Babu-Narayan SV, Budts W, Chessa M, Diller GP, Lung B, Kluin J, Lang IM, Meijboom F, Moons P, Mulder BJM, Oechslin E, Roos-Hesselink JW, Schwerzmann M, Sondergaard L, Zeppenfeld K. 2020 ESC Guidelines for the management of adult congenital heart disease. Eur Heart J. 2021;42(6):563-645.

48. Kahlert P, Al-Rashid F, Döttger P, Mori K, Plicht B, Wendt D, Bergmann L, Kottenberg E, Schlamann M, Mummel P, Holle D, Thielmann M, Jakob HG, Konorza T, Heusch G, Erbel R, Eggebrecht H. Cerebral embolization during transcatheter aortic valve implantation: a transcranial Doppler study. Circulation. 2012;126(10):1245-55.

49. Arsalan M, Walther T. Durability of prostheses for transcatheter aortic valve implantation. Nat Rev Cardiol. 2016;13(6):360-7.

50. Capodanno D, Petronio AS, Prendergast B, Eltchaninoff H, Vahanian A, Modine T, Lancellotti P, Sondergaard L, Ludman PF, Tamburino C, Piazza N, Hancock J, Mehilli J, Byrne RA, Baumbach A, Kappetein AP, Windecker S, Bax J, Haude M. Standardized definitions of structural deterioration and valve failure in assessing long-term durability of transcatheter and surgical aortic bioprosthetic valves: a consensus statement from the European Association of Percutaneous Cardiovascular Interventions (EAPCI) endorsed by the European Society of Cardiology (ESC) and the European Association for Cardio-Thoracic Surgery (EACTS). Eur Heart J. 2017;38(45):3382-90.

51. Dvir D, Bourguignon T, Otto CM, Hahn RT, Rosenhek R, Webb JG, Treede H, Sarano ME, Feldman T, Wijeysundera HC, Topilsky Y, Aupart M, Reardon MJ, Mackensen GB, Szeto WY, Kornowski R, Gammie JS, Yoganathan AP, Arbel Y, Borger MA, Simonato M, Reisman M, Makkar RR, Abizaid A, McCabe JM, Dahle G, Aldea GS, Leipsic J, Pibarot P, Moat NE, Mack MJ, Kappetein AP, Leon MB. Standardized Definition of Structural Valve Degeneration for Surgical and Transcatheter Bioprosthetic Aortic Valves. Circulation. 2018;137(4):388-99.

52. Nazif TM, Dizon JM, Hahn RT, Xu K, Babaliaros V, Douglas PS, El-Chami MF, Herrmann HC, Mack M, Makkar RR, Miller DC, Pichard A, Tuzcu EM, Szeto WY, Webb JG, Moses JW, Smith CR, Williams MR, Leon MB, Kodali SK. Predictors and clinical outcomes of permanent pacemaker implantation after transcatheter aortic valve replacement: the PARTNER (Placement of AoRtic TraNscathetER Valves) trial and registry. JACC Cardiovasc Interv. 2015;8(1 Pt A):60-9.

53. Siontis GC, Jüni P, Pilgrim T, Stortecky S, Büllesfeld L, Meier B, Wenaweser P, Windecker S. Predictors of permanent pacemaker implantation in patients with severe aortic stenosis undergoing TAVR: a meta-analysis. J Am Coll Cardiol. 2014;64(2):129-40.

54. Latib A, Naim C, De Bonis M, Sinning JM, Maisano F, Barbanti M, Parolari A, Lorusso R, Testa L, Actis Dato GM, Miceli A, Sponga S, Rosato F, De Vincentiis C, Werner N, Fiorina C, Bartorelli A, Di Gregorio O, Casilli F, Muratori M, Alamanni F, Glauber M, Livi U, Nickenig G, Tamburino C, Alfieri O, Colombo A. TAVR-associated prosthetic valve infective endocarditis: results of a large, multicenter registry. J Am Coll Cardiol. 2014;64(20):2176-8.

55. Cahill TJ, Baddour LM, Habib G, Hoen B, Salaun E, Pettersson GB, Schäfers HJ, Prendergast BD. Challenges in Infective Endocarditis. J Am Coll Cardiol. 2017;69(3):325-44.

56. Yudi MB, Sharma SK, Tang GHL, Kini A. Coronary Angiography and Percutaneous Coronary Intervention After Transcatheter Aortic Valve Replacement. J Am Coll Cardiol. 2018;71(12):1360-78.

57. Yang TH, Webb JG, Blanke P, Dvir D, Hansson NC, Nørgaard BL, Thompson CR, Thomas M, Wendler O, Vahanian A, Himbert D, Kodali SK, Hahn RT, Thourani VH, Schymik G, Precious B, Berger A, Wood DA, Pibarot P, Rodés-Cabau J, Jaber WA, Leon MB, Walther T, Leipsic J. Incidence and severity of paravalvular aortic regurgitation with multidetector computed tomography nominal area oversizing or undersizing after transcatheter heart valve replacement with the Sapien 3: a comparison with the Sapien XT. JACC Cardiovasc Interv. 2015;8(3):462-71.

58. Popma JJ, Adams DH, Reardon MJ, Yakubov SJ, Kleiman NS, Heimansohn D, Hermiller J, Jr., Hughes GC, Harrison JK, Coselli J, Diez J, Kafi A, Schreiber T, Gleason TG, Conte J, Buchbinder M, Deeb GM, Carabello B, Serruys PW, Chenoweth S, Oh JK. Transcatheter aortic valve replacement using a self-expanding bioprosthesis in patients with severe aortic stenosis at extreme risk for surgery. J Am Coll Cardiol. 2014;63(19):1972-81.

59. Mentias A, Desai MY, Saad M, Horwitz PA, Rossen JD, Panaich S, Elbadawi A, Abbott JD, Sorajja P, Jneid H, Tuzcu EM, Kapadia S, Vaughan-Sarrazin M. Incidence and Outcomes of Acute Coronary Syndrome After Transcatheter Aortic Valve Replacement. JACC Cardiovasc Interv. 2020;13(8):938-50.

60. Fröhlich GM, Baxter PD, Malkin CJ, Scott DJ, Moat NE, Hildick-Smith D, Cunningham D, MacCarthy PA, Trivedi U, de Belder MA, Ludman PF, Blackman DJ. Comparative survival after transapical, direct aortic, and subclavian transcatheter aortic valve implantation (data from the UK TAVI registry). Am J Cardiol. 2015;116(10):1555-9.

61. Greenbaum AB, O'Neill WW, Paone G, Guerrero ME, Wyman JF, Cooper RL, Lederman RJ. Caval-aortic access to allow transcatheter aortic valve replacement in otherwise ineligible patients: initial human experience. J Am Coll Cardiol. 2014;63(25 Pt A):2795-804.

62. Ansari MM, Cardoso R, Garcia D, Sandhu S, Horlick E, Brinster D, Martucci G, Piazza N. Percutaneous Pulmonary Valve Implantation: Present Status and Evolving Future. J Am Coll Cardiol. 2015;66(20):2246-55.

63. McElhinney DB, Benson LN, Eicken A, Kreutzer J, Padera RF, Zahn EM. Infective endocarditis after transcatheter pulmonary valve replacement using the Melody valve: combined results of 3 prospective North American and European studies. Circ Cardiovasc Interv. 2013;6(3):292-300.

64. Chatterjee A, Bajaj NS, McMahon WS, Cribbs MG, White JS, Mukherjee A, Law MA. Transcatheter Pulmonary Valve Implantation: A Comprehensive Systematic Review and Meta-Analyses of Observational Studies. J Am Heart Assoc. 2017;6(8).

65. Hascoet S, Mauri L, Claude C, Fournier E, Lourtet J, Riou JY, Brenot P, Petit J. Infective Endocarditis Risk After Percutaneous Pulmonary Valve Implantation With the Melody and Sapien Valves. JACC Cardiovasc Interv. 2017;10(5):510-7.

66. Georgiev S, Ewert P, Tanase D, Hess J, Hager A, Cleuziou J, Meierhofer C, Eicken A. A Low Residual Pressure Gradient Yields Excellent Long-Term Outcome After Percutaneous Pulmonary Valve Implantation. JACC Cardiovasc Interv. 2019;12(16):1594-603.

67. Martin MH, Meadows J, McElhinney DB, Goldstein BH, Bergersen L, Qureshi AM, Shahanavaz S, Aboulhosn J, Berman D, Peng L, Gillespie M, Armstrong A, Weng C, Minich LL, Gray RG. Safety and Feasibility of Melody Transcatheter Pulmonary Valve Replacement in the Native Right Ventricular Outflow Tract: A Multicenter Pediatric Heart Network Scholar Study. JACC Cardiovasc Interv. 2018;11(16):1642-50.

68. Sun X, Hao Y, Sebastian Kiekenap JF, Emeis J, Steitz M, Breitenstein-Attach A, Berger F, Schmitt B. Four-Dimensional Computed Tomography-Guided Valve Sizing for Transcatheter Pulmonary Valve Replacement. J Vis Exp. 2022(179).

69. Dubey A, B V, Bég OA, Gorla RSR. Finite element computation of magneto-hemodynamic flow and heat transfer in a bifurcated artery with saccular aneurysm using the Carreau-Yasuda biorheological model. Microvasc Res. 2021;138:104221.

70. Abdollahzadeh Jamalabadi MY, Daqiqshirazi M, Nasiri H, Safaei MR, Nguyen TK. Modeling and analysis of biomagnetic blood Carreau fluid flow through a stenosis artery with magnetic heat transfer: A transient study. PLoS One. 2018;13(2):e0192138.

71. Arai T, Lefèvre T, Hovasse T, Morice MC, Romano M, Benamer H, Garot P, Hayashida K, Bouvier E, Chevalier B. The feasibility of transcatheter aortic valve implantation using the Edwards SAPIEN 3 for patients with severe bicuspid aortic stenosis. J Cardiol. 2017;70(3):220-4.

72. Karamlou T, Pettersson G, Nigro JJ. Commentary: A pediatric perspective on the Ozaki procedure. J Thorac Cardiovasc Surg. 2021;161(5):1582-3.

73. Tchetche D, Van Mieghem NM. New-generation TAVI devices: description and specifications. EuroIntervention. 2014;10 Suppl U:U90-u100.

74. Rheude T, Blumenstein J, Möllmann H, Husser O. Spotlight on the SAPIEN 3 transcatheter heart valve. Med Devices (Auckl). 2018;11:353-60.

75. Noterdaeme T, Marx N, Lange R. A novel transcatheter aortic valve with a form-fitting anchor for self-alignment: feasibility in a chronic preclinical model. Interact Cardiovasc Thorac Surg. 2019;29(1):8-14.

76. Kim WK, Hengstenberg C, Hilker M, Schäfer U, Rudolph TK, Toggweiler S, Rück A, Søndergaard L, Conradi L, Hamm C, Walther T, Möllmann H. Transcatheter aortic valve implantation with the ACURATE neo valve: indications, procedural aspects and clinical outcomes. EuroIntervention. 2020;15(18):e1571-e9.

77. Okuno T, Lanz J, Pilgrim T. ACURATE neo: How Is This TAVR Valve Doing to Fit into an Increasingly Crowded Field? Curr Cardiol Rep. 2020;22(10):107.

78. Law MA, Chatterjee A. Transcatheter pulmonic valve implantation: Techniques, current roles, and future implications. World J Cardiol. 2021;13(5):117-29.

79. Elattar MA, Vink LW, van Mourik MS, Baan J, Jr., vanBavel ET, Planken RN, Marquering HA. Dynamics of the aortic annulus in 4D CT angiography for transcatheter aortic valve implantation patients. PLoS One. 2017;12(9):e0184133.

80. Pluchinotta FR, Sturla F, Caimi A, Giugno L, Chessa M, Giamberti A, Votta E, Redaelli A, Carminati M. 3-Dimensional personalized planning for transcatheter pulmonary valve implantation in a dysfunctional right ventricular outflow tract. Int J Cardiol. 2020;309:33-9.

81. Ooms JF, Wang DD, Rajani R, Redwood S, Little SH, Chuang ML, Popma JJ, Dahle G, Pfeiffer M, Kanda B, Minet M, Hirsch A, Budde RP, De Jaegere PP, Prendergast B, O'Neill W, Van Mieghem NM. Computed Tomography-Derived 3D Modeling to Guide Sizing and Planning of Transcatheter Mitral Valve Interventions. JACC Cardiovasc Imaging. 2021;14(8):1644-58.

82. Chung R, Taylor AM. Imaging for preintervention planning: transcatheter pulmonary valve therapy. Circ Cardiovasc Imaging. 2014;7(1):182-9.

83. Curran L, Agrawal H, Kallianos K, Kheiwa A, Lin S, Ordovas K, Mahadevan VS. Computed tomography guided sizing for transcatheter pulmonary valve replacement. Int J Cardiol Heart Vasc. 2020;29:100523.

84. Saremi F, Gera A, Ho SY, Hijazi ZM, Sánchez-Quintana D. CT and MR imaging of the pulmonary valve. Radiographics. 2014;34(1):51-71.

85. Anderson RH, Mori S, Spicer DE, Cheung JW, Lerman BB. Living anatomy of the pulmonary root. J Cardiovasc Electrophysiol. 2018;29(9):1238-40.

86. Dong X, Sun Q, Tang M, Zhang S. Types of anatomic relationship between left main coronary artery and pulmonary sinus of Valsalva: Implications for balloon pulmonary angioplasty and catheter ablation in the pulmonary root. Int J Cardiol. 2019;288:34-8.

87. Zegdi R, Lecuyer L, Achouh P, Didier B, Lafont A, Latrémouille C, Fabiani JN. Increased radial force improves stent deployment in tricuspid but not in bicuspid stenotic native aortic valves. Ann Thorac Surg. 2010;89(3):768-72.

88. Cabrera MS, Oomens CW, Baaijens FP. Understanding the requirements of self-expandable stents for heart valve replacement: Radial force, hoop force and equilibrium. J Mech Behav Biomed Mater. 2017;68:252-64.

89. Cabrera MS, Sanders B, Goor O, Driessen-Mol A, Oomens CWJ, Baaijens FPT. Computationally Designed 3D Printed Self-Expandable Polymer Stents with Biodegradation Capacity for Minimally Invasive Heart Valve Implantation: A Proof-of-Concept Study. 3D Print Addit Manuf. 2017;4(1):19-29.

**Statutory Declaration**

"I, **Xiaolin Sun**, by personally signing this document in lieu of an oath, hereby affirm that I prepared the submitted dissertation on the topic [**English: Functional heart valve stent designs for future transcatheter autologous pulmonary valve replacement, Deutsch: Funktionelle Herzklappen-Stent Designs für zukünftige autologe, transkatheter Klappenprothesen in pulmonaler Position**], independently and without the support of third parties, and that I used no other sources and aids than those stated. All parts which are based on the publications or presentations of other authors, either in letter or in spirit, are specified as such in accordance with the citing guidelines. The sections on methodology (in particular regarding practical work, laboratory regulations, statistical processing) and results (in particular regarding figures, charts and tables) are exclusively my responsibility.

My contributions to any publications to this dissertation correspond to those stated in the below joint declaration made together with the supervisor. All publications created within the scope of the dissertation comply with the guidelines of the ICMJE (International Committee of Medical Journal Editors; www.icmje.org) on authorship. In addition, I declare that I shall comply with the regulations of Charité – Universitätsmedizin Berlin on ensuring good scientific practice.

I declare that I have not yet submitted this dissertation in identical or similar form to another Faculty.

The significance of this statutory declaration and the consequences of a false statutory declaration under criminal law (Sections 156, 161 of the German Criminal Code) are known to me."

Date                                    Signature

**Curriculum Vitae**

My curriculum vitae does not appear in the electronic version of my paper for reasons of data protection.

My curriculum vitae does not appear in the electronic version of my paper for reasons of data protection.

**Complete list of publications**

1.  ___Sun, X.,___ Hao, Y., Sebastian, Kiekenap, J.F., Emeis, J., Steitz, M., Breitenstein-Attach, A., Berger, F., Schmitt, B. Four-Dimensional Computed Tomography-Guided Valve Sizing for Transcatheter Pulmonary Valve Replacement. J. Vis. Exp. (179), e63367, doi: 10.3791/63367 (2022). *(2021 IF: 1.355), Share the first authorship.*

2.  Hao, Y., ___Sun, X.___, Kiekenap, J., Emeis, J., Steitz, M., Breitenstein-Attach, A., Berger, F., & Schmitt, B. (2022). Transcatheter Pulmonary Valve Replacement from Autologous Pericardium with a Self-Expandable Nitinol Stent in an Adult Sheep Model. J. Vis. Exp. (184), 10.3791/63661 (2022). https://doi.org/10.3791/63661, (2021 IF: 1.355)

3.  ___Sun, X.___, Hao, Y., Steitz, M., Breitenstein-Attach, A., Kiekenap, J.F.S., Emeis, J.; Khan, M.B., Berger, F., Schmitt, B. Straightened Segmentation in 4D Cardiac CT: A Practical Method for Multiparametric Characterization of the Landing Zone for Transcatheter Pulmonary Valve Replacement. Appl. Sci. 2022, 12, 12912. https://doi.org/10.3390/ app122412912. (2021 IF: 2.838). S*hare the first authorship.*

## Acknowledgements

I would like to express my heartfelt appreciation to my supervisor, **_PD Dr. Boris Schmitt_**, for providing me with the opportunity and support to conduct this study in our GrOwnValve research group at Charité – Universitätsmedizin Berlin, Campus Virchow-Klinikum, as well as for his continuous guidance, encouragement, and care throughout the duration of the study. His insightful remarks, as well as his rigorous perusal of this dissertation, are much appreciated.

I deeply appreciate the direction from **_Prof. Dr. Felix Berger and Dr. Thore Dietrich_**, who gave me valuable comments helping to improve the quality of the dissertation and encouraged me complete my doctoral study.

I would also like to thank all my colleagues in our team, particularly **_Jasper Emeis_** for his assistance with various tasks in our office, as well as **_Marvin Steitz, Alexander Breitenstein, Mahamuda Badhon Khan_** and **_Dr. Ferenc Markus_** for their outstanding technical assistance. I would like to express my gratitude to **_the colleagues at FEM_** for their assistance with our animal trials.

Furthermore, I would also like to express my sincere gratitude to **_the China Scholarship Council (No. 201908080063)_** and **_the Deutsches Zentrum für Herz-Kreislauf-Forschung e.V. (DZHK)_** whose financial assistance enables me to successfully complete my research work abroad. I also want to thank **_Mrs. Claudia Jaramillo_** in the Promotionsbüro of Charité – Universitätsmedizin Berlin for her help in completing my entire doctoral procedure.

Words cannot describe how thankful I am for my wife **_Yimeng Hao_**'s support. I am genuinely grateful for the support and encouragement offered by **_my entire family_**.

# Letter of Statistical Confirmation

## CHARITÉ

### CharitéCentrum für Human- und Gesundheitswissenschaften

Charité | Campus Charité Mitte | 10117 Berlin

**Institut für Biometrie und Klinische Epidemiologie (iBikE)**

Direktor: Prof. Dr. Frank Konietschke

Postanschrift:
Charitéplatz 1 | 10117 Berlin
Besucheranschrift:
Reinhardtstr. 58 | 10117 Berlin

Tel. +49 (0)30 450 562171
frank.konietschke@charite.de
https://biometrie.charite.de/

---

Surname, Name: Sun, Xiaolin

Email: xiaolin.sun@charite.de

Immatriculation Number: 226463

Thesis Advisor: PD.Dr.med Boris Schmitt

Institution / Clinic: Deutsches Herzzentrum Berlin, Campus Virchow-Klinikum

---

## Certification

I hereby certify that Mr. Sun has taken a statistical consultation on a PhD project with me, within the Service Unit Biometry of the Institute of Biometry and Clinical Epidemiology (iBikE). The following consultation date was attended:

- Appointment 1: 20.4.2022

The following key advice regarding meaningful analysis and interpretation of data was given during the consultation:

> *The work of Mr. Sun is based on design of different heart valve stents and simulations thereof to derive radial force and hoop force of each stent. As such this work, as far as presented to me during the statistical consultation, does not contain a relevant statistical component, therefore statistical advice is not applicable. This was also approved by his supervisor PD Dr. med. Boris Schmitt in writing on June, 18th, 2022.*

This certificate does not guarantee the correct implementation of the suggestions made in the consultation, the correct performance of the recommended statistical procedures, nor the correct presentation and interpretation of the results. The responsibility for this rests solely with the doctoral student. The Institute of Biometry and Clinical Epidemiology assumes no liability for this.

Date: 17.8.2022

Annette Aigner
Digital unterschrieben von
Annette Aigner
Datum: 2022.08.17 20:03:59
+02'00'

Name of consultant: Annette Aigner, PhD

CHARITÉ
UNIVERSITÄTSMEDIZIN BERLIN
Institut für Biometrie und
Klinische Epidemiologie
Campus Charité Mitte
Charitéplatz 1 | D-10117 Berlin
Sitz: Reinhardtstr. 58

_____
Signature consultant, institute stamp